Simulation of Reflectometry Measurements between Mars Express and ExoMars Trace Gas Orbiter

AE5822: Thesis Space

Nicola Beugel

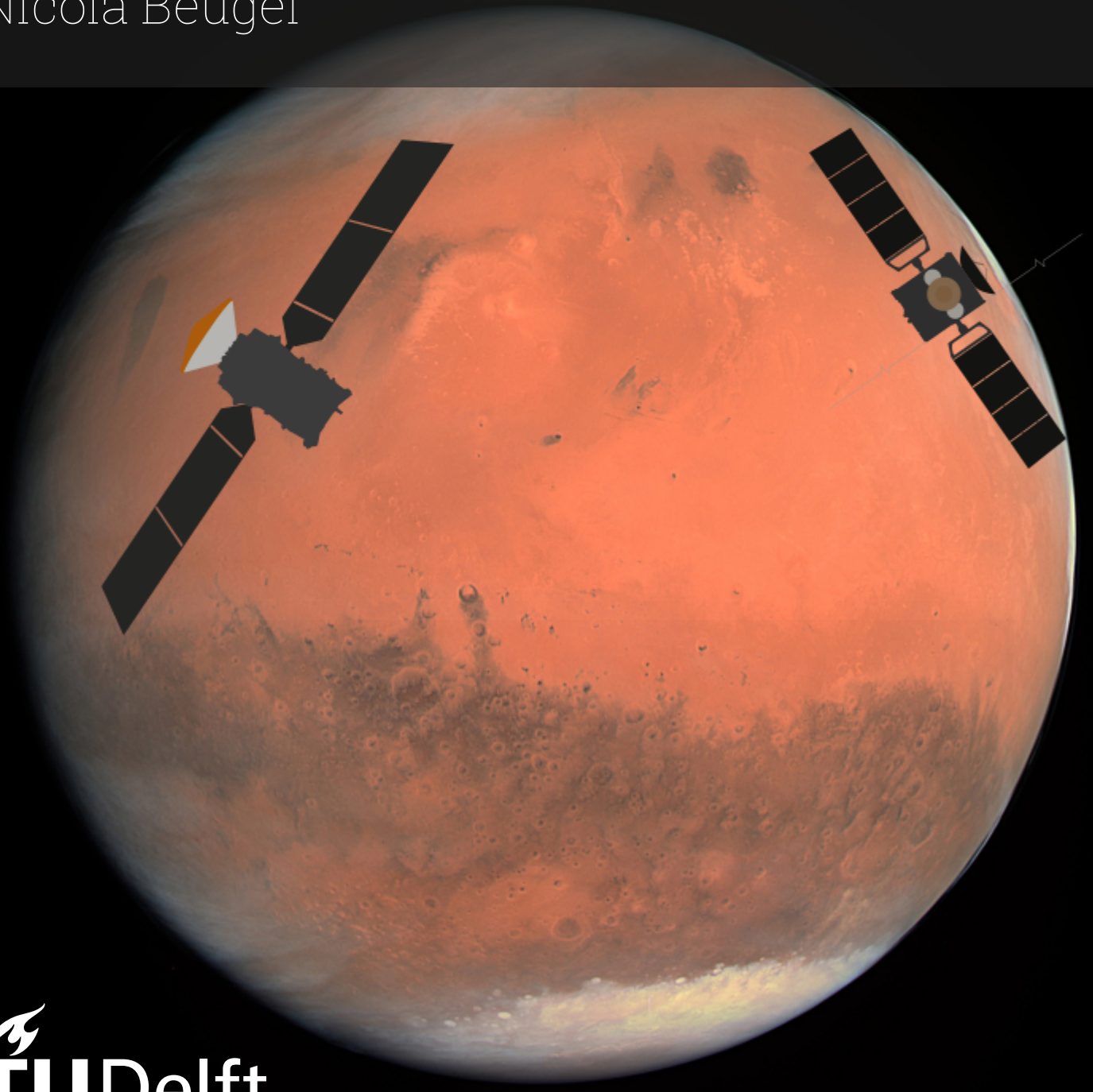

Delft University of Technology

TU Delft

Simulation of Reflectometry Measurements between Mars Express and ExoMars Trace Gas Orbiter

by

Nicola Beugel

to obtain the degree of Master of Science

at the Delft University of Technology,

to be defended publicly on Tuesday March 31, 2026 at 13:30.

Student number:	5345049	
Project duration:	May 27, 2025 – March 31, 2026	
Thesis committee:	Prof. dr. B. L. A. Vermeersen,	Supervisor
	Ir. L. H. Svedhem,	Daily Supervisor
	Dr. ir. W. van der Wal,	Chair
	Dr. ir. R. Saathof,	External Examiner

Cover: Created using True-colour image of Mars seen by OSIRIS [13] by ESA & MPS for OSIRIS Team under CC BY-SA 3.0 IGO and using ExoMars TGO size vs Mars Express [37] by SkywalkerPL under CC BY 4.0 (Modified)

An electronic version of this thesis is available at http://repository.tudelft.nl/.

TU Delft

Preface

Before you lies the master thesis ”Simulation of Reflectometry Measurements between Mars Express and ExoMars Trace Gas Orbiter”. When hearing about this thesis topic for the first time, it immediately caught my attention. The exploration of what lies beyond Earth has always fascinated me, so doing a master thesis about a new way to investigate Mars, our neighboring planet, felt like a perfect fit. Looking back I certainly do not regret my decision.

Reflecting upon my time here at the TU Delft, I recall all the great moments and many opportunities that I had, from experiments with superconductors in liquid nitrogen to living abroad for 6 months to do an internship and on the way making friends for life. The completion of this thesis marks the end of my time as a student. The time flew by and I feel a little sad that this period of my life is coming to an end. But it also feels exciting to start my career and discover what the future has in store for me. It was not always easy but it was worth it in the end, and I would like to thank everyone who helped me along the way.

First of all, I would like to thank my daily supervisor Håkan Svedhem for all the guidance and feedback that you gave during this project and whom it was a pleasure to work with. Your positive attitude really gave me a lot of motivation and you made the whole project a pleasant experience.

Finally, I want to thank my family and friends, especially my amazing parents, for all their support during not only this project, but my entire time here in Delft. Throughout all the highlights and difficult moments, you were there to support me and remind me that everything was going to be okay and this really means the world to me.

To anyone who may read this thesis, I hope that it helps you with your own work and/or better understanding in this field of study and I hope that you enjoy reading it as much as I enjoyed working on it.

Nicola Beugel
Delft, March 2026

Summary

For centuries Mars has been a topic of interest to scientists. Mars's geology, atmosphere, and climate history provides crucial insight into the evolution of planetary environments and into the understanding of our own planet Earth. Over the years, numerous measurements have taken place at Mars. One of these types of measurements were mutual radio occultation measurements between Mars Express (MEX) and ExoMars Trace Gas Orbiter (TGO). When an occultation measurement with an incorrect switch-on time was performed, a significant return signal arriving from the surface of Mars was observed. This unexpected result opened up opportunities to look into the possibilities of using reflectometry measurements between MEX and TGO to research the Martian (sub)surface. Thus, in 2025 European Space Agency (ESA) started with so called bistatic radar experiments (with MEX transmitting and TGO receiving) [41].

Nieuwenhuizen [35] conducted an initial investigation into the modeling of these bistatic measurements and several recommendations were made for follow-up research. The aim of this thesis was to use these recommendations to create an improved bistatic measurement model and compare this model with measured data and the initial model of Nieuwenhuizen [35]. This thesis also investigated future measurement opportunities and whether reflectometry techniques presently used with Earth remote sensing, GNSS-Reflectometry (GNSS-R) [16], could be applied to Mars bistatic radar measurements.

A bistatic geometry search script was created to determine the Specular Point (SP) surface coordinates (used in the bistatic measurement simulation) and to search for future measurement opportunities. A large amount of measurement opportunities was found for June,July and August of 2026. These opportunities were then ranked based on several (geometry) parameters, including whether any Region of Interests (ROIs) were intersected and the first seven opportunities were shown in figure 5.4.

The new bistatic measurement simulation model (created in Python) made several improvements compared to Nieuwenhuizen [35], including the utilization of the SPICE toolkit shape kernel files to be able to use the full 128 pixel per degree resolution of the Mars Orbiter Laser Altimeter (MOLA) Digital Elevation Model (DEM) of Mars. The model also incorporated the effects of the polarization of the MEX and TGO antennas to better model the reflected power.

The increase in spatial resolution resulted in significant improvement compared to Nieuwenhuizen [35]. Moreover, the model almost always matches the general shape of the measured data (all be it with less power/over a smaller power scale) and the majority of spikes/dips in power caused by geographic features like craters are observable in the model. There are however certain features in the power data that were not present in the model. These were mainly present when the incidence angle became small. A possible explanation for this could be the missing transmitted Left Hand Circular Polarized (LHCP) signal component from the MEX MelaCom antenna (for which no antenna pattern was available found and thus was not modeled).

Several key parameters were also investigated in the model. It was found that the incidence angle together with the antenna polarizations play an important role to achieve the best reflected signal power due to the large dependence of the reflectivity on both of these parameters. Furthermore the pointing of the two spacecraft also plays a key role for the reflected signal due to the (undesired) direct signal component that can arise under certain pointing conditions. Moreover, it was found that pointing directly towards the SP (instead of the nominal nadir-pointing attitude) was not a viable strategy to increase the reflected power because it caused the direct power to be much higher than the reflected power, removing any details from the reflected power signal. The permittivity sensitivity of the received signal was also investigated. It was found to influence the reflected power in different ways depending on whether the rr reflectivity or rl reflectivity was dominant. The sensitivity of the reflected power was shown to be (just) above the noise floor for differences in relative permittivity of 2.0, but that this heavily relied on the absolute reflected power of the measurement being significantly large enough. Finally, an investigation of the optimal incidence angle was also performed. This yielded that when optimizing for

maximum reflected power the optimal incidence angle for nadir pointing (pointing towards the planet center) lied between $40\,°$ and $80\,°$ depending on the transmitter (TX) and receiver (RX) distances to the SP. For SP pointing the optimal incidence angle for maximum reflected power was found to be $90\,°$ regardless of the TX or RX distance to the SP. Optimal incidence angle investigations for minimizing the direct power and maximizing the reflected to direct power ratio were also performed to investigate the SP pointing direct power problem but these only showed that SP pointing with the current antenna polarization configuration is not feasible.

Contents

List of Figures

List of Tables

Nomenclature

List of Abbreviations

Abbreviation	Definition
ADC	Analog-to-Digital Converter
AGC	Automatic Gain Control
BSR	Bi-Static Radar
cGNSS-R	conventional GNSS-R
CK	Camera Kernel
DDM	Delay-Doppler Map
DEM	Digital Elevation Model
DSK	Digital Shape Kernel
ESA	European Space Agency
ET	Ephemeris Time
FFT	fast Fourier transform
FK	Frame Kernel
FREND	Fine Resolution Epithermal Neutron Detector
FTP	File Transfer Protocol
GNSS	Global Navigation Satellite System
GNSS-R	GNSS-Reflectometry
GRS	Gamma-Ray Spectrometer
IEM	Integral Equation Model
iGNSS-R	interferometric GNSS-R
IQ	In-phase / Quadrature
KA-GO	Kirchoff Approximation to Geometric Optics
LHCP	Left Hand Circular Polarized
LSK	Leap Second Kernel
MEGRD	Mission Experiment Gridded Data Record
MEX	Mars Express
MOLA	Mars Orbiter Laser Altimeter
PCK	Planetary Constants Kernel
PRN	Pseudo-Random Noise
RHCP	Right Hand Circular Polarized
RMS	Root Mean Square
ROI	Region of Interest
RX	receiver

Abbreviation	Definition
S/C	spacecraft
SCLK	Spacecraft Clock Kernel
SHARAD	Mars SHAllow RADar sounder
SNR	Signal-to-Noise Ratio
SP	Specular Point
SPICE	Spacecraft, Planet, Instrument, “C-matrix”, Events
SPK	Spacecraft and Planet Kernel
SPM	Small Perturbation Method
TDB	Barycentric Dynamical Time
TGO	ExoMars Trace Gas Orbiter
TX	transmitter
UHF	Ultra-high frequency
UTC	Coordinated Universal Time
WAF	Woodward Ambiguity Function

List of Symbols

Symbol	Definition	Unit
B	Receiver bandwidth	Hz
B_t	Bandwidth of transmitter signal	Hz
C	Roughness parameter of the Hagfors' law	-
D_x	Divergence factor caused by planet's curvature	-
D_y	Divergence factor caused by planet's curvature	-
G_r	Receiver antenna gain (pattern)	-
G_t	Transmitter antenna gain (pattern)	-
N_{inc}	Number of incoherent accumulations	-
P_N	Noise power	W
P_t	Transmitter power	W
P_{direct}	Direct signal power	W
P^r_{pq}	Total scattering/reflected power measured by the receiver	W
P^{coh}_{pq}	Coherent component of scattering/reflected power measured by the receiver	W
P^{incoh}_{pq}	Incoherent component of scattering/reflected power measured by the receiver	W
R_a	Rayleigh parameter	-
$R_{r,sp}$	Distance between receiver and specular point	m
$R_{t,sp}$	Distance between transmitter and specular point	m
R_{tr}	Distance between transmitter and receiver	m
T_N	Receiver antenna noise temperature	K
T_c	Coherent integration time.	s
Y^c	Amplitude of correlation using conventional GNSS-R	a.u.
Y^i	Amplitude of correlation using interferometric GNSS-R	a.u.
Γ_{pq}	Coherent reflectivity (polarization dependent)	-
χ^2	Woodward Ambiguity Function	-
ϵ_r	Relative permittivity	-
γ	Facet tilt angle required for specular reflection	deg
λ	Wavelength of transmitter signal	m
$\mathfrak{R}_{pq}$	Fresnel reflection coefficient (polarization dependent)	-
ψ	Surface roughness loss, accounts for the loss of coherent power due to diffused scattering	-
ρ_{pq}	Reflectivity (polarization dependent)	-
σ^0_{pq}	The (polarization dependent) normalized bistatic radar cross section	-
σ_h	Root Mean Square surface height	-
θ_i	Incidence angle	deg
$a(t)$	locally generated replica of the transmitted signal	V or W
c	Speed of light in vacuum.	m/s
k	Wavenumber of transmitter signal	rad/m
k_B	Boltzmann's constant	J/K
$s_d(t)$	direct signal	V or W
$s_r(t)$	reflected signal	V or W

1 Introduction

1.1. Project Context, Motivation and Relevance

For centuries Mars has been a topic of interest to scientists. Mars's geology, atmosphere, and climate history provide crucial insight into the evolution of planetary environments and into the understanding of our own planet Earth. The search for water on Mars is a central theme of research, being important both for the possibility of the existence of life and for future human exploration of Mars. Thus there is a huge variety of reasons why Mars is studied so intensively. Over the years, numerous measurements have taken place at Mars, one of these being mutual radio occultation measurements.

During mutual radio occultation measurements at Ultra-high frequency (UHF), between Mars Express (MEX) and the ExoMars Trace Gas Orbiter (TGO), a significant return signal arriving from the surface of Mars was observed (partially due to an incorrect switch-on time of the instruments). This unexpected result opened up opportunities to look into the possibilities of using reflectometry measurements between MEX and TGO to research the Martian (sub)surface, especially the water(-ice) content as the used frequency has a penetration depth of about a meter below the surface. Thus, in 2025 the European Space Agency (ESA) has started so called bistatic radar experiments (with MEX transmitting and TGO receiving) [41].

Nieuwenhuizen [35] conducted an initial investigation into the modeling of bistatic measurements between MEX and TGO and deriving (sub)surface water content. Several recommendations were made for follow-up research, and one of the goals of this thesis is to follow these recommendations to create an improved bistatic measurement model.

In addition to this, this thesis will also investigate whether reflectometry techniques presently used with Earth remote sensing can be applied to Mars bistatic radar measurements. Specifically, the remote sensing technique GNSS-Reflectometry (GNSS-R) will be explored. GNSS-R is a remote sensing technique that utilizes signals from Global Navigation Satellite Systems (GNSSs) reflected off the Earth's surface, with the primary purpose of GNSS-R being to extract valuable environmental data by analyzing these reflected GNSS signals [16]. GNSS-R is being used in a wide variety of applications, including monitoring ocean surface roughness, soil moisture, snow depth, vegetation growth, and even detecting natural hazards [16]. GNSS-R measurements have now been employed for several years, where a large number of satellite navigation signals, after reflection from the Earths surface (solid or liquid), are being recorded by various lower orbiting spacecraft. Moreover ESA has launched a dedicated spacecraft for this purpose in 2025 (Hydro-GNSS) [14], underlying the relevance of GNSS-R.

1.2. Research Questions and Objectives

This thesis aims to create an (improved) model to simulate bistatic reflectometry measurements between MEX and TGO (taking into account recommendations from Nieuwenhuizen [35]). The main goal is to try to use the Mars Digital Elevation Model (DEM) created from Mars Orbiter Laser Altimeter (MOLA) data at its full resolution (128 pixels per degree). Moreover this thesis will investigate the the-

oretical background of GNSS-R to potentially identify areas where GNSS-R principles can be applied to bistatic measurements on Mars. It also aims to investigate optimal configurations for future bistatic measurements based on simulation of MEX-TGO bistatic measurements.

In order to accomplish these goals, there are several research questions that this thesis aims to answer. These questions are divided into two high-level questions, which outline the overarching themes, investigated in this thesis. These high level research questions also come with several sub-questions which are more specific questions that help to break down and address each main question in detail.

RQ 1: *How can a set of Mars bistatic radar measurements between MEX and TGO be modeled to use the (full resolution) Mars MOLA DEM?*

- ***RQ 1.1:*** *How do the modeled bistatic radar measurements of MEX-TGO compare to the initial model created by Nieuwenhuizen [35] and the actual MEX-TGO measurement data?*
- ***RQ 1.2:*** *Where can GNSS-R principles/techniques be applied to Mars bistatic radar measurements?*

RQ 2: *What are key parameters for future measurements to obtain the optimal received signal?*

- ***RQ 2.1:*** *How do (instrumentation/geometry) parameters like spacecraft pointing, antenna polarization, permittivity, etc. influence the received signal?*
- ***RQ 2.2:*** *When are there suitable opportunities for bistatic measurements for 2026, with MEX and TGO?*

1.3. Structure of the Thesis

This thesis is structured as follows. Having defined the project context and the research goals/questions here in chapter 1, the theoretical background for this thesis is presented in chapter 2 by discussing the key concepts that will be used in the bistatic measurement simulation and analysis of these simulations. Chapter 3 explains the model used to search for bistatic measurement geometries and determine their relevant geometry parameters (e.g. specular point coordinates). Then chapter 4 discusses the bistatic measurement simulation model created to simulate MEX-TGO measurements. The results of the performed MEX-TGO bistatic measurement simulations are presented and discussed in chapter 5. Finally, the conclusions of this thesis are presented in chapter 6 together with recommendations for future investigations.

The code for the bistatic geometry search and bistatic measurement simulation scripts is available on the following public GitHub repository: `https://github.com/nbeugel/MSc-thesis-Simulation-of-Reflectometry-Measurements-between-MEX-and-ExoMarsTGO`

2

Theoretical Background

This chapter presents the theoretical background on for this thesis. First the basics of GNSS-R as investigated in the literature study of this thesis will be discussed in section 2.1. Then the characterization of surface properties and their influence on the reflected signal will be explored in section 2.2. Next the Delay-Doppler Map (DDM) observable will be discussed in section 2.3. This is then followed by section 2.4 where the modeling of the bistatic signal power will be explained and section 2.5 where relevant scattering coefficient models are introduced. Lastly, the spatial resolution of bistatic measurements is discussed in section 2.6.

2.1. Basics of GNSS-R

2.1.1. Working principle of GNSS-R

GNSS constellations are groups of satellites designed to provide position, velocity, and timing information for use on Earth and, to some extent, in space [53]. These GNSS signals can be used for Earth remote sensing. GNSS-Reflectometry (as the name implies) is a remote sensing technique that measures reflected signals (either from liquid or from solid surfaces) coming from GNSS satellites, which are collected by a GNSS-R receiver (as well as sometimes the corresponding direct signals [26]). For the purpose of this thesis, only spaceborne GNSS-R receivers (so bistatic radar systems) are relevant. An example of a bistatic (GNSS-R) configuration can be seen in figure 2.1.

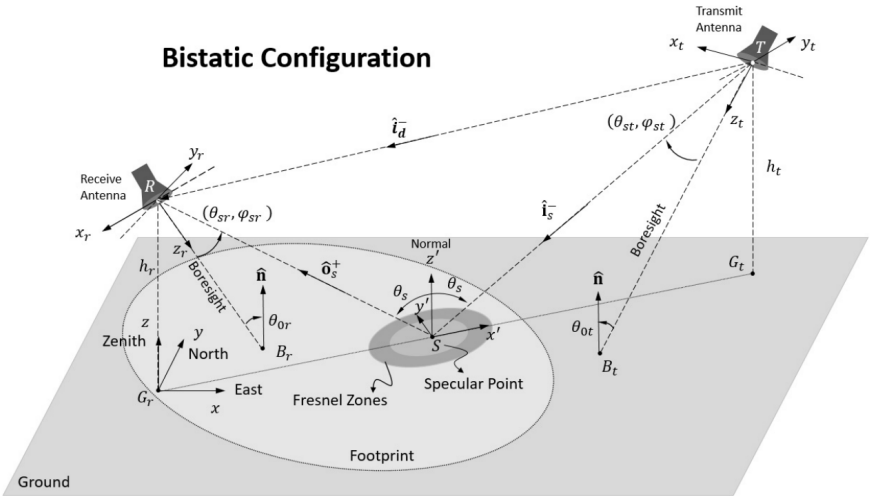

Figure 2.1: Arbitrary bistatic antenna configuration. (Image source: [28])

GNSS-R can be used for measuring several environmental properties, such as soil moisture, snow/ice depth, vegetation, and sea level. So there are applications in many subjects [8]. For this thesis soil

moisture detection is a particularly interesting application as the detection of water on Mars is an important topic in planetary sciences.

2.1.2. Specular point

For the bistatic radar measurement geometry, the specular point is an important location. The SP is the surface's exact location where the specular reflections take place (see again figure 2.1). Theoretically, it is defined as the point where the incident angle and the reflection angle (sometimes called scattering or emission angle) are equal in the plane that includes both transmitter and receiver, making the waves coming from a single direction be reflected in another single direction as well [8].

2.1.3. Delay and Doppler shift

Two other useful parameters for a (GNSS-R) bistatic measurement are the delay and Doppler shift. At any point on the surface p, the reflection path length is given by the distance from the transmitting spacecraft to p plus the distance from the p to the receiving spacecraft:

$$\left|\overrightarrow{TpR}\right| = \left|\overrightarrow{Tp}\right| + \left|\overrightarrow{pR}\right| \tag{2.1}$$

The signal path delay for a point p (assuming free-space propagation) is then:

$$t' = \frac{\left|\overrightarrow{TpR}\right|}{c} \tag{2.2}$$

with c being the speed of light in vacuum.

The Doppler frequency shift can be expressed as a function of the rate of change of the reflection path length [23]:

$$f_D = \frac{1}{\lambda}\left(-\frac{d|\overrightarrow{TpR}|}{dt}\right) = \frac{1}{\lambda}\left(\vec{v_t}\cdot\frac{\overrightarrow{Tp}}{|\overrightarrow{Tp}|} - \vec{v_r}\cdot\frac{\overrightarrow{pR}}{|\overrightarrow{pR}|}\right) \tag{2.3}$$

where λ is the transmitter signal wavelength; $\vec{v_t}$ is the transmitter velocity vector; and $\vec{v_r}$ is the receiver velocity vector. Note that equation (2.3) assumes a body-fixed reference frame (surface points are stationary for each time step).

2.1.4. GNSS-R receiver data acquisition techniques

There are two main GNSS-R techniques/architectures:

- conventional GNSS-R (cGNSS-R)
- interferometric GNSS-R (iGNSS-R)

With cGNSS-R, the reflected signal $s_r(t)$ is correlated with a locally generated replica of the transmitted signal $a(t)$ (GNSS-R of course uses signals from GNSS satellites which use Pseudo-Random Noise (PRN) codes) over a period equal to the coherent integration time T_c (typically 1 ms). The amplitude of the correlation Y^c can be written as shown in equation 2.4 [26, 53].

$$Y^c(\tau, f_d) = \frac{1}{T_c}\int_{t_0}^{t_0+T_c} s_r(t)a^*(t-\tau)e^{-2\pi j(f_c+f_d)t}dt \tag{2.4}$$

where t_0 is the start time of the correlation, f_c is the carrier frequency, $*$ denotes the complex conjugate operation, τ is the delay and f_d is the Doppler shift.

With iGNSS-R, the reflected signal $s_r(t)$ is correlated with the received direct signal $s_d(t)$ instead of a locally generated replica (again over a period equal to the coherent integration time T_c), see figure 2.2. The amplitude of this correlation Y^i can be written as shown in equation 2.5 [26, 53]:

$$Y^i(\tau, f_d) = \frac{1}{T_c}\int_{t_0}^{t_0+T_c} s_r(t)s_d^*(t-\tau)e^{-2\pi j(f_c+f_d)t}dt \tag{2.5}$$

Additionally, in order to improve the correlation amplitude (reduce the influence of thermal and speckle noise), an incoherent average can be used (equation (2.6)) [53]:

$$\langle |Y(\tau, f_d)|^2 \rangle \approx \frac{1}{N_{inc}} \sum_{i=1}^{N_{inc}} |Y(\tau, f_d)|^2 \tag{2.6}$$

where, N_{inc} is the number of incoherent accumulations.

An illustration of the configuration of the two techniques is shown in figure 2.2. For the MEX-TGO measurements no PRN code is used, so during this thesis the signal correlations were not utilized.

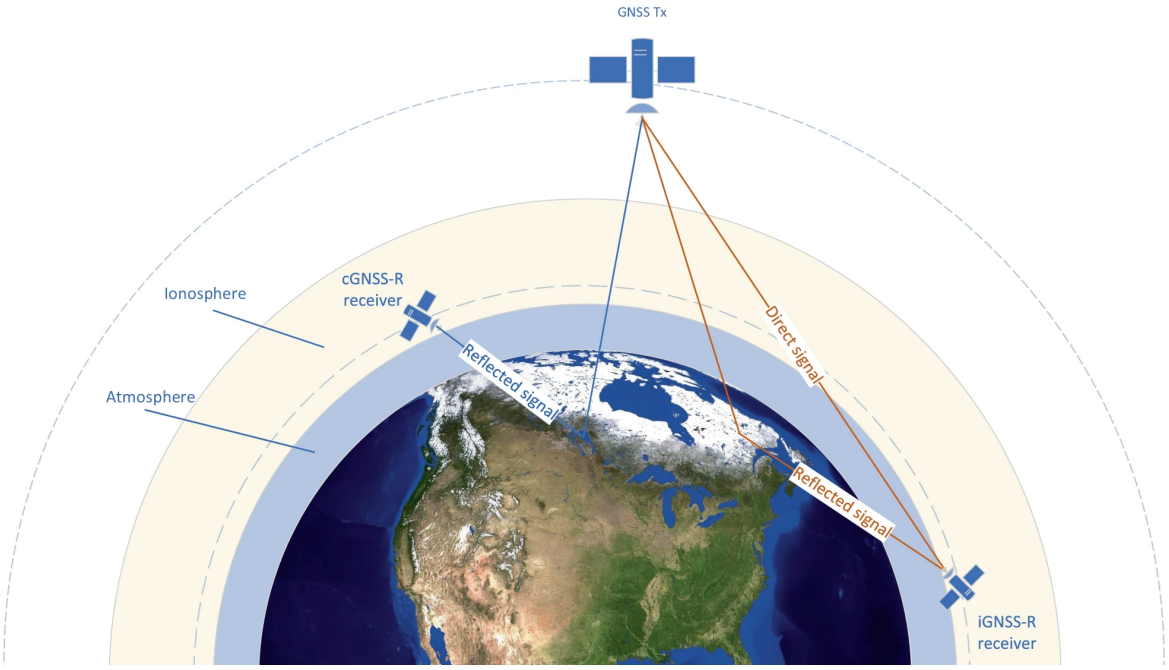

Figure 2.2: GNSS-R Measurement geometry. Left side cGNSS-R, Right side iGNSS-R (Image source [10])

2.2. Soil Surface Characterization

Because signals in bistatic measurements reflect off the surface, it is important to characterize the surface in terms of its dielectric and geometrical properties. How much of the signal is reflected by the soil is (for a large part) determined by by the Fresnel reflection coefficients, that depend on the polarization of the incident wave and the dielectric properties of the soil. These will be explored in subsection 2.2.1. However, there are other parameters that also influence the reflectivity/scattering. For natural terrains, which are not perfectly flat, the roughness of the surface also plays an important role in the scattering process and this will be discussed in subsection 2.2.2.

As the reflectivity (and therefore the received power) are dependent on the soil properties, it is important to note what information can be extracted from bistatic measurements. In general soil is a mixture of air, bulk soil, bound water, and free water. This means that the dielectric properties of the soil will differ slightly based on the soil humidity level. A (semi-empirical) model based on a dielectric mixing approach can therefore be used to approximate the water content inside the soil (if the soil composition is known).

2.2.1. Fresnel Reflection Coefficients & reflectivity

For GNSS satellites (and also for the MEX MELACOM UHF radio), the transmitted signals are Right Hand Circular Polarized (RHCP). RHCP signals can be interpreted as a linear combination of horizontal and vertical polarization components (with a 90 degree phase offset).

The Fresnel reflection coefficients for vertical and horizontal polarizations for plane waves incident from medium 1 onto medium 2 with a non-magnetic interface (i.e. $\mu_r = 1$) are given by [24]:

$$\Re_{HH} = \frac{\cos(\theta_i) - \sqrt{\epsilon_r - \sin^2(\theta_i)}}{\cos(\theta_i) + \sqrt{\epsilon_r - \sin^2(\theta_i)}} \tag{2.7}$$

$$\Re_{VV} = \frac{\epsilon_r \cos(\theta_i) - \sqrt{\epsilon_r - \sin^2(\theta_i)}}{\epsilon_r \cos(\theta_i) + \sqrt{\epsilon_r - \sin^2(\theta_i)}} \tag{2.8}$$

where θ_i is the incidence angle, $\epsilon_r = \epsilon_{r2}/\epsilon_{r1}$ with ϵ_{r2} being the complex permittivity of medium 2 (the soil) and ϵ_{r1} being the complex permittivity of medium 1 (the air).

The cross and co-polarization Fresnel coefficients for Left Hand Circular Polarized (LHCP) and RHCP can then be written as [8]:

$$\Re_{RL} = \Re_{LR} = \frac{1}{2}(\Re_{VV} - \Re_{HH}) \tag{2.9}$$

and

$$\Re_{RR} = \Re_{LL} = \frac{1}{2}(\Re_{VV} + \Re_{HH}) \tag{2.10}$$

With the Fresnel reflection coefficients, the reflectivity can be determined. The reflectivity (without the influence of vegetation and surface roughness) is computed as the squared modulus of the (complex) Fresnel reflection coefficient [25, 50], see equation (2.11).

$$\rho_{pq} = |\Re_{pq}|^2 \tag{2.11}$$

where the scattered and incident polarization are denoted by p and q The reflectivity represents the ratio of reflected to incident intensity and will be used in the Hagfors' scattering model (which is discussed in section 2.5.2).

The effects of varying permittivities and incidence angles on the reflectivity are shown in figure 2.3. Note that this figure shows the elevation angle (reciprocal of incidence angle). The figure shows that for the rl (left hand to right hand circular polarization) signal reflectivity a larger surface permittivity increases the reflectivity and a smaller incidence angel (larger elevation angel) gives a higher reflectivity. For the rr (right hand to right hand circular polarization) signal reflectivity this is reversed. A larger surface permittivity decreases the reflectivity and a smaller incidence angel (larger elevation angel) gives a very low reflectivity for rr. This is important to keep in mind as the co-polarizations of the MEX and TGO antennas are both RHCP.

2.2.2. Surface Roughness

As stated earlier, the geometrical properties of the surface (i.e. the surface roughness) play an important role in the scattering process. For a perfectly smooth surface illuminated by a plane wave, the energy is reflected solely into the specular direction with scattering amplitude equal to the Fresnel reflection coefficients [11] (see figure 2.4 (a)). But as the surface roughness increases, the diffuse (non-coherent) scattering component becomes more dominant and the scattered energy is reradiated in many directions (figure 2.4 (b), (c) and (d)). This means the scattered energy in the specular direction decreases as the surface gets rougher.

The precise characterization of natural terrain is a difficult task. Therefore, to model the scattering it is common to approximate the surface elevation as a stationary stochastic process with a Gaussian height distribution [11].

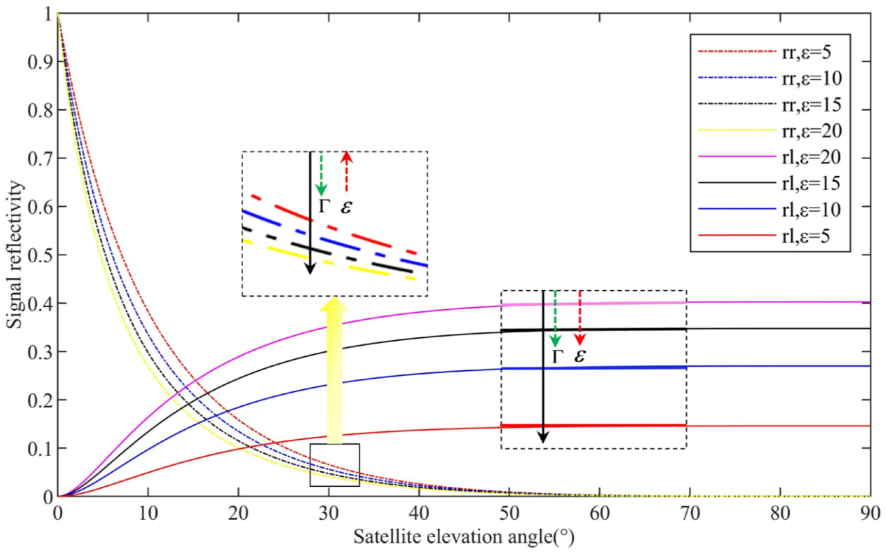

Figure 2.3: Schematic diagram of reflectivity variation. In the (zoomed) boxes, the red and green arrows indicate the direction of decreasing reflectivity (Γ) and decreasing relative permittivity (ε). The (size of the) black arrows highlight the total range of variation in the signal range. (Image source: [50])

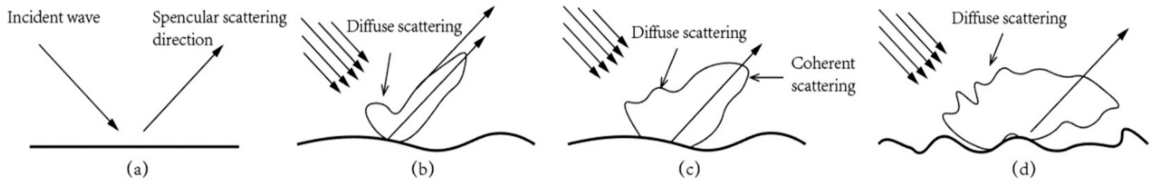

Figure 2.4: Electromagnetic wave scattering from several different rough surfaces. (a) specular surface.; (b) slightly rough surface; (c) medium rough surface; (d) rough surface. (Image source: [49])

2.3. Delay-Doppler Map observable

One of the main products of GNSS bistatic radar is the so-called Delay-Doppler Map (DDM) of the scattered signal [53]. The DDM is a 2D map which shows the strength of the reflected signal as function of the signal delay and signal Doppler shift. DDMs can provide information about the reflecting surface, such as surface roughness, moisture content, and more [16]. The concept of delay-Doppler mapping is shown in figure 2.5.

The DDMs can be modeled as the sum of both coherent and incoherent contributions [46, 4]:

$$\langle |Y(\tau, f_d)|^2 \rangle = \langle |Y_{pq}^{\text{coh}}(\tau, f_d)|^2 \rangle + \langle |Y_{pq}^{\text{inc}}(\tau, f_d)|^2 \rangle \tag{2.12}$$

2.3.1. DDM coherent component

The coherent component is defined for an incident signal with the scattered and incident polarization p and q [4]:

$$\langle |Y_{pq}^{\text{coh}}(\tau, f_d)|^2 \rangle = \frac{P_t G_t \lambda^2 G_r |\chi^2(\tau, f_d)|}{(4\pi)^2 (R_{t,sp} + R_{r,sp})^2} \Gamma_{pq}(\theta) \tag{2.13}$$

where P_t is the transmitter power; G_t is the transmitter gain; G_r is the receiver antenna gain; $R_{t,sp}$ is the distance between the transmitter and the specular point; $R_{r,sp}$ is the distance between the receiver and the specular point; λ is the transmitter signal wavelength; χ^2 is the Woodward Ambiguity Function (WAF) (see section 2.3.3) and $\Gamma_{pq}(\theta)$ is the coherent reflectivity at the angle of incidence (θ), which is defined in equation (2.14) [4, 29].

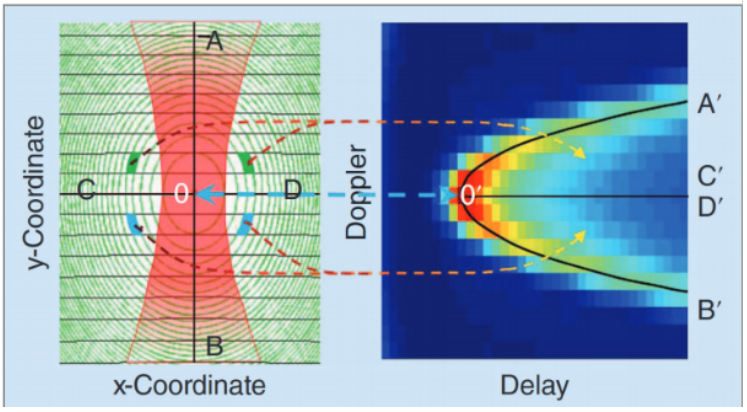

Figure 2.5: A concept of delay-Doppler mapping. The direction of flight is along the x-axis. (Image source: [53])

$$\Gamma_{pq}(\theta) = \psi|\Re_{pq}|^2 = \mathsf{exp}(-R_a^2)|\Re_{pq}|^2 = \mathsf{exp}(-(2k\sigma_h\cos(\theta))^2)|\Re_{pq}|^2 \tag{2.14}$$

where $\Re_{pq}$ is the Fresnel reflection coefficient; and ψ is the surface roughness loss, which accounts for the loss of coherent power due to diffuse scattering. R_a is the Rayleigh parameter (indication of surface roughness relative to the signal wavelength), k is the transmitter signal wavenumber, and σ_h is the Root Mean Square (RMS) surface height.

2.3.2. DDM incoherent component

A widely used model for the incoherent component of the DDM, derived from the Kirchoff Approximation to Geometric Optics (KA-GO), can be written as a surface integral [52, 46]:

$$\langle|Y_{pq}^{\mathsf{inc}}(\tau, f_d)|^2\rangle = \frac{\lambda^2 P_t}{(4\pi)^3}\iint \frac{G_t(\vec{\rho})G_r(\vec{\rho})}{R_t(\vec{\rho})^2 R_r(\vec{\rho})^2}|\chi^2(\vec{\rho};\delta\tau,\delta f_d)|\sigma_{pq}^0(\vec{\rho})d^2\vec{\rho} \tag{2.15}$$

where the variable of integration ρ is the positioning vector of the scattering point; P_t is the transmitter power; G_t is the transmitter gain; G_r is the receiver antenna gain; $R_t(\vec{\rho})$ is the distance between the transmitter and point ρ; $R_r(\vec{\rho})$ is the distance between the receiver and point ρ; λ is the transmitter signal wavelength; σ_{pq}^0 is the incoherent Normalized Bistatic Radar Cross Section; and χ^2 is the WAF. In literature this model for the incoherent component of the DDM is usually referred to as the Zavorotny-Voronovich model [52].

To accelerate computation, equation (2.15) can be formulated as a 2D convolution [12, 31] which can then be efficiently computed by a fast Fourier transform (FFT):

$$\langle|Y_{pq}^{\mathsf{inc}}(\tau, f_d)|^2\rangle = \Sigma(\tau, f_d) * *\chi^2(\tau, f_d) \tag{2.16}$$

where the sigma matrix $\Sigma(\tau, f_d)$ contains the product of the surface integral without the WAF for a given delay and Doppler shift.

2.3.3. Woodward Ambiguity Function

$\chi^2(\delta\tau, \delta f)$ is known in radar terminology as the Woodward Ambiguity Function (WAF). The WAF is essentially a function that describes how well a specific signal waveform can simultaneously distinguish the distance and speed of a target.

$\chi(\delta\tau, \delta f)$ is defined as:

$$\chi(\delta\tau, \delta f) = \frac{1}{T_c}\int_0^{T_c} a(t)a^*(t-\delta\tau)\mathsf{exp}(-2\pi i(\delta f)) \tag{2.17}$$

For a GNSS PRN code the WAF can be approximated by:

$$\text{WAF}(\vec{\rho};\delta\tau,\delta f) = \chi^2(\vec{\rho};\delta\tau,\delta f) \approx \Lambda^2(\delta\tau)S^2(\delta f) \tag{2.18}$$

where $\Lambda(\delta\tau)$ and $S(\delta f)$ are weighting functions in the delay and Doppler domain, respectively:

$$\Lambda(\delta\tau) = \begin{cases} 1 - \frac{|\delta\tau|}{\tau_c} & \text{if } |\tau| \leq \tau_c \\ 0 & \text{if } |\tau| > \tau_c \end{cases} \tag{2.19}$$

where $\delta\tau$ is the difference of the selected delay τ and the delay $\tau(\vec{\rho})$ of any point on the surface at $\vec{\rho}$.

$$S(\delta f) = \frac{1}{T_c}\int_0^{T_c} \exp(-2\pi i(\delta f)) = \frac{\sin(\pi\delta f T_c)}{\pi\delta f T_c} e^{-\pi i\delta f T_c} = \text{sinc}(\delta f T_c) e^{-\pi i\delta f T_c} \tag{2.20}$$

where δf is the difference of the selected Doppler shift f and the Doppler shift $f_D(\vec{\rho})$ of any point on the surface at $\vec{\rho}$.

The ambiguity function within the power Delay Doppler Map expression selects the region of the glistening zone that contributes to the power at a given delay τ and Doppler shift f_d bin, and masks out the other surface points [30]. When the WAF is taken into account, the power value for each delay-Doppler pixel becomes the weighted sum of the power scattered from the corresponding spatial area, plus that from a number of adjacent areas. This spreading effect is caused by the WAF of pseudorandom GPS sequences [6]. The spreading effect reduces for a narrower WAF, and an ideal ambiguity function would be a 2-dimensional Dirac delta function $\chi(\tau, f) = \delta(\tau)\delta(f)$ (which would have no ambiguities at all).

2.4. Modeling of bistatic signal power

2.4.1. Scattering/Reflected Power

As discussed earlier, an incident wave that reflects on a rough surface is partly reflected in the specular direction and partly scattered in all directions. These are referred to as the coherent component and the diffuse/incoherent scattering component respectively.

In general, the total scattering/reflected power measured by a bistatic radar receiver P_{pq}^r is composed of a coherent and incoherent component: [9]:

$$P_{pq}^r = P_{pq}^{\text{coh}} + P_{pq}^{\text{incoh}} \tag{2.21}$$

where subscripts p and q denote the scattered and incident polarization respectively, and P_{pq}^{coh} and P_{pq}^{incoh} are the power of the coherent and incoherent components.

The coherent power component can be written as [9]:

$$P_{pq}^{\text{coh}} = \frac{P_t G_t \lambda^2 G_r}{(4\pi)^2 (R_{t,sp} + R_{r,sp})^2} \Gamma_{pq}(\theta) \tag{2.22}$$

where P_t is the transmitter power; G_t is the transmitter gain; G_r is the receiver antenna gain; $R_{t,sp}$ is the distance between the transmitter and the specular point; $R_{r,sp}$ is the distance between the receiver and the specular point; λ is the transmitter signal wavelength; and $\Gamma_{pq}(\theta)$ is the coherent surface reflectivity at the angle of incidence (θ)

The incoherent power component, assuming a bistatic scattering coefficient σ_{pq}^0 is given by the bistatic radar equation [9, 11]:

$$P_{pq}^{\text{incoh}} = \frac{P_t \lambda^2}{(4\pi)^3} \iint_A \frac{G_t(\vec{\rho}) G_r(\vec{\rho})}{R_t(\vec{\rho})^2 R_r(\vec{\rho})^2} \sigma_{pq}^0(\vec{\rho}) d^2\vec{\rho} \tag{2.23}$$

where the variable of integration ρ is the positioning vector of the scattering point; P_t is the transmitter power; G_t is the transmitter gain; G_r is the receiver antenna gain; $R_t(\vec{\rho})$ is the distance between the

transmitter and point ρ; $R_r(\vec{\rho})$ is the distance between the receiver and point ρ; λ is the transmitter signal wavelength; and σ^0_{pq} is the incoherent Normalized Bistatic Radar Cross Section.

The incoherent power near the specular point can be approximated by [2, 50]:

$$P^{\text{incoh}}_{pq}(\tau \approx 0, f \approx 0) = \frac{P_t \lambda^2 G_t G_r}{(4\pi)^3 R_t^2 R_r^2} \sigma^0_{pq} A_{eff} \tag{2.24}$$

where the effective area A_{eff} is given by:

$$A_{eff} = \frac{2\pi}{3} G_{1x} G_{1y} = \pi \left(\frac{G_{1m}}{2} \right)^2 \tag{2.25}$$

$$G_{1x} = \frac{1}{D_x \cos(\theta)} \sqrt{\frac{2cR_tR_r}{B_t(R_t + R_r)}} \tag{2.26}$$

$$G_{1y} = TG_{1x} \tag{2.27}$$

$$T = \frac{D_x}{D_y} \cos(\theta) \tag{2.28}$$

where c represents the speed of light, and B_t represents the bandwidth of the transmitted signal; and where D_x and D_y represent "divergence factors" caused by the planet's curvature (see appendix A.1).

The total received power $P_{\text{tot,DD}}$ over a given Delay-Doppler interval can be expressed as equation (2.29) [7].

$$P_{\text{tot,DD}} = \sum_{l=1}^{L} \sum_{m=-M}^{M} P_{\text{DDM}}(\tau_l, f_{D,m}) \tag{2.29}$$

2.4.2. Direct Power

Besides the reflected signal, the total received signal also contains a direct signal component (see again figure 2.2). Depending on the geometry of the specific measurement, this could be a significant part of total received signal, so it's important to take it into consideration when trying to model the total received power. According to the free space propagation model the direct signal power P_{direct} is given by equation (2.30) [25, 50].

$$P_{\text{direct}} = \frac{P_t G_t G_r \lambda^2}{(4\pi)^2 R_{tr}^2} \tag{2.30}$$

where P_t is the transmitter power; G_t is the transmitter gain; G_r is the receiver antenna gain; R_{tr} is the distance between the transmitter and the receiver; and λ is the transmitter signal wavelength.

2.4.3. Noise Power

For the received signal the noise power also has to be considered. If it is assumed that there the thermal noise is dominant, the noise power P_N can be computed with equation (2.31).

$$P_N = k_B T_N B \tag{2.31}$$

where k_B is the is the Boltzmann's constant, B is the receiver bandwidth, and T_N is the receiver antenna noise temperature.

2.5. Bistatic scattering coefficient models

Computing the incoherent power/DDM contribution requires a model to compute the bistatic scattering coefficient (bistatic radar cross section). These models are typically obtained by adopting different approximations on the equations describing the interaction of the incident electromagnetic field with a random surface [11]. There are several scattering models that are used to model the bistatic radar coefficient in GNSS-R (with a short overview given in section 2.5.1). However, in planetary sciences Hagfors' law is often used, which will be discussed in section 2.5.2 and this is the scattering model that will be used in this thesis.

2.5.1. Scattering models in GNSS-R

The most common models in literature for GNSS-R to obtain the scattering coefficients are the Kirchhoff Approximation, under the Physical Optics (KA-PO) and Geometric Optics (KA-GO) solutions, the Small Perturbation Method (SPM) and the Integral Equation Model (IEM) [11]. A quick overview of these methods is given below:

- KA-GO: Simplification of the Kirchhoff approximation where only those facets from the reflecting surface that allow local specular reflection will contribute to the scattered field, thus excluding local diffraction effects [15].
- KA-PO: Compared to KA-GO, this approach not only considers the contribution of the scattered fields over the well oriented surfaces, but also it considers the totality of contributions of the scattering fields over the whole rough surface [8].
- SPM: It is based on formulating the scattering as a partial differential equation boundary value problem and to find a solution in terms of plane waves that matches the surface boundary conditions [22].
- IEM: This method can be viewed as an extension of the Kirchhoff method and the SPM, as it reproduces the results of these methods for their appropriate limits [22].

2.5.2. Hagfors' Law

Another scattering model is the Hagfors' model which is often used in planetary sciences as it provides good agreement with a variety of observations [40]. As Hagfors' law is an empirical model it describes the total scattering cross section (so not only the incoherent part). So for the calculation of the reflected power with Hagfors' law, equation (2.23) is used. Another important thing to note about Hagfors' law is that it assumes an exponential height autocorrelation function, which is non-physical, meaning that energy is not conserved [40, 45]. Hagfors' law is described by equation (2.32) [20, 40].

$$\sigma_{0,pq} = \frac{\rho_{pq} C}{2} (\cos^4(\gamma) + C \sin^2(\gamma))^{-3/2} \tag{2.32}$$

where ρ_{pq} is the reflectivity (as given by equation (2.11)), γ is the facet tilt angle at the location of interest required for specular reflection (also referred to as the 'required tilt angle' in this thesis) [36] and the width/roughness parameter C provides a measure of the angular extent of the backscattering lobe and hence the roughness of the surface [40] and is typically interpreted as the inverse RMS surface slope squared.

$$C = s_{\text{RMS}}^{-2} \tag{2.33}$$

Hagfors' law was originally derived for monostatic radar geometries. (So the required tilt angle would just be the incidence angle). However monostatic scattering models can be modified so they also can be applied to bistatic radar geometries (bistatic theorem) [19]. The functional form of monostatic scattering models can be used in bistatic radar geometries by replacing the monostatic incidence angle with the bistatic bisector angle (see figure 2.6). To account for the reflection coefficient dependence on incidence angle, the bistatic scattering model equivalent takes the reflectivity at the incidence angle $\rho_{pq}(\theta_i)$ (where for a monostatic radar geometry the reflectivity is taken at normal incidence $\rho_{pq}(0)$) [19].

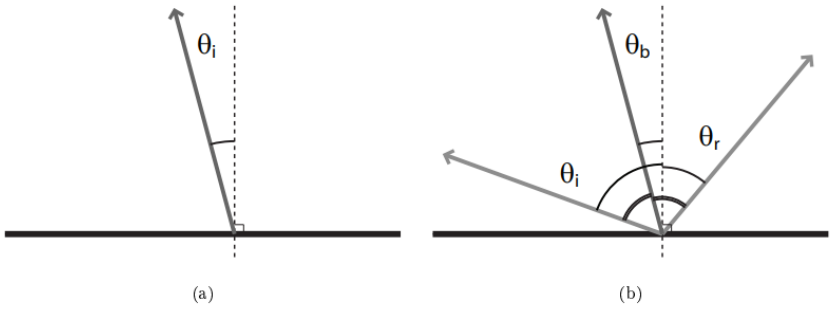

Figure 2.6: (a) Monostatic radar geometry, defined by the incidence angle θ_i. (b) Equivalent bistatic radar geometry. The incidence and reflection angles, θ_i and θ_r , define a bisector angle, θ_b, that is equivalent to the monostatic incidence angle. (Image source: [19])

2.6. Spatial resulution & Fresnel zones

If the surface geometry of the bistatic measurement is such that the Rayleigh parameter (R_a) of the rough surface is smaller than unity, then the specular reflection is dominant, and therefore, the spatial resolution of the bistatic GNSS-R radar will be limited to the first Fresnel zone [53]. The first Fresnel zone (assuming a flat surface) is given by an ellipse with semi-major axis a and semi-minor axis b, see equations (2.34a) and (2.34b) [21].

$$b = \sqrt{\lambda \frac{R_{t,sp} R_{r,sp}}{R_{t,sp} + R_{r,sp}}} \tag{2.34a}$$

$$a = \frac{b}{\cos \theta_i} \tag{2.34b}$$

Diffuse, quasi-specular scattering is the more frequently occurring process when dealing with natural surfaces. In this case, scattered radio waves arrive from the “glistening” zone, which is much larger than the first Fresnel zone [53].

3

Bistatic geometry search

In this chapter the numerical model is discussed that was created to search and determine viable bistatic measurement geometries and compute relevant quantities related to these geometries. First of all section 3.1 discusses the requirements/constraints that need to be satisfied for a feasible bistatic measurement geometry. Then, sections 3.2 and 3.3 present a description and the architecture of the bistatic geometry search model respectively. Lastly, section 3.4 explains the process of how the specular point for a bistatic geometry is acquired.

3.1. Requirements and constraints

There are several constraints that need to be satisfied for a measurement geometry to be considered feasible. Due to the numerical nature of the model, the constraints have been implemented using certain tolerances.

Requirements for the SP to have a valid bistatic measurement geometry:

REQ-BMG-1: The difference between the incidence angle and emission angle (of the found SP) shall be less than 0.1°.

REQ-BMG-2: The angle between the SP surface normal and TX-SP-RX plane shall be less than 0.1°.

REQ-BMG-3: The SP should always be visible (unobstructed line of sight) for both the transmitter (TX) and receiver (RX).

Besides these constraints, there are also several geometric requirements/constraints that were imposed to eliminate measurement opportunities which would result in an unreasonably low received signal power level (and thus a poor Signal-to-Noise Ratio (SNR)).

REQ-BMG-4: The total signal path length (distance TX to SP + distance SP to RX) shall be less than $3500\,\mathrm{km}$. *This requirement ensures that the free-space path loss does not become too big, as it scales with the distance squared*

REQ-BMG-5: The incidence angle of the SP shall be between 30° and 85°. *This requirement ensures reflectivity does not become too low. MEX and TGO transmit and receive RHCP signals and the RHCP to RHCP Fresnel coefficient decreases significantly for small incidence angles. The upper bound for the incidence angle is there to prevent undesired signal scattering, associated with shallow measurement geometries. Low elevation angles (<5°), are discarded by most, if not all, GNSS-R satellites for Earth [47].*

Finally, a requirement on the minimum measurement duration has been set to ensure data quality and scientific meaningful measurements.

REQ-BMG-6: The measurement duration shall be at least 1 minute.

3.2. Model description

One of the research objectives was to investigate suitable opportunities for bistatic radar measurements between MEX and TGO. Another objective was the modeling of bistatic radar measurements. Both require information about the the time and location of feasible bistatic measurement geometries. Therefore a numerical model for searching viable bistatic geometries and determining the specular point position of these geometries was implemented in Python.

3.2.1. SPICE toolkit

The numerical model uses the Spacecraft, Planet, Instrument, "C-matrix", Events (SPICE) toolkit, an information system which provides access and tools to interact with planetary and spacecraft ephemeris and ancillary engineering information [1]. The SPICE toolkit can be used to compute many kinds of observation geometry parameters, including the ephemerides, orientations, sizes, and shapes of planets, satellites, comets and asteroids [32]. As the numerical model is written in Python, the SpiceyPy package [1], a Python wrapper for the SPICE toolkit was used.

SPICE data files are typically referred to as kernels. These kernels provide information for spacecraft and target body trajectory (ephemeris), orientation and shape; instrument field-of-view size, shape and orientation; specifications for reference frames; and tabulations of time system conversion coefficients and more [33]. The kernels that were used for the bistatic geometry search model (as well as the bistatic measurement simulation model which will be discussed in chapter 4) are listed in appendix C. All the kernels can be downloaded from the ESA SPICE service File Transfer Protocol (FTP) server: `https://spiftp.esac.esa.int/data/SPICE/`.

3.2.2. Operating modes

The model has two main operating modes. The first mode (SPICE window) is only concerned with searching for viable bistatic measurement opportunities within a given time window, given certain constraints/requirements. This mode only returns a list of measurement opportunity intervals that were found within a given time frame. The second mode (fixed step mode) is used to determine the specular point planetocentric (latitude and longitude) coordinates for a (fixed step) list of times. This set of coordinates, together with their associated times can then be used as input for the bistatic measurement simulation model (which will be discussed in chapter 4).

3.3. Architecture

3.3.1. SPICE window mode architecture

In SPICE window mode the script uses a SPICE function to search for viable bistatic measurement opportunities within a given time window. The SPICE function performs a Geometry Finder search on a user defined boolean quantity. The SPICE Geometry Finder subsystem finds time windows (intervals) over which user-specified geometric conditions are met [34].

In SPICE window mode the geometry search model needs several input parameters, these can be separated into several categories:

- **Time parameters:** The user inputs a start and end time of the search window in either the Coordinated Universal Time (UTC), Barycentric Dynamical Time (TDB) or Ephemeris Time (ET) format; an aberration correction flag; time step size used in the SPICE function for finding geometric events; Geometry Finder convergence tolerance (sets the accuracy of the start and end times of found measurement intervals).
- **TX and RX parameters:** This includes two instances of the Spacecraft class (one for the TX and one for the RX), this is a custom class which houses information about the spacecraft itself (name, SPICE spacecraft (S/C) frame name) and several antenna parameters.
- **Planet parameters:** This includes the surface topography model (digital shape model) of the planet to be used (this will either be an ellipsoid or a digital shape model loaded by Digital Shape Kernel (DSK) files); an instance of the Planetary

body class which is a custom class that houses the planet's name, SPICE body-fixed frame name and ellipsoid radii.

- **Geometry parameters:** This includes the TX, RX positions, velocities and orientations w.r.t. the target body. These are indirectly set via the SPICE kernels, which are loaded via three metakernels (General,TX,RX); SP geometry tolerances.
- **Objective function & Optimization parameters:** These are parameters related to the bistatic geometry objective function and the optimization method used to find a minimum for this objective function.
- **Additional measurement opportunity constraints:** (=Optional) Additional constraints on the to be found measurement opportunities (max range sum, minimum measurement time, incidence angle bounds, max off-boresight angles).
- **Regions of interests:** (=Optional) A Regions of interests object (custom class) can be passed to check if the found measurement intervals intersect any of the regions of interests.

The model works as follows. The user search window start and end times are converted to the ET format and used to create a SPICE confinement window. Then the SPICE Geometry Finder function is called. This SPICE function uses a routine returning the boolean value corresponding to an ET. This bistatic geometry evaluation routine returns true if a valid measurement geometry could be found and false otherwise.

The bistatic geometry evaluation routine (function) works in the following way. First (for the given ET) the TX and RX positions are calculated. Then an initial guess for the SP is computed. This initial guess can then be used as starting point for the optimization algorithm. The optimization method tries to minimize an objective function which checks the bistatic measurement geometry requirements (incidence angle equal to emission angle and SP surface normal coplanar with TX-SP-RX plane), by varying the latitude and longitude of the SP. Once the optimizer is finished, the bistatic measurement geometry requirements of the found SP are checked and if the final optimization result is within the given tolerances, the geometry is considered valid. If any optional measurement opportunity constraints which relate to the geometry are supplied, these are also checked. The measurement opportunities search has the following optional constraints that can be added. A maximum range sum (TX to SP distance + RX to SP distance), a minimum measurement time, a minimum and maximum incidence angle and maximum off-boresight angles for the TX and RX antennas. Then if all the tolerances and constraints are satisfied, true is returned (plus relevant calculated data such as the found optimal SP coordinates and incidence angle).

Once the SPICE Geometry Finder function is finished, it returns a list of time intervals where the bistatic geometry requirements are satisfied. These time intervals (start and end times) are then written to a JSON file. Finally if Regions of interests collection object is also passed as input, the time intervals are checked whether they intersect any of the regions of interests. If they do, the regions that were intersected are stored with the interval information in the JSON results file. An overview of the architecture can be found in figure 3.1

3.3.2. Fixed step mode architecture

This mode works in a very similar way to the SPICE window mode. The input parameters are the same as for the SPICE window search with the exception of the SPICE Geometry Finder specific parameters (Geometry Finder convergence tolerance) and the optional regions of interests object which are omitted in the fixed step mode. The main difference between the fixed step mode and the SPICE window mode is that the fixed step mode does not use the SPICE Geometry Finder function to call the bistatic geometry evaluation routine, but instead calls this routine directly for a set of ET times. This list of ET times is computed based of the start and end times and a time step size. The bistatic geometry evaluation routine then return the relevant data (SP latitude/longitude coordinates, incidence angle, etc.) for every ET time and this data is then written to a JSON file. An overview of the architecture can be found in figure 3.1.

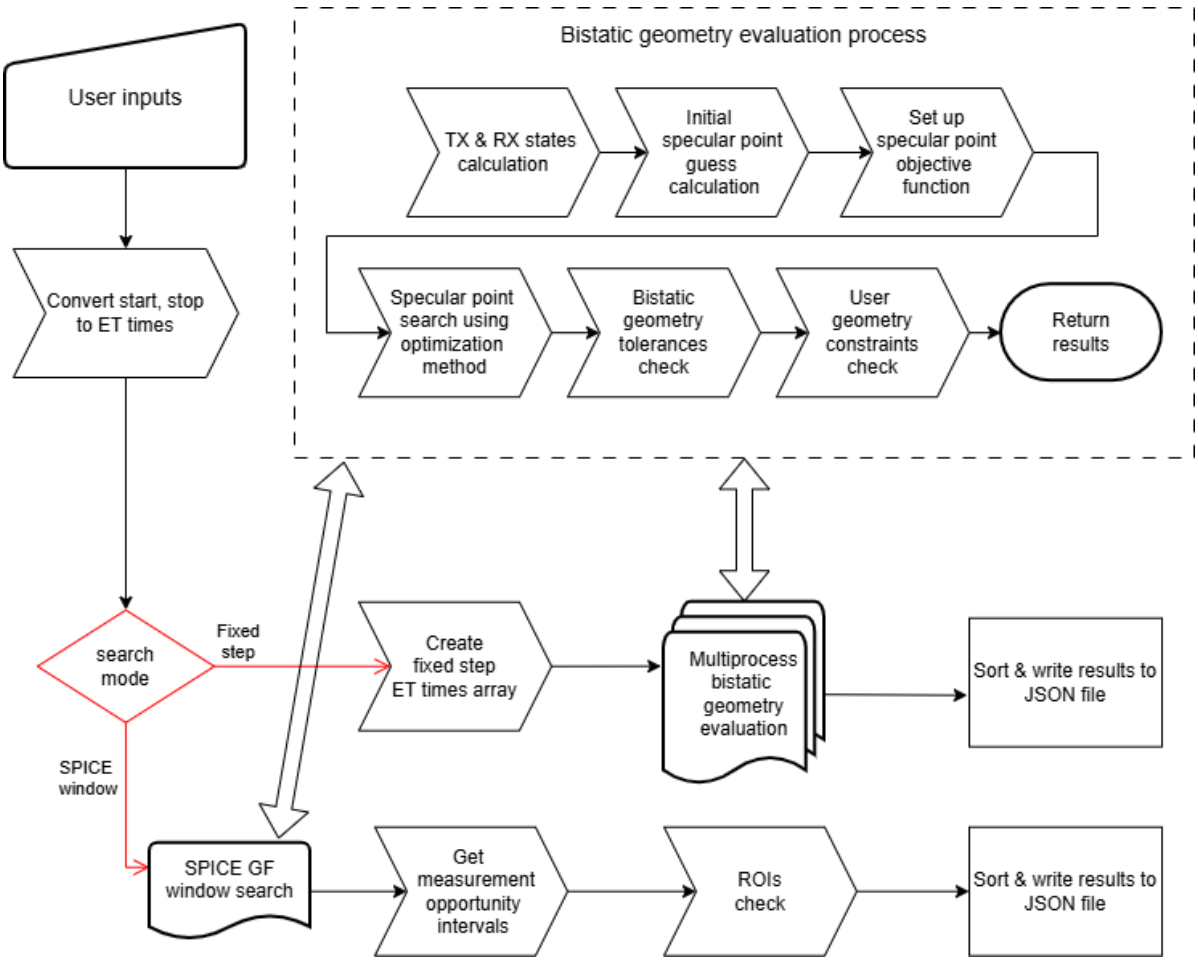

Figure 3.1: Diagram of the architecture of the bistatic geometry search script.

3.4. Specular point determination

In this section the process for finding the specular point location (coordinates) is explained.

3.4.1. Initial specular points estimation

To start the specular point determination, the optimization algorithm needs an initial guess for the specular point. A fast and accurate initial is important as it greatly influences whether and how fast the optimization algorithm converges.

Initial estimations are commonly based on the subpoint of the receiver on the planet's surface or the weighted distance along the vector from the receiver to the transmitter and then scaled down to the planet's surface to get the initial specular point [39, 48, 51], as shown in figure 3.2. For this thesis the second method was used.

First an estimated point S' along $\overrightarrow{RT}$ should be found, then the subpoint S of S' can be used as the initial estimation of specular point. The precision of estimation obtained from this method depends on the position of S' [39]. As mentioned before, a way to determine S' is by a weighted distance approach [48]:

$$\overrightarrow{OS'} = \overrightarrow{OR} + \eta \overrightarrow{RT} \tag{3.1}$$

$$\eta = \frac{\left|\overrightarrow{RR''}\right|}{\left|\overrightarrow{RR''}\right| + \left|\overrightarrow{TT''}\right|} \tag{3.2}$$

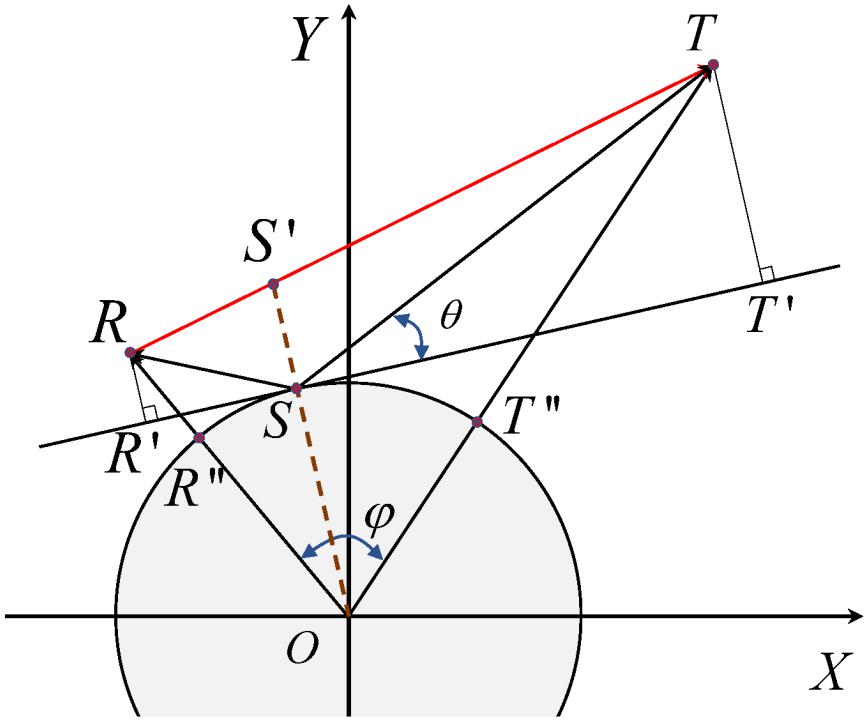

Figure 3.2: The geometry of initial specular points estimation. S is the specular point; R and T denote the receiver and transmitter; R' and T' are the orthographic points on the tangent plane to the sphere planet at S; S' is the intersection of vector $\overrightarrow{OS}$ and $\overrightarrow{RT}$. (Image source [39])

Then the initial specular point estimate is found by scaling S' so that it lies on the surface.

This approach should work better than the midpoint approach from Nieuwenhuizen [35], who reported a decrease in accuracy with increasing MEX altitude, as the weighted distance scaling takes into account the TX (and RX) altitude.

3.4.2. Optimization

With an initial specular point guess available, this can be used as the starting point for finding the actual SP. To achieve this an optimization algorithm was implemented. It works on the principle of minimizing an objective function which for a supplied lattitude/longitude point gives a measure of how close the selected point is to satisfying the bistatic measurement geometry requirements (incidence angle equal to emission angle and SP surface normal coplanar with the TX-SP-RX plane). Note that internally the longitude/latitude coordinates are first converted to 3D rectangular body-fixed frame coordinates (based on the selected digital shape model) and these can then be used to compute the required angles (with the help of SPICE functions). The optimization method then tries to minimize an objective function by varying the latitude and longitude of the input point.

The optimization methods were implemented by using the SciPy optimize sub-package which provides several methods for minimizing objective functions (see `https://docs.scipy.org/doc/scipy/reference/optimize.html#module-scipy.optimize`).

The optimization would ideally try to minimize the difference between the incidence and emission angles, with the coplanarity of the surface normal with the with TX-SP-RX plane as constraint. However most optimization methods do not support (non-linear) constraints. Therefore the coplanarity constraint is added to the objective function with a penalty function. The coplanarity constraint is mathematically implemented as the dot product between the SP normal vector and the cross product of the SP to TX and SP to RX. This should be 0 when coplanarity between the SP normal and TX-SP-RX plane is

satisfied. The objective function $f(\lambda_P, \varphi_P)$ is given in equation (3.3).

$$f(\lambda_P, \varphi_P) = |\theta_{inc,P}(\lambda_P, \varphi_P) - \theta_{em,P}(\lambda_P, \varphi_P)| + \text{penalty}(|\overrightarrow{n_P}(\lambda_P, \varphi_P) \cdot \frac{\overrightarrow{r_{P,\text{TX}}} \times \overrightarrow{r_{P,\text{RX}}}}{|\overrightarrow{r_{P,\text{TX}}} \times \overrightarrow{r_{P,\text{RX}}}|}|) \tag{3.3}$$

where λ_P, φ_P are the longitude and latitude of the point P under investigation, $\theta_{inc,P}$,$\theta_{em,P}$ are the incidence and emission angles of P, and $\overrightarrow{n_P}$,$\overrightarrow{r_{P,\text{TX}}}$,$\overrightarrow{r_{P,\text{RX}}}$ are the surface normal vector at P and the vectors pointing from P to the TX and RX respectively. For the penalty function two options are available, a linear and a quadratic penalty function:

$$\text{penalty}(x) = p \cdot \max(0, x) \tag{3.4a}$$

$$\text{penalty}(x) = p \cdot \max(0, x)^2 \tag{3.4b}$$

where p is a scaling constant. For this thesis equation (3.4a) was used.

3.4.3. Digital shape model

For the calculation of (among other things) incidence/emission angles a digital shape model of the target body (for this thesis Mars) is required. SPICE essentially allows for two types of shape models. The first option is where the target body is represented by an ellipsoid. For the purpose of trying to find measurement geometries, this is a good option as it means that there is only one specular point and because an ellipsoid has a smooth surface the optimizer should in principle not get stuck in any local minima. The model can also use DSK files, this will be discussed in more depth in section 4.2.7.

4

Measurement Simulation

The goal of the numerical bistatic measurement simulation model is the simulate the total received power for a bistatic measurement. Although the model can be used for any two spacecraft at any target body (as long as the relevant data is available in SPICE kernels), in this thesis the bistatic measurements between MEX and TGO, with Mars as target body will be the main focus. As several bistatic measurements between MEX and TGO have been performed during 2025, this enables a direct comparison between modeled and measured power. This allows for validation of the model and allows for comparing measurements with different operational parameters (e.g. pointing) and surface parameters (e.g. permittivity).

The numerical model/simulator to simulate bistatic measurements between two spacecraft was (just as the bistatic geometry search script) written in Python and uses the SPICE toolkit for most geometry related computations. First the model architecture is explained in section 4.1, then in section 4.2 several sub-elements of the model are explained in more depth. Lastly, in section 4.3 the data readout process for the MEX-TGO measurements is presented (which will be used to compare against the measurement simulation model).

4.1. Model Architecture overview

The model needs several input parameters. Inputs to the model can be separated into the following categories:

- **Time parameters:** This includes a list of measurement times (in ET format); and the aberration correction flag.
- **TX and RX parameters:** This includes two instances of the Spacecraft class (one for the TX and one for the RX), which houses information about the spacecraft itself (name, S/C frame name) and the antenna parameters (antenna signal power and frequency, noise temperature, as well as co-polarization (and if available cross-polarization) patterns of the antenna).
- **Planet parameters:** This includes the surface permittivity model, the surface topography model (digital shape model) of the planet and an instance of the Planetary body class which houses the planet's name, SPICE body-fixed frame name and ellipsoid radii.
- **Grid parameters:** This includes the grid cell size, total grid size and the specular point longitude/latitude coordinates (for every measurement time).
- **Operational parameters:** This includes the pointing modes to be assessed.
- **Geometry parameters:** This includes TX, RX positions, velocities and orientations w.r.t. the target body. These are provided via the SPICE kernels, which are loaded via three metakernels (General, TX, RX).

Some important things to note: the model also has a scattering model parameter, however currently only the Hagfors' model is implemented; and the aberration correction flag is set to 'None' as the aberration correction is assumed to have a negligible effect on the TX and RX positions compared to the time step used in the simulations which is 1 second.

The simulator is set up as follows. After all the above inputs are given, the simulator first calculates the TX and RX states and boresight vectors (for every selected pointing mode) in the planet (also called target body) body-fixed body-centered reference frame for the entire measurement time list (sequentially). Then for multiple ET times in parallel (multiprocessing) the following process is performed:

First a simulation grid is generated (with the grid spacing and total number of grid cells/points based off user input) with the specular point at the center of the grid. Then for all the grid points the required parameters (like incidence and emission angles, distances to the S/Cs, bistatic radar cross-sections, surface areas, gain values etc.) are calculated. With all the required grid cell parameters the reflected power for every grid cell can then be determined using equation (2.23). After that, the direct power is also calculated and the results (calculated grid cell parameters and power values) are returned.

The results for all the ET times, along with additional data like the input parameters and TX and RX states and boresight vectors, are then saved to a HDF5 file (HDF5 was chosen because it lets you store and compress large amounts of numerical data with fast I/O processing). An overview of the architecture can be found in figure 4.1

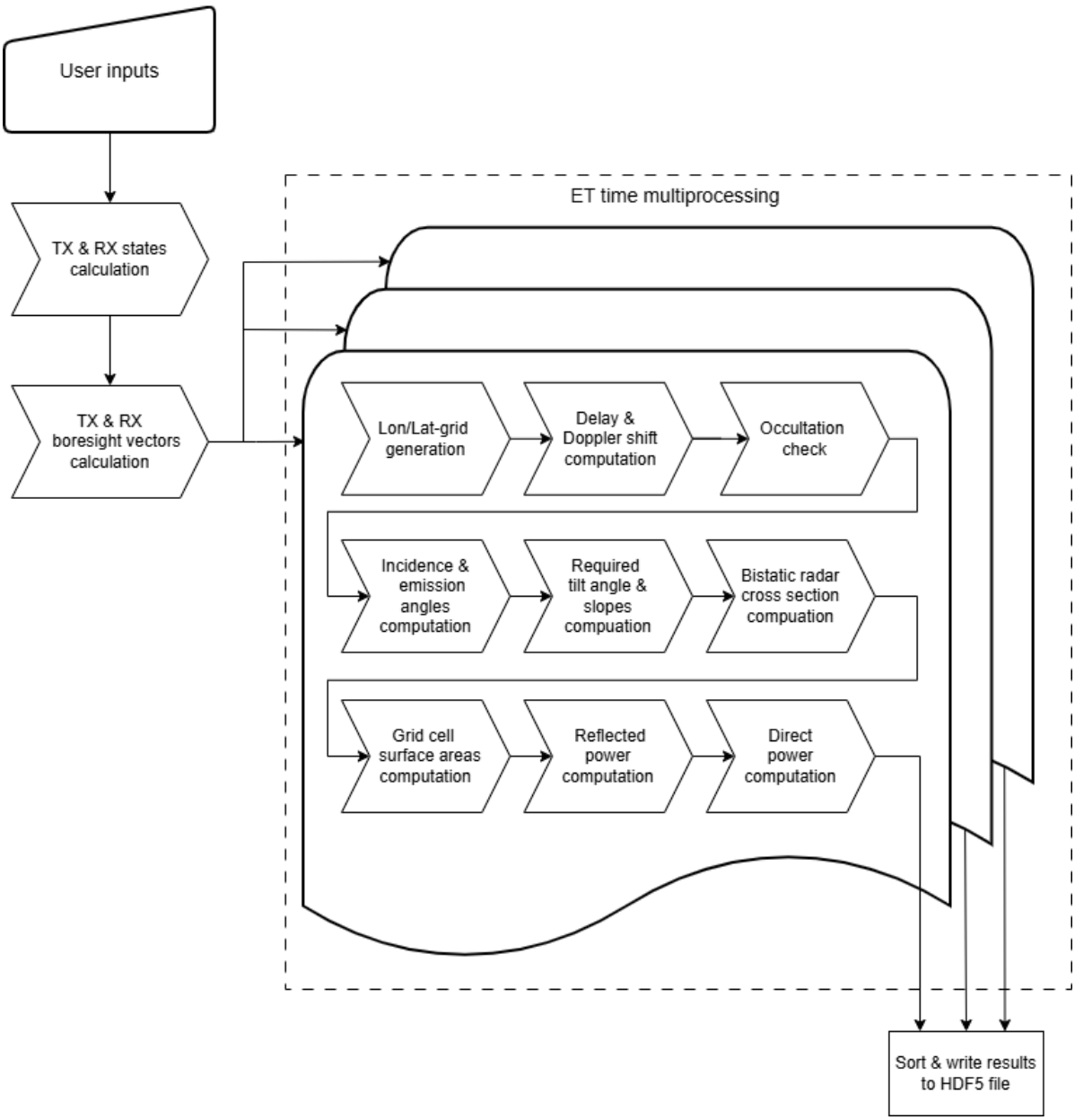

Figure 4.1: Diagram of the architecture of the bistatic measurment simulation model/script.

4.2. Model details

In section 4.1 a general overview of the architecture of the simulator was given. In this section several elements of the simulator will be discussed in more detail. This includes the modeling of the TX and RX antenna patterns, the latitude/longitude grid generation procedure, the used surface permittivity model, the bistatic radar cross section calculation, the available pointing modes of the simulator, the digital shape model used in the simulator and the modeling/calculation of the total received power.

4.2.1. Antenna patterns

In section 2.4 the modeling of bistatic signal power was discussed and the dependence on the TX and RX gain could be seen. Thus the gain patterns of the TX and RX antennas need to be modeled.

The antenna gain decreases the further away from the boresight the signal is transmitted/received. This is characterized by the radiation pattern of the antenna. The antenna patterns are modeled more extensively compared to the model of Nieuwenhuizen [35]. There only the co-polarization (the desired polarization of the antenna) was modeled. For MEX and TGO the co-polarization is Right Hand Circular Polarized (RHCP) [41]. For the model of this thesis, the cross-polarization will be taken into consideration as well. Unfortunately the there was no cross-polarization data available for MEX, so only the cross-polarization of TGO will be considered (though the simulator is written in such a way that the MEX cross-polarization could be added if the data were to be present).

The antenna pattern is simulated by a (user-defined) function which takes one input, the off-boresight angle. Generally speaking, the radiation pattern is dependent on both azimuth and elevation angle, however for simplicity, it is assumed that there is spherical symmetry in the radiation pattern and that the influence of the azimuth angle is negligible (so the pattern represents an average of all azimuths).

4.2.2. Co- and cross-polarization patterns for MEX & TGO

The MelaCom antenna system of MEX has off-boresight gain for the co-polarization as tabulated in table 4.1.

Table 4.1: MEX MelaCom co-polarization (RHCP) antenna gain pattern values (forward link; $437.1\,\mathrm{MHz}$), retrieved from [42, 35].

Off-boresight angle [°]	Antenna gain [dB]
0	6.0
10	5.5
35	3.0
50	−2.0
65	−10.0

The linear scale gain function was then generated by performing a fit, using a Gaussian radiation pattern (given in equation (4.1)), a good approximation for the shape of the MEX antenna pattern [41]. The radiation pattern fit can be seen in figure 4.2.

$$G(\theta) = 10^{\frac{G_{0,\mathrm{dB}}}{10}} \exp(-\ln(2) \cdot \left(\frac{\theta}{\theta_{3\mathrm{dB}}}\right)^2) \tag{4.1}$$

For the Electra radios of TGO, its off-boresight gain for the co-polarization is tabulated in table 4.2. Here the linear scale gain is once again generated by performing a fit, using a Gaussian radiation pattern as can be seen in figure 4.3. Important to note here is that this antenna pattern is slightly different compared to that of Nieuwenhuizen [35].

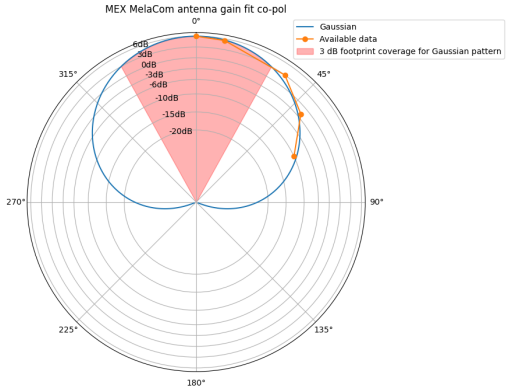

Figure 4.2: Polar plot MEX MelaCom modeled co-polarization (RHCP) antenna gain pattern.

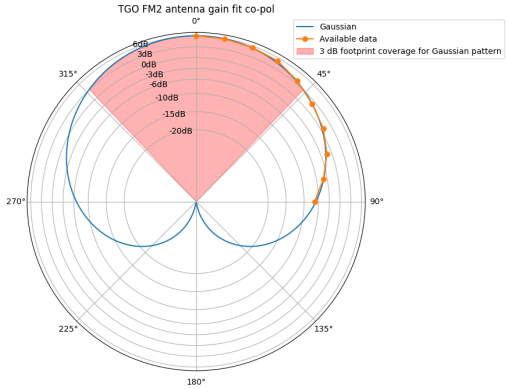

Figure 4.3: Polar plot TGO FM2 modeled co-polarization (RHCP) antenna gain pattern.

Table 4.2: TGO FM2 co-polarization (RHCP) antenna gain pattern values (return link; $437.1\,\mathrm{MHz}$), retrieved from [42].

Off-boresight angle [°]	Antenna gain [dB]
0	6.1
10	5.9
20	5.6
30	5.2
40	3.8
50	2.1
60	0.8
70	−1.3
80	−4.1
90	−7.1

The cross-polarization pattern for TGO was estimated from data from figure 4.4. Although the cross-polarization is more heavily dependent on both azimuth and elevation angle than the co-polarization, a rough average for multiple azimuth angles is taken and only a general off-boresight angle (so assuming spherical symmetry) is used. Additionally, in figure 4.4 the null of the cross-polarization patterns is not exactly at $0\,°$, but for the simulated pattern a symmetric pattern with a null at $0\,°$ is used. This was all done to keep the simulation simple and due to the poor quality of the available cross-polarization data for TGO. For the cross-polarization fit, a ratio of polynomials type function of the form as given in equation (4.2) was used for the linear scale gain (where $\theta \geq 0$ is the off-boresight angle and a, b, c, d are the fitting parameters). This radiation pattern fit can be seen in figure 4.5. Note that this radiation pattern only extends to about 150°, beyond this angle, the cross-polarization gain was set to 0 (=$-\infty$ dB).

$$G(\theta) = \frac{a\theta + b\theta^2}{1 + c\theta + d\theta^2} \tag{4.2}$$

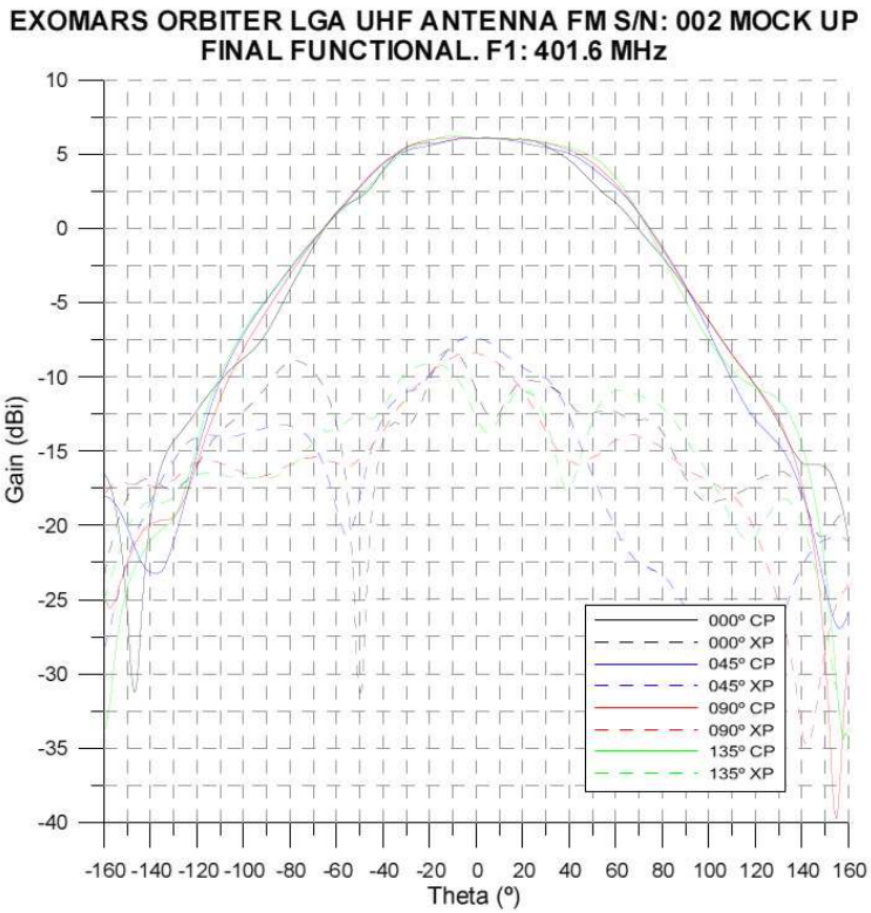

Figure 4.4: UHF antenna copolar and crosspolar patterns on TGO Mock up. F1 = $401.6\,\mathrm{MHz}$ (Image source [43])

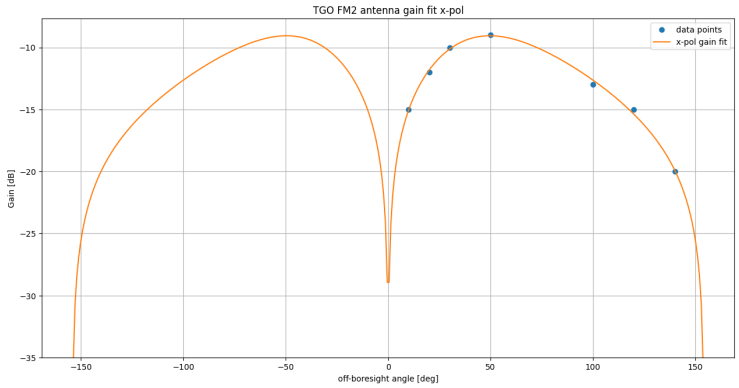

Figure 4.5: TGO FM2 modeled cross-polarization (LHCP) antenna gain pattern.

4.2.3. Simulation grid generation

The simulation grid consists of a 2D longitude/latitude coordinate grid with grid cells (where the grid cell center is used evaluation point for distance and angle calculations) along meridians and parallels (lines of longitude and latitude). First the number of points along the lines of longitude and latitude n_{lat} and n_{lon} is determined, based off the user input. The user gives a grid cell/element size (in meters) and a total grid length (in meters). Then the number of points along the lines of longitude and latitude is calculated such that n_{lat} times the grid cell/element size is equal to (or exceeds) the total grid length (and the same for n_{lon} of course). Note that the grid generation is done in such a way that the specular point is always in the center of the grid (so n_{lat} and n_{lon} are always odd numbers). Next, the spacing of the grid is determined. This is done using the pyproj library, a Python interface to PROJ (cartographic projections and coordinate transformations library) [38]. Pyproj has a function which given a single initial point and azimuth, number of points (npts) and delimiter distance between two successive points, returns a list of longitude/latitude pairs describing npts equally spaced intermediate points along the geodesic between the initial and terminus point (essentially a function which solves direct geodesic problem). Note that this function uses an ellipsoid shape. Along the meridian of the specular point (azimuth of 0/180°), this function is called with the delimiter distance set to half the grid cell/elem size. The delimiter distance is set to half the grid cell/elem size so that both the center, and upper and lower boundaries coordinates can be determined for the grid cells along the meridian of the specular point. Then the same thing is done along the parallel of the specular point (azimuth of 90/-90°). Finally the center points and boundaries of the specular point meridian and parallel are combined into a grid using the numpy.meshgrid function (both a grid of grid cell center points and a grid of grid cell boundaries is created). The grid cell center points are then used in the simulator as evaluation point for the calculation of grid cell parameters (e.g. distance to TX and RX, incidence and emission angles, grid cell normal vectors, etc.) and the grid cell boundaries are used for the calculation of the surface area of each grid cell. The advantage of using this procedure with grid points with equal distance spacing is that this way every grid cell should roughly have the same surface area (as opposed to for example equal latitude/longitude separation, where you would get significant different grid cell sizes the closer the specular point is to the poles). That being said, even for the current grid generation process, the closer the SP is to the poles, the larger the distortion in the area will be for grid cells further away from the SP grid cell.

4.2.4. Surface permittivity model

Modeling the permittivity for the entire planet is a difficult task. The (apparent) permittivity is highly dependent on the specific location on the planet (as it changes with surface composition). On top of that, the apparent permittivity is influenced by the different near-surface layers, this effect is extremely sensitive to the ratio between the signal wavelength and the layers' thicknesses [17].

Unfortunately finding a global surface permittivity map of Mars, applicable to the MEX MelaCom antenna frequency was not successful. Castaldo et al. [5] does present a global permittivity mapping

of Mars, which was derived from Mars SHAllow RADar sounder (SHARAD) radargrams. However, SHARAD uses a different wavelength compared to MEX MelaCom and the uncertainty (standard deviation) of the global permittivity map was quite high (plus there was no publicly available dataset, only a figure/map of the results).

Nieuwenhuizen [35] used inferred permittivities based on Gamma-Ray Spectrometer (GRS) and Fine Resolution Epithermal Neutron Detector (FREND) datasets, however these only gave a rough estimate, lack polar coverage and use significant interpolation. Therefore, for the model in this work, a constant value (for the whole planet) for ϵ_r was used for this numerical model (as well as the practical consideration that it was quick and easy to implement). Unless there are large permittivity changes along the measurement track, this permittivity model should be sufficient to do qualitative comparisons with measurement data. as a deviating permittivity should roughly speaking only shift the reflectivity (and therefore the power) up or down with a constant value (see also figure 2.3 again).

4.2.5. Bistatic radar cross section calculation

For the calculation of the incidence and emission angles of every grid cell a SPICE function is used. The slope of the grid cell is calculated by taking the angle between the surface normal vector of the selected shape model (MOLA 128 pixel per degree) and the normal vector that would be at the same latitude/longitude coordinate of the grid cell for an triaxial ellipsoid shape model. For the C parameter of the Hagfors' model, for every grid cell a root-mean-square operation is performed on the selected grid cell plus all the grid cells surrounding the selected grid cell. So for a selected grid cell not near any edges the root-mean-square operation is done using 9 points. This is done because the C parameter should represent a statistical average of the surface variation of an area, which means you need multiple points. Ideally this would be done with a set of points inside the grid cell, but this would add a lot of extra computations. The required tilt angle (for specular reflection) is calculated as the angle between the surface normal and the bisector of the $\overrightarrow{r_T}$ and $\overrightarrow{r_R}$ vectors (which is the surface normal at the scattering point needed for a perfect specular reflection) [18] (see again figure 2.6). Then (as explained in section 2.5.2) the incidence angle is used as input angle for the reflectivity. With the required tilt angle and C-parameter known, the σ^0_{pq} can be calculated (for both rr and lr).

4.2.6. pointing modes

One of the goals of this thesis was to investigate how spacecraft pointing influence the received signal. Therefore the simulator has the option to model the measurement for different pointing modes. The pointing modes that were implemented are the following:

- **Nadir pointing:** *In this mode the TX and RX spacecraft point their antenna boresight towards the center of the target body (the center of the body-fixed body-centered target body frame).*
- **SP pointing:** *In this mode the TX and RX spacecraft point their antenna boresight towards the specular point throughout the entire measurement.*
- **SPICE kernel pointing:** *In this mode the simulator retrieves the orientation of the TX and RX spacecraft from SPICE Camera Kernel (CK) files.*

The simulator allows for total received power computation for multiple pointing modes per simulations. For most simulations, SPICE kernel pointing and SP pointing were used. SPICE kernel pointing for comparison of the model with the MEX-TGO measurement data and SP pointing to investigate whether this pointing mode could potentially increase the reflected power (and SNR) of a measurement.

4.2.7. Digital shape model

For the determination of surface roughness and incidence/emission angles a digital model of the shape of the target body (in this case Mars) is needed. The simulator has two main options to model the shape. It can be modeled as an triaxial ellipsoid or it can be modeled by SPICE DSK files. ESA has DSK files available for the MOLA 128 pixel per degree topography model on their FTP server. So for most of the simulations, the 128 pixel per degree MOLA topography model was used. Though the simulator is set up in such a way that any shape model represented by DSK files can be used.

One of the big limitations of the model of Nieuwenhuizen was the low spatial resolution (typically 4 pixel

per degree, maximum of 16 pixel per degree) which led to large oscillations in the simulated power [35]. So a big priority for this numerical model was to increase the spatial resolution. This was achieved by using the DSK files instead of using Mission Experiment Gridded Data Record (MEGRD) data files. This meant that dedicated SPICE functions could be used for conversion from (planetocentric) longitude/latitude coordinates to surface points (expressed in a body-fixed body-centered target body frame), the calculation of the surface normal vectors, and the calculation of the illumination angles (incidence and emission angles) associated with these surface points. This allowed for a significant increase in computational speed and therefore the resolution could be increased.

4.2.8. Total received power modeling

As stated earlier, the main goal of this simulator/numerical model is to model the received power. Section 2.4 showed that the received power consists of the direct power and the scattering/reflected power. For the direct power equation (2.30) is used. For the reflected power equation (2.23) is used (as explained earlier the Hagfors' model is an empirical model which means that there are no separate coherent in incoherent components for the reflected power), where discretization occurs due to this equation being evaluated for every individual grid cell. One of the recommendations of Nieuwenhuizen [35] was to include polarization effects in the model. Although the recommendation there was to only let RHCP signals contribute to the total received power, because both the co- and cross-polarization patterns are modeled, in this model both the RHCP and LHCP received signals are modeled. So this means that the final model result includes the RHCP and LHCP received direct power, and the RHCP and LHCP received reflected power (for every grid cell). The total received power is then calculated as the sum of these four elements. Though they are stored separately so an analysis can be done of the relative contribution of RHCP vs LHCP polarization as well as reflected vs direct power. See figure 4.6 for a diagram showing all the different received power components.

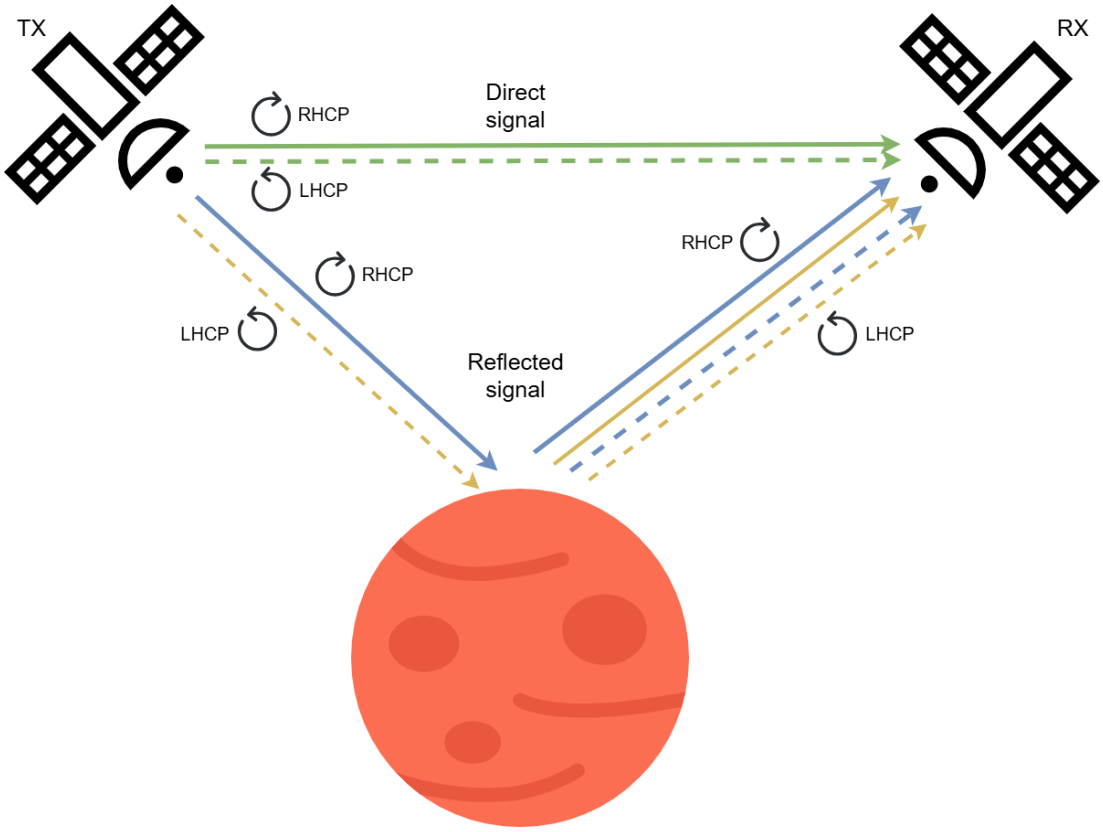

Figure 4.6: Polarization components of the bistatic measurement geometry signal power model where the TX emits both a RHCP and a LHCP component. RHCP and LHCP are depicted by solid and dashed arrows respectively. The green arrows represent the direct signal component, the blue and yellow arrows represent the signals originating from TX co- and cross-polarization respectively.

Both the direct and reflected power use the orientation of the TX and RX spacecraft to calculate the off-boresight angles to get the correct gain values. This is done for every pointing mode (as a list of pointing modes can be given as input). The distance are then a straightforward calculation based on the TX, RX and grid point positions. The bistatic scattering coefficients (rr and lr) are calculated as explained in section 4.2.5 and the surface area of an individual grid cell is approximated by the surface area of the grid cell on a biaxial ellipsoid, which is given by equation (4.3) [27]:

$$A_E = \frac{b^2}{2}(\lambda_2 - \lambda_1)\left[\left(\frac{\sin\varphi_2}{1-e^2\sin^2\varphi_2} + \frac{1}{2e}\ln\frac{1+e\sin\varphi_2}{1-e\sin\varphi_2}\right) - \left(\frac{\sin\varphi_1}{1-e^2\sin^2\varphi_1} + \frac{1}{2e}\ln\frac{1+e\sin\varphi_1}{1-e\sin\varphi_1}\right)\right] \tag{4.3}$$

where e is the eccentricity of the ellipsoid, a and b are the semi-major and semi-minor axes of the ellipsoid, φ_1, φ_2 are the bounding geodetic latitudes, and λ_1, λ_2 are the bounding longitudes (in radians). Then this area is also multiplied with a $1/\cos\theta_{slope}$ term to compensate for any occurring slopes.

Finally the measurement is also checked for occultation. This is once again done with a already existing SPICE function. If the planet blocks the line-of-sight between the TX and RX (occultation) the direct and reflected power are set to 0. Additionally, if the incidence angle of a grid cell goes above $90\,°$ the grid cell is also assumed to be occulted.

4.3. IQ file data readout

As mentioned earlier, several bistatic measurements have been performed between MEX and TGO during 2025. The results of these measurements are stored in IQ files. This section will discuss the data readout of these files and how the data is converted to power value in Watts.

Unfortunately, at the time of writing there was still no calibration data available for the MEX-TGO setup that was used in these measurements (though calibration measurements are planned to happen in March of 2026). Therefore, for the data readout the same procedure as described by Nieuwenhuizen [35] is used (for a detailed explanation refer to her thesis). The relevant data is collected as Automatic Gain Control (AGC) data, which is a parameter which is representative of the received signal power. This AGC data needs to be retrieved from In-phase / Quadrature (IQ) files (sample records which are downlinked by TGO). This consists of selecting the relevant bits from the IQ file to get the AGC data. The AGC data is a number ranging from 0 to 255. This is then converted to based on the noise floor power and a guess that every step in AGC count corresponds to a dB step size of 1 [35].

5

Results & Discussion

This chapter presents validation and model results for the bistatic geometry search numerical model as described in chapter 3 and presents validation and model results for the bistatic measurement simulation model as described in chapter 4 for several measurements between MEX and TGO, along with relevant discussion of these results. First the bistatic geometry search model results will be discussed in section 5.1 and after that the results for the measurement simulation model are discussed in section 5.2. Finally, section 5.3 will discuss an investigation into what would be an optimal incidence angle for a bistatic measurement (for a simplified geometry).

5.1. Bistatic geometry search results

First in section 5.1.1 several validation results will be presented, and then in section 5.1.2 the results for the future measurement opportunities search will be discussed.

5.1.1. BSR specular point ground track validation

To simulate the bistatic measurements, the (latitude/longitude) location of the specular point is required for all the time stamps where the measurement shall be simulated. This process was explained in chapter 3. There it was mentioned that for the SP search, either an ellipsoid shape model or a shape model defined by DSK files could be used. For all the results in this thesis, the ellipsoid shape model was used for finding the specular points.

The choice of using the ellipsoid shape model instead of the full Mars MOLA shape model has several reasons. First of all, due to the non-smooth terrain the optimization algorithm could potentially get stuck in a local minimum (or not converge at all). Additionally, with non-smooth terrain it is not guaranteed that there is a single SP, there could be multiple points that satisfy the geometry requirements of a SP, complicating the process. Finally, when SP searches were performed with the MOLA shape model, the resulting SP track for the measurement was usually very noisy and there were often gaps in the track where the optimization algorithm failed to converge, likely because at those periods any surface normal vector deviated too much from the TX-SP-RX plane (due to the non-smooth terrain).

It is important to confirm that the SP geometry search process (with the ellipsoid model) is working as expected. Therefore the bistatic geometry search process was validated by comparing it with the minimum delay point and with the SP tracks found by Nieuwenhuizen [35].

SP vs simulator minimum delay point

One possible way to validate the bistatic geometry (specular point) is to look at the delay of the specular point. For an ellipsoid shape model the specular point should be the point of minimum delay (=minimum path length) [39]. So the distance between the computed specular point and the point of minimum delay (for an ellipsoid shape model) should give a good measure of the accuracy of the bistatic geometry search process.

Thus, for measurement Bi-Static Radar (BSR)-2.1 a simulation was performed using an ellipsoid shape

model of Mars, with a $50\,\mathrm{m}$ by $50\,\mathrm{m}$ grid and grid cell size of $0.25\,\mathrm{m}$ (by $0.25\,\mathrm{m}$). Then the distance between the specular point and the minimum delay point was computed by solving the inverse geodesic problem (which was handled by PyProj [38]). The results for this can be found in figure 5.1. With an average distance of just above $0.5\,\mathrm{m}$, the bistatic geometry search algorithm seems to be converging to the point of minimum as expected. figure 5.2 is also included here to show an example the delay contours of the simulation (for $t = 0\,\mathrm{s}$). These delay contours are elliptical of shape for an ellipsoid shape model (as expected),

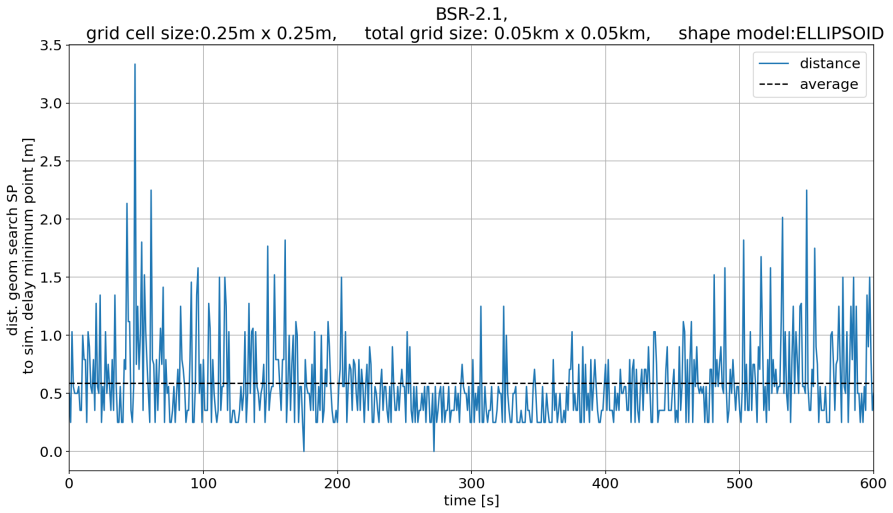

Figure 5.1: Distance between SP found by geometry search and minimum delay point of simulation (grid cell size: $0.25\,\mathrm{m}$, total grid size: $50\,\mathrm{m}$) for measurement BSR-2.1.

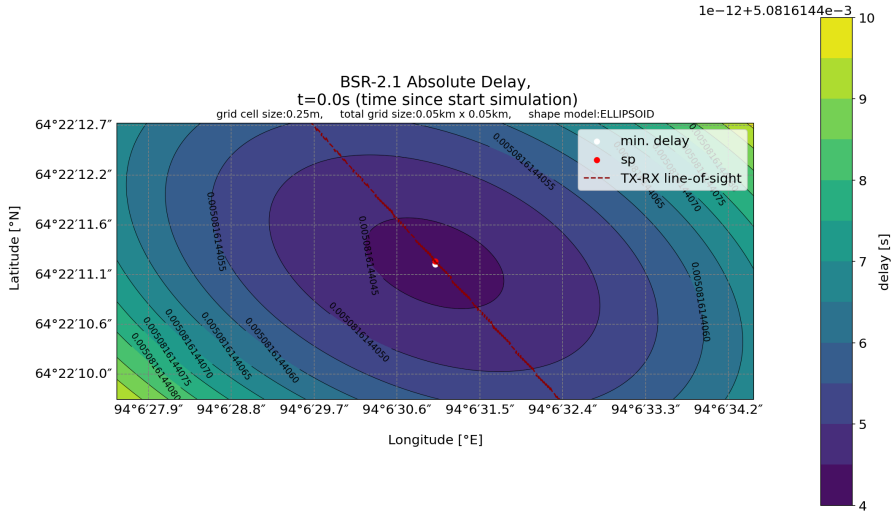

Figure 5.2: Absolute delay contour plot of the simulation surface grid (grid cell size: $0.25\,\mathrm{m}$, total grid size: $50\,\mathrm{m}$, shape model: ellipsoid) for measurement BSR-2.1 (at $t = 0\,\mathrm{s}$).

SP comparison with Nieuwenhuizen SP

Another way to validate the geometry search algorithm is by comparing it to the results of Nieuwenhuizen [35]. As Niewenhuizen also uses an ellipsoid shape model for determining the specular point, the ground tracks of the SP for this thesis and that of Nieuwenhuizen should be the same. In figure 5.3 the latitude and longitudes of the SP track for measurement BSR-2.1 is shown. Besides two anomalies in the latitude around $t = 125\,\mathrm{s}$ and $t = 550\,\mathrm{s}$, which appear to be deviations in the otherwise smooth curve, the track of the SP of the geometry search of this thesis and the track determined by Nieuwenhuizen [35] are in agreement.

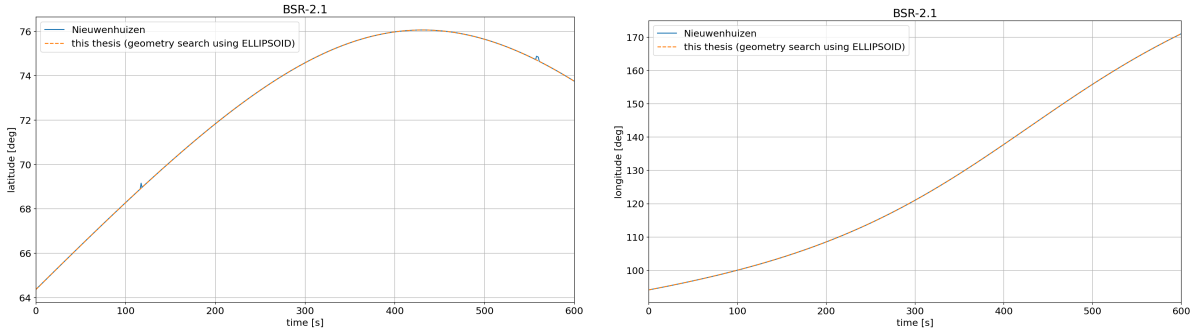

(a) Latitude **(b)** Longitude

Figure 5.3: Latitude and longitude for SP for this thesis and Nieuwenhuizen [35] for measurement BSR-2.1.

5.1.2. Measurement opportunities search results

One of the recommendations of Nieuwenhuizen [35] was to look for a less computationally intensive algorithm for deriving specular point geometry constraints. The current algorithm only takes a couple of seconds to run (for an ellipsoid shape model), and is decoupled from the measurement simulation script. This simplifies the simulation process because the specular point geometry search only has to be performed once for each measurement and can then be reused if it is desired to run the measurement simulation with a different set of parameters (e.g. changing the grid size, permittivity, etc.).

Besides using the bistatic geometry search model as part of the bistatic measurement simulation, it can also be used standalone to search for future bistatic measurement opportunities. One of the limitations in Nieuwenhuizen's [35] search possibilities was that it lacked the ability to search for measurements in specific target areas. Therefore in the measurement opportunities search model in this thesis, the possibility was added to check which Region of Interests (ROIs) are intersected for a measurement opportunity interval. This allows for a (automated) selection of potential measurement opportunities. This thesis uses the ROIs defined by Nieuwenhuizen [35] for its assessment. To aid the selection of the most useful measurement opportunities a figure-of-merit/performance metric was defined to rank all the measurement opportunities. This performance metric takes into account the amount of regions-of-interest that are intersected during the measurement interval, the duration of the interval, the minimum and maximum range sum (TX to SP distance + RX to SP distance) during the interval, and the minimum and maximum incidence angle during the interval. The performance metric is described by equation (5.1).

$$\begin{aligned}\text{metric} = {} & 1 \cdot 10^4 \cdot \#\text{ of intersected ROIs} + 10 \cdot \text{interval duration [s]} \\ & - 100 \cdot \left| 60^\circ - \frac{\theta_{i,min} + \theta_{i,max}}{2}\text{[deg]} \right| - (\text{range sum min [km]} + \text{range sum max [km]})\end{aligned} \tag{5.1}$$

A measurement opportunity search was then performed for June,July and August 2026 (with added constraints as discussed in section 3.1) and the found opportunities were then ranked with this performance metric. The results for the first seven measurements are shown in figure 5.4. Information about these measurement opportunities can be found in table 5.1.

The first ranked measurement opportunity has a very long measurement duration (over $1400\,\text{s}$) and low minimum range sum which is why it's at the top. The second ranked opportunity actually intersects both the Chryse Planitia and Valles Marineris regions which is why it also scored very high. The third measurement opportunity also has a very long measurement duration (almost $1200\,\text{s}$) and comes very close to the north pole. This potential measurement could also be interesting to investigate the effect that snow/ice has on the reflected power.

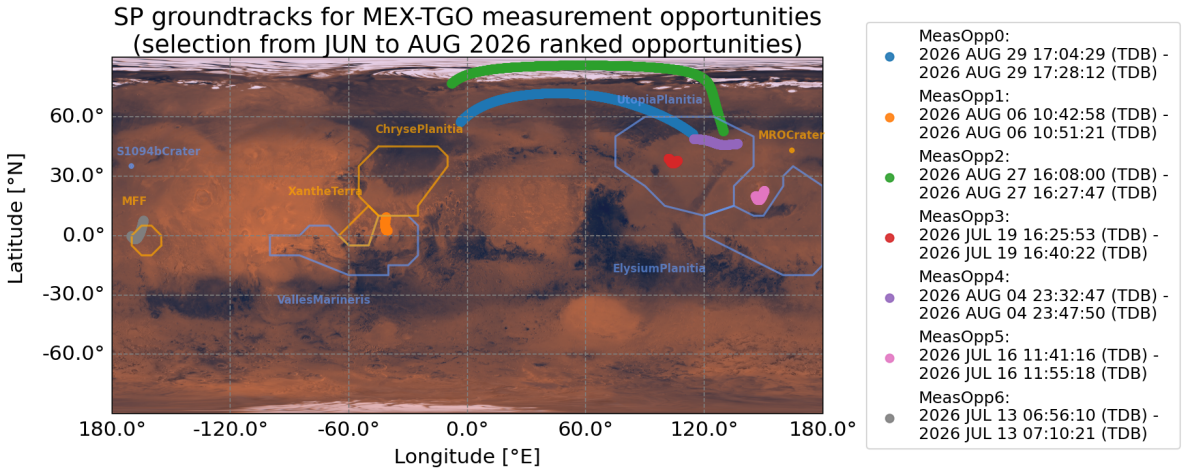

Figure 5.4: Global map of Mars with several future MEX-TGO bistatic measurement opportunities ground tracks with ROIs from [35] (background retrieved from [44]).

Table 5.1: Table with information about the first seven ranked measurement opportunities found between June and August 2026.

ID	Start time [TDB]	Measurement duration [s]	ROIs intersected	incidence angle bounds [°]		range sum bounds [km]	
				min	max	min	max
Meas. Opp. 0	2026 AUG 29 17:04:29.531	1423.125	'UtopiaPlanitia'	59.0	84.6	1474.9	3499.6
Meas. Opp. 1	2026 AUG 06 10:42:58.593	502.5	'ChrysePlanitia', 'Valles-Marineris'	73.1	84.8	3127.5	3499.15
Meas. Opp. 2	2026 AUG 27 16:08:00.468	1186.875	'UtopiaPlanitia'	54.9	85.0	1440.2	3156.2
Meas. Opp. 3	2026 JUL 19 16:25:53.906	868.125	'UtopiaPlanitia'	40.6	85.0	1071.3	3495.4
Meas. Opp. 4	2026 AUG 04 23:32:47.343	902.8125	'UtopiaPlanitia'	51.5	85.0	1291.8	3495.6
Meas. Opp. 5	2026 JUL 16 11:41:16.406	841.875	'ChrysePlanitia'	42.7	85.9	1248.4	3498.9
Meas. Opp. 6	2026 JUL 13 06:56:10.781	850.3125	'MFF'	43.5	85.0	1557.1	3499.6

5.2. Bistatic measurement simulation model results

As mentioned in the introduction, the MEX-TGO bistatic measurements were originally resulted from occultation measurements between the two spacecraft where, due to an incorrect switch-on time, it was discovered that there was also a power return from the surface. Following the same convention as Nieuwenhuizen [35] these measurements are designated as BSR campaign 1. However, due to the very low signal strength and little signal power variations, BSR-1.1 to 1.4 will not be discussed in this thesis. After BSR campaign 1 two more measurements were done in March and April of 2025 (BSR campaign 2) and Nieuwenhuizen proposed several new measurements (between July and December 2025) from which a selection was also chosen. table 5.2 summarizes all the bistatic measurements between MEX and TGO (except BSR campaign 1) for which at the time of writing measurement data was available. These measurements were all modeled with the bistatic measurement simulation model and will be discussed in sections 5.2.3 and 5.2.4. But first several validation results of the model will be presented.

Table 5.2: Table of measurement times and duration for BSR campaigns 2 to 8 retrieved from [35]

ID	UTC Date	UTC Time Start	Duration [min]
BSR-2.1	20/03/2025	23:40:54	10
BSR-2.2	05/04/2025	16:56:04	10
BSR-3.1	17/07/2025	10:38:31	10
BSR-4.1	15/08/2025	19:39:12	20
BSR-5.1	22/09/2025	22:56:40	10
BSR-6.1	30/09/2025	19:33:20	10
BSR-6.2	07/10/2025	05:02:15	8
BSR-6.3	13/10/2025	00:38:36	19
BSR-6.4	15/10/2025	15:30:52	10
BSR-6.5	16/10/2025	05:21:53	20
BSR-7.1	01/11/2025	12:33:54	10
BSR-7.2	04/11/2025	03:21:58	10
BSR-7.3	09/11/2025	09:10:58	10
BSR-7.4	15/11/2025	04:49:32	10

5.2.1. Grid cell size effect on model

A first validation step of the bistatic measurement simulation was to investigate the grid cell size effect on the model power. As the accuracy of the calculations within the model is driven by the accuracy of the DEM, the expectation is that grid cell sizes below the Mars MOLA DEM (which is about $463\,\mathrm{m}$ at the equator) will not lead to significant differences in model results. To validate this several simulations (for a $50\,\mathrm{km}$ by $50\,\mathrm{km}$ grid) with different grid cell sizes were performed for measurement BSR-2.1. The simulation with the smallest grid cell size ($200\,\mathrm{m}$ by $200\,\mathrm{m}$) was taken as the reference (assumed to have the highest accuracy). The difference in power between the other simulations and the reference simulation then gives a measure of the error for the higher grid cell sizes. Therefore the relative RMS error of the reflected power of the other grid cell sizes with respect to the reference power (RMS $\frac{P_{refl}-P_{refl,ref}}{P_{refl,ref}}$) can be seen in figure 5.5.

Figure 5.5 shows that the error decreases roughly linearly with grid cell size until around $400\,\mathrm{m}$. Below $400\,\mathrm{m}$ the RMS error seems to level off as expected, with the remaining error attributed to discretization noise. For most of the simulations however, a $800\,\mathrm{m}$ grid cell size was used to reduce the computation time.

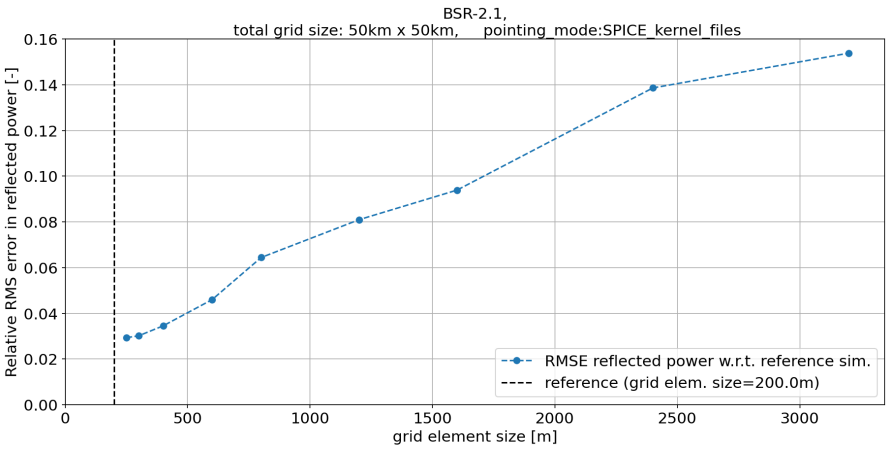

Figure 5.5: Relative RMS error of reflected power for simulations with different grid cell sizes with respect to reference simulation (grid cell size $200\,\mathrm{m}$) for measurement BSR-2.1.

5.2.2. Grid size effect on model

The effect of the total grid size was also investigated. Several grid sizes were tested, including $100\,\mathrm{km}$ by $100\,\mathrm{km}$, $200\,\mathrm{km}$ by $200\,\mathrm{km}$ and $300\,\mathrm{km}$ by $300\,\mathrm{km}$ grids. The one experimental simulation performed with a $300\,\mathrm{km}$ by $300\,\mathrm{km}$ grid did not yield a significant different result compared to the $200\,\mathrm{km}$ by $200\,\mathrm{km}$ grid simulation (in terms of received power). Therefore, to keep the computation times of a single measurement reasonable, it was decided (for most measurements) to use a $200\,\mathrm{km}$ by $200\,\mathrm{km}$ grid.

5.2.3. Model comparison BSR 2.x, 3.x, 4.x with measured data and Nieuwenhuizen model

One of the main research questions was to compare the modeled measurements (specifically the received power) with the initial model created by Nieuwenhuizen [35] and compare it with the measured data from MEX-TGO bistatic measurements. First the results for the received power (using the spacecraft pointing attitudes that were used during the MEX-TGO bistatic measurements) for BSR campaigns 2,3 and 4 (BSR-2.1 till 4.1) will be discussed as they offer the possibility compare the current model to the model of Nieuwenhuizen [35] and see if the improvements to the spatial resolution and switching to the DSK files of the Mars MOLA shape model improved the results. As mentioned earlier,BSR-1.x results will not be discussed as they had low signal strength and very little power variations across their measurements, making it difficult to use for comparison.

Although a spatial resolution increase could be achieved compared to Nieuwenhuizen [35], to limit the computation time the temporal resolution was kept at time steps of $1.0\,\mathrm{s}$. All simulations were done with a relative permittivity of $\epsilon_r = 4.0$, a grid size of $200\,\mathrm{km}$ by $200\,\mathrm{km}$ and a grid cell size of $800\,\mathrm{m}$ for the 10 minute measurements and $1600\,\mathrm{m}$ for the 20 minute measurements.

The noise temperature of the TGO RX antenna was retrieved from [41] to be $300\,\mathrm{K}$ and the noise bandwidth is deduced from the sampling rate ($32\,\mathrm{kHz}$). According to Svedhem [41] there should be an anti-aliasing filter before the Analog-to-Digital Converter (ADC) and therefore the noise bandwidth should be half the sampling rate, which gives a noise bandwidth of $16\,\mathrm{kHz}$. These numbers are different from the ones used by Nieuwenhuizen [35], so this means that the received power from the measured data will be different. Additionally, a mistake in the reflected power equation of Nieuwenhuizen was found, dividing by 4π squared instead of 4π cubed. So a correction factor of $1/4\pi$ has been applied to the Nieuwenhuizen reflected power.

BSR-2.1
In terms of features, in figure 5.6 it can clearly be seen that the model follows the measured data for the large dip around $t = 150\,\mathrm{s}$. This dip is caused by the Louth crater [3] which is present near the SP around that time. This can clearly be seen when looking at figure 5.7 which shows the terrain of the simulation grid at $t = 150\,\mathrm{s}$. At the end of the measurement (between $t = 500\,\mathrm{s}$ and $t = 600\,\mathrm{s}$) the model also appears to follow the data, with a dip and then two peaks visible in the model as well as in the measured data.

For this measurement the direct signal power is notably lower than the reflected power. So the behavior observed in the total received power is primarily driven by the behavior of the reflected power.

When comparing to the model of Nieuwenhuizen, what stands out is the overall power level is much higher for Nieuwenhuizen and the Nieuwenhuizen model has a large scale increase and then decrease which is not present in either this thesis' model or the data.

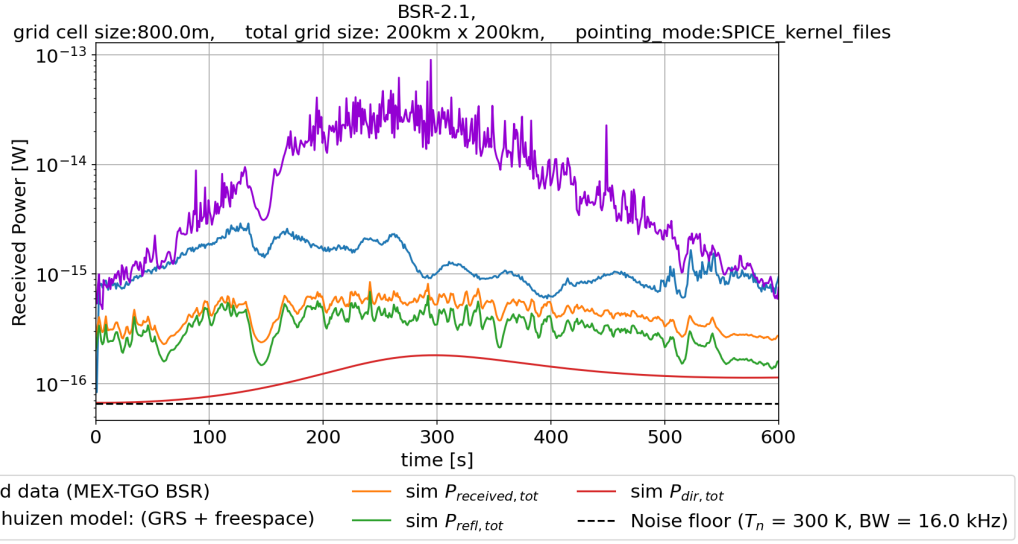

Figure 5.6: Comparison of received power model results with measured data and Nieuwenhuizen [35] model for BSR-2.1.

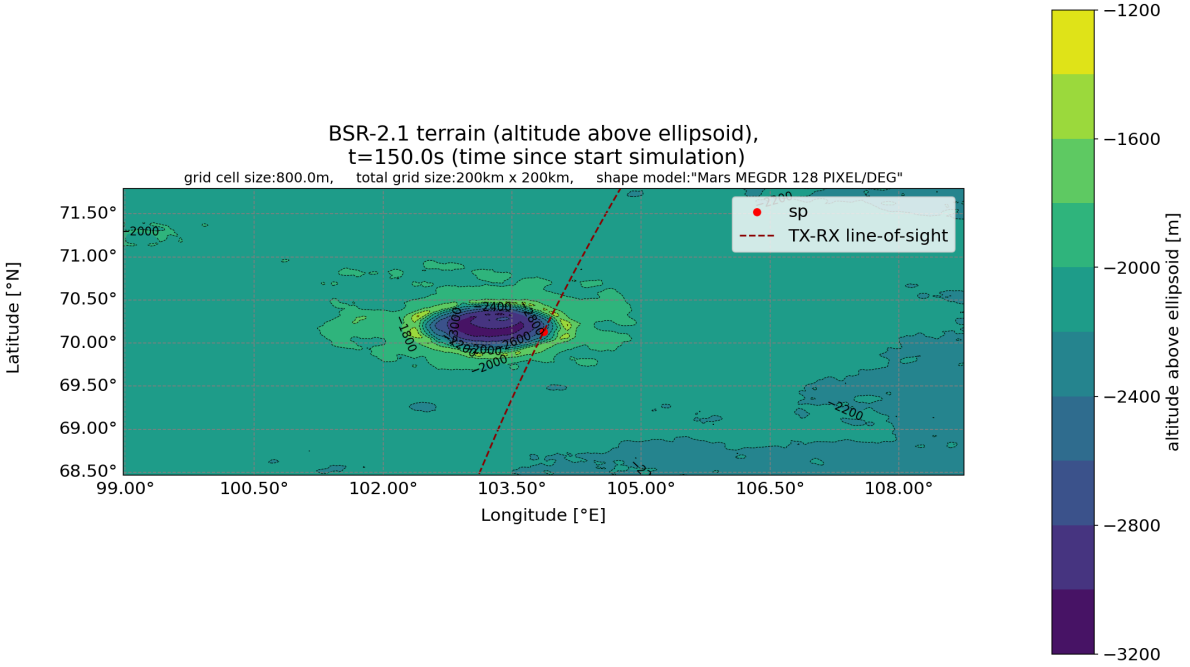

Figure 5.7: Terrain (altitude above ellipsoid) contour plot of the simulation surface grid for measurement BSR-2.1 (at $t = 150\,\mathrm{s}$)

BSR-2.2

In figure 5.8 the overall shape of the model seems to match of the data reasonably, but the model appear dampened relative to data, with the model features occurring at a much smaller power scale. For example the large scale increase and then decrease between $t = 300\,\mathrm{s}$ and $t = 600\,\mathrm{s}$ which can clearly be seen in the data is barely visible in the model (though it can clearly be seen the modeled direct power component). This is in striking contrast with the Nieuwenhuizen model where (when ignoring the ripple effect) the large scale increase and then decrease is much larger. The model does also appear to have similar fluctuations in power between $t = 350\,\mathrm{s}$ and $t = 450\,\mathrm{s}$, especially when comparing the measured data to the total reflected power. However these effects are overpowered by a large direct signal power, resulting in the total received power being very flat compared to the data.

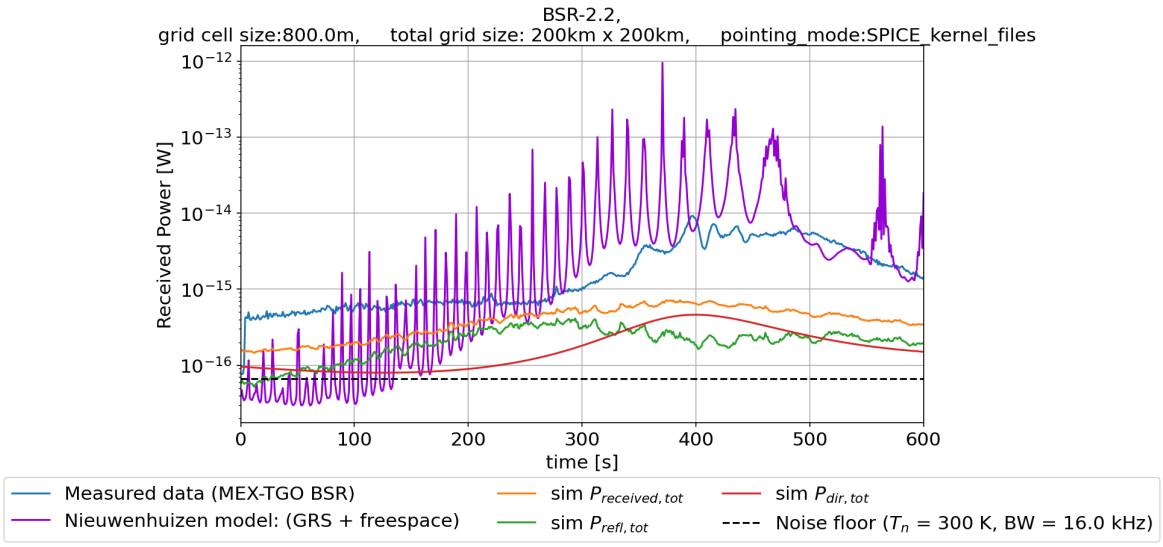

Figure 5.8: Comparison of received power model results with measured data and Nieuwenhuizen [35] model for BSR-2.2.

BSR-3.1

For this measurement (figure 5.9) the model follows most of the shape of the data extremely well. From $t = 0\,\mathrm{s}$ until $t = 425\,\mathrm{s}$, virtually every significant peak/dip in power can that can be seen in the data seems to be present in the model. Only the large spike at the end of the measurement is not visible in the model.

When comparing to Nieuwenhuizen, some similarities in the power fluctuations can definitely be observed, but once again the absolute power of the Nieuwenhuizen model is much larger and its overall ripple effect makes it difficult to see certain features.

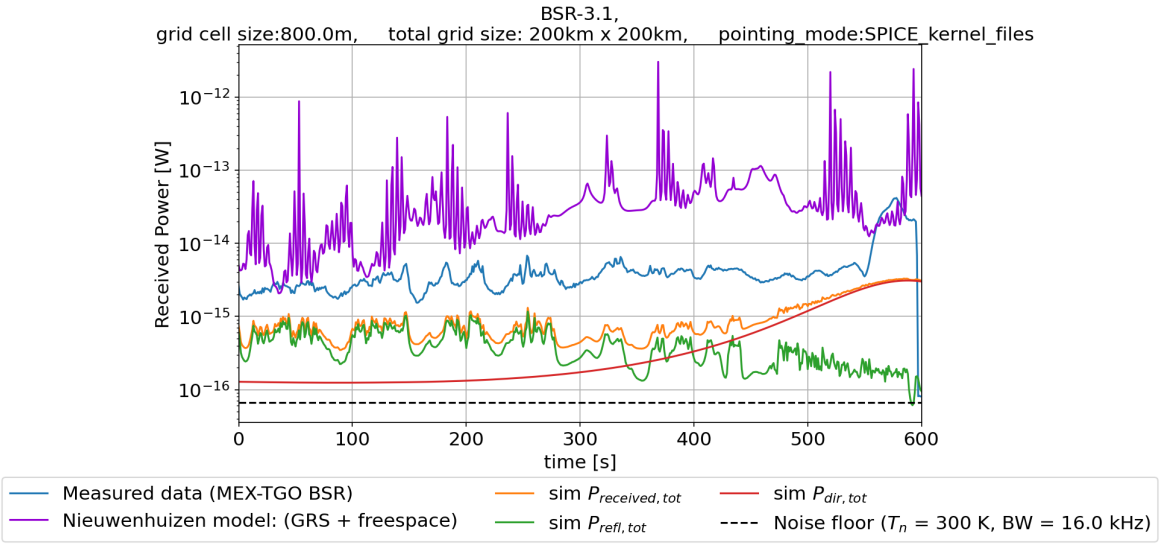

Figure 5.9: Comparison of received power model results with measured data and Nieuwenhuizen [35] model for BSR-3.1.

BSR-4.1

In figure 5.10 the overall (primarily flat) shape of the model matches the measured data quite well. What is remarkable though is that the large bump/peak between $t = 200\,\mathrm{s}$ and $t = 350\,\mathrm{s}$ does not appear in the model, whereas several smaller features (for example several spikes before $t = 200\,\mathrm{s}$ and between $t = 600\,\mathrm{s}$ and $t = 900\,\mathrm{s}$) do appear in the model. Additionally, at the end of the measurement the times when the power disappears for the model and drops to the noise floor for the measured data are the same. This is due to occultation and indicates that the occultation check of the simulator appears to be operating adequately.

Near the middle of the measurement, Nieuwenhuizen's model power unexpectedly decreases significantly. Also near the end of the measurement, Nieuwenhuizen's model levels off due to its direct power contribution, however compared to this model the direct power contribution of Nieuwenhuizen's model is a bit lower, which is surprising as the only source for this discrepancy could be either a difference modeled distance (unlikely given that this model and Nieuwenhuizen's model both use the same SPICE kernels), or a difference in the antenna gain patterns or off-boresight angles. It is likely (in part) caused by the difference in the receiver (TGO) co-polarization antenna gain pattern.

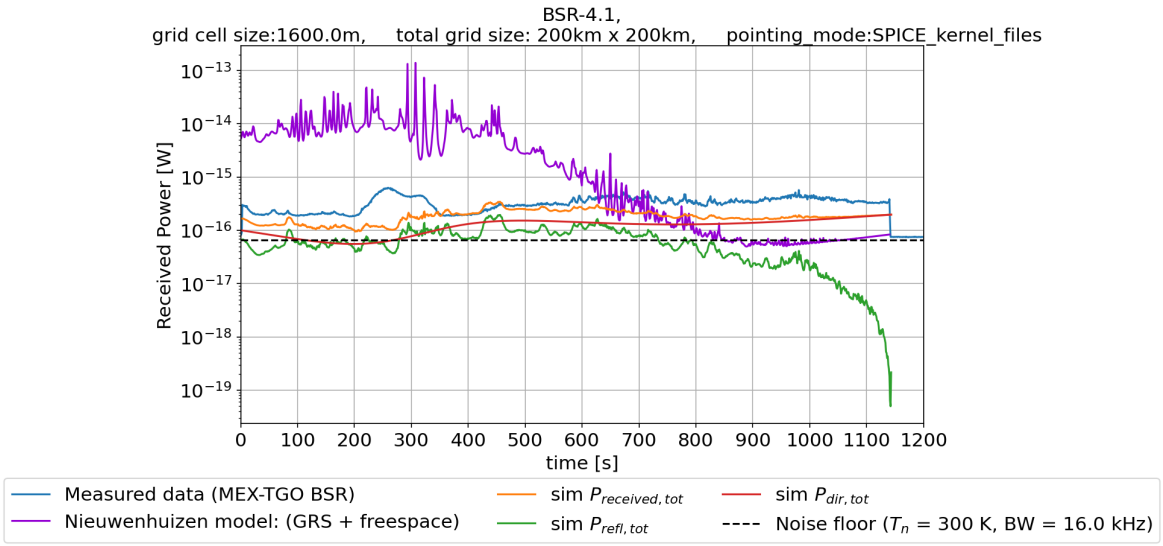

(a) Overview

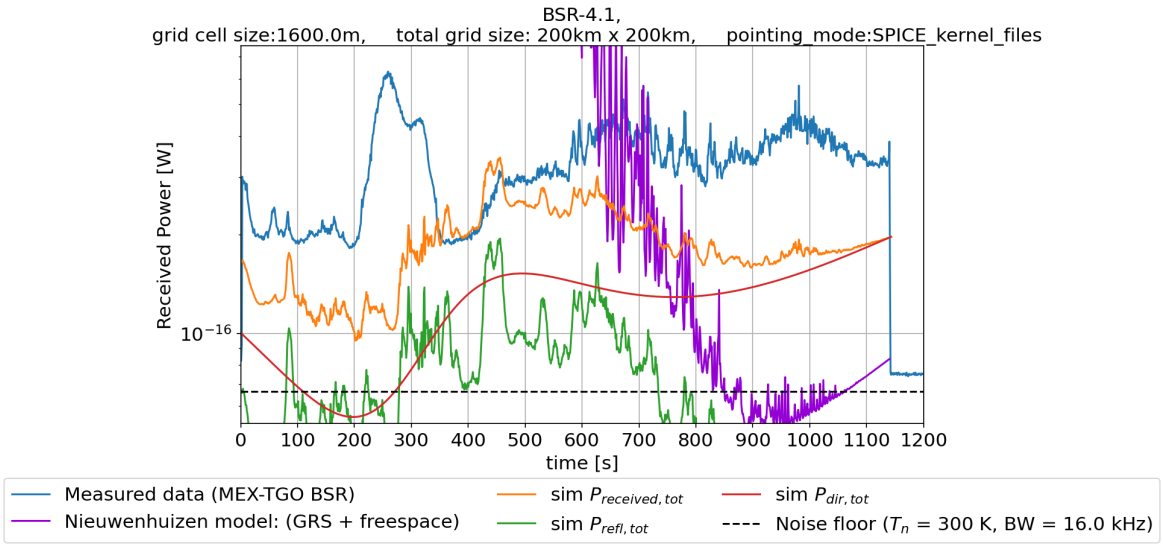

(b) Zoomed in

Figure 5.10: Comparison of received power model results with measured data and Nieuwenhuizen [35] model for BSR-4.1.

General observations

The first thing that stands out is that compared to the data and to Nieuwhuizen's model the absolute power seems to be consistently lower. Whether this is an underestimation of the power of the model is difficult to say as there is no calibration data available yet to determine the actual absolute measured power. Therefore it is more interesting to look at the general shape of the power curves and see if features like peaks and valleys that occur in the measured data, also appear in the model.

Compared to Nieuwenhuizen's model, the current model does not seems to suffer from periodic oscillations/ripple effects. Moreover, the current model also does not seem to have any kind of 'signal mirroring effect' that Nieuwenhuizen mentioned in her model (when using 4 pixel/deg resolution), and the current model also doesn't suffer from the very large difference between the minimum and maximum absolute power that can be seen in the model of Nieuwenhuizen. These are all very good signs, suggesting that the increase in spatial resolution seems to have really improved the model results.

Generally speaking, the model shape matches the measured data very closely. The features in the power signal are usually less severe for the model than for the measured data, but again, this can be attributed to the uncertainty in the MEX-TGO power calibration. However the current model doesn't match the data in every place. When trying to find similarities between the regions that were modeled less accurately (particularly looking at the large scale increase and then decrease between $t = 300\,\mathrm{s}$ and $t = 600\,\mathrm{s}$ for BSR-2.2, the end of BSR-3.1 and the large bump/peak between $t = 200\,\mathrm{s}$ and $t = 350\,\mathrm{s}$ in BSR-4.1) it was noticed that all these deficiencies seems to happen when the incidence angle is on the lower side (see the incidence angle plots in appendix B). So it could be that reflected power at low incidence angles is underestimated by the model. Perhaps this is because the cross-polarization of MEX is not included, but this is not certain.

5.2.4. Model comparison BSR 5.x, 6.x, 7.x with measured data

More recent measurements (BSR campaigns 5,6 and 7) were also available. The results for the received power (again using the spacecraft pointing attitudes that were used during the MEX-TGO bistatic measurements) for these measurements are discussed below. Although these measurements were not modeled by Nieuwenhuizen, a comparison with the measured data is still possible.

BSR-5.1

Again the model matches the general shape of the measured data really well. Especially the peak around $t = 380\,\mathrm{s}$. This peak corresponds to when the SP is in the middle of a crater. Only the peak around $t = 500\,\mathrm{s}$ is not very pronounced (a bit more flattened compared to the measured data). Once again the measured data has a higher power than the model. At the very beginning of the measurement, it can once again be observed that the time when the spacecraft come out of occultation for the model matches that of the data. However, there is a small difference between the signal power of the measured signal during eclipse and the noise floor power. This is because the 'calibration' of the noise floor power is determined once and the same conversion factor is used for all the measurements. So this seems to indicate that there is some drifting of the noise floor AGC value.

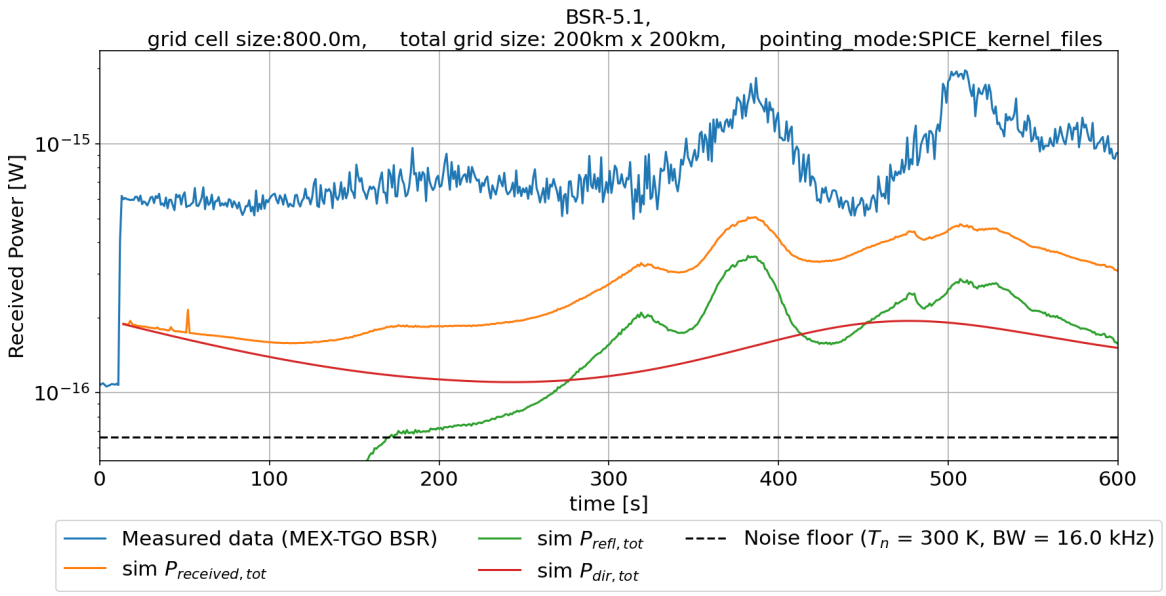

Figure 5.11: Comparison of received power model results with measured data for BSR-5.1, zoomed in.

BSR-6.1

The model follows the general shape of the measured data reasonably. However, where the data has its maximum power around $t = 350\,\mathrm{s}$, the model only starts to drop in power just after $t = 400\,\mathrm{s}$. Secondly, the large spikes in power for the data at $t = 500\,\mathrm{s}$ and just before $t = 600\,\mathrm{s}$ are very dampened in the model due to the large direct power. These spikes can clearly be seen though in the reflected power.

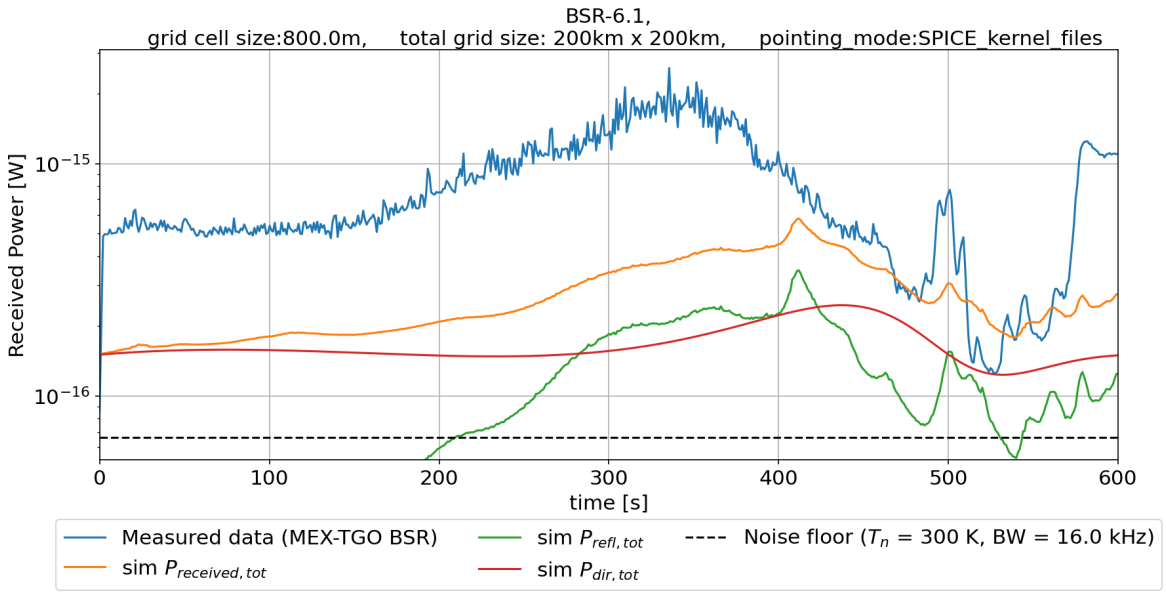

Figure 5.12: Comparison of received power model results with measured data for BSR-6.1, zoomed in.

BSR-6.2

The general shapes of the measured data and the model match once again very well. The only surprising thing in the model shape is the big dip around $t = 380\,\mathrm{s}$ in the model power which does not occur in the data. When looking at the terrain this dip appears to occur when the SP is on the edge/rim of a crater. Also, the moment of coming out of occultation can once again clearly be seen to match.

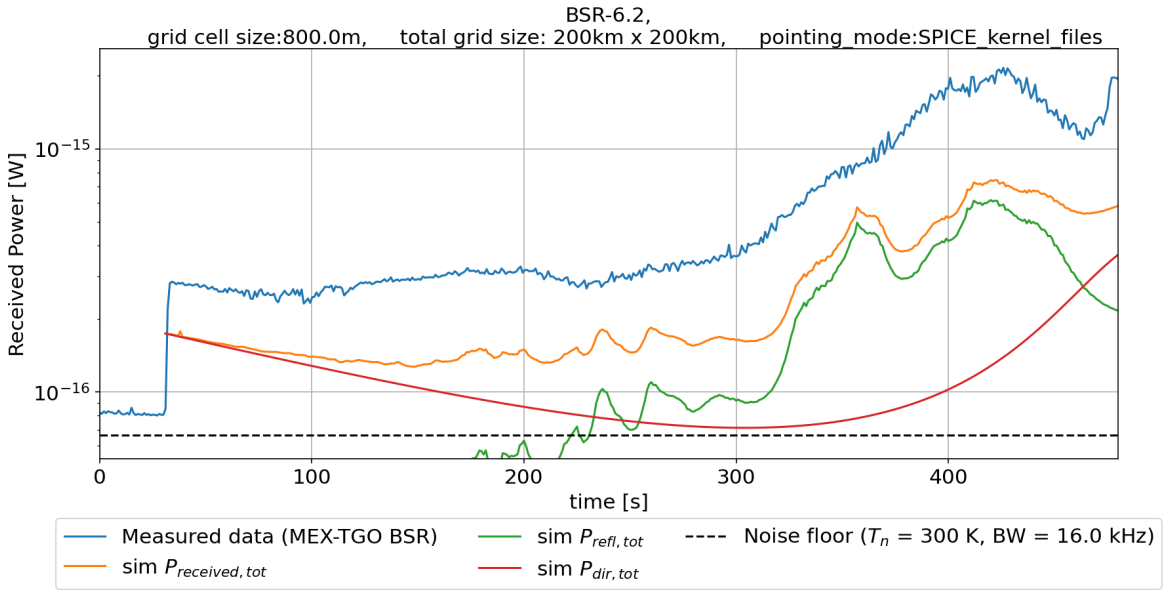

Figure 5.13: Comparison of received power model results with measured data for BSR-6.2, zoomed in.

BSR-6.3

Once again the general shapes seem to be a quite good match. Surprising is the relative ratio of certain dips in the model compared to the data. In the model there is a large dip around $t = 500\,\mathrm{s}$ and then some smaller peaks/dips after that. In the data, the dip around $t = 500\,\mathrm{s}$ is also present but much smaller and the peaks/dips right after are much more erratic compared to the model. Occultation can again be observed at the beginning and end for the data and model.

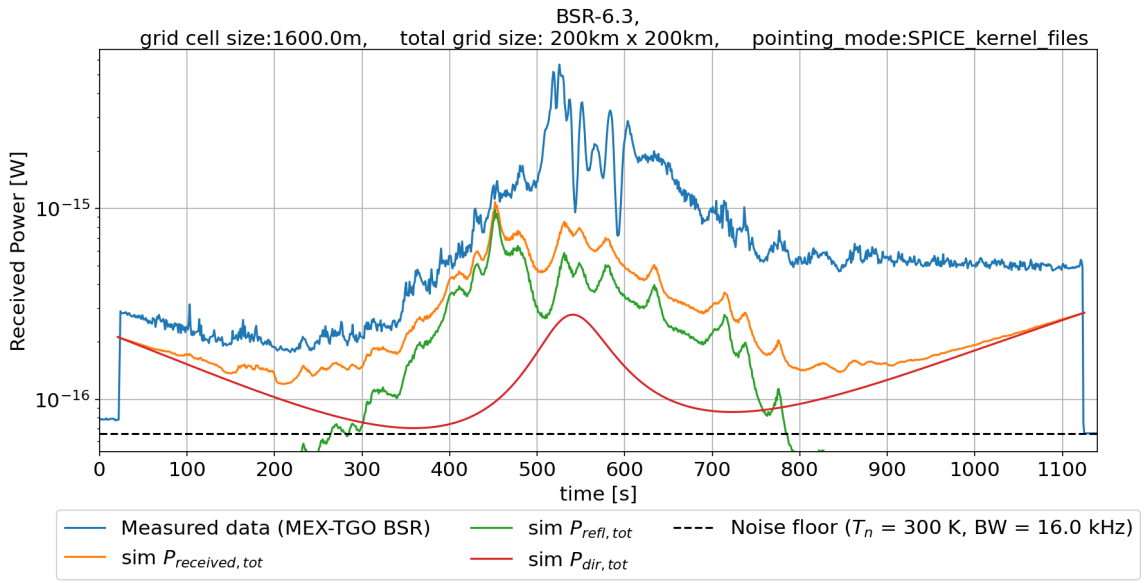

Figure 5.14: Comparison of received power model results with measured data for BSR-6.3, zoomed in.

BSR-6.4

The first two-thirds of the measurement, the reflected and direct power are well below the noise power. This is likely due to a very large TX antenna off-boresight angle in the beginning of the measurement (see figure B.9 in appendix B). Only in the last third of the measurement does the power start to rise. The point when the power starts to rise happens roughly at the same time for the measured data and the model. The model initially rises faster than the data, which is surprising as for all the previous measurement the measured data power has consistently been higher than the model power. However, then the model has a dip in power ($t = 500\,\mathrm{s}$) which cannot really be observed in the data. After that the model follows the shape of the data quite well for the last $100\,\mathrm{s}$ of the measurement. When looking at the terrain around $t = 500\,\mathrm{s}$ the specular point comes really close to a crater which could be the cause of the dip. This dip is on the smaller side in terms of absolute power (the zoom makes it seem more pronounced), which could be why it does not show up in the data.

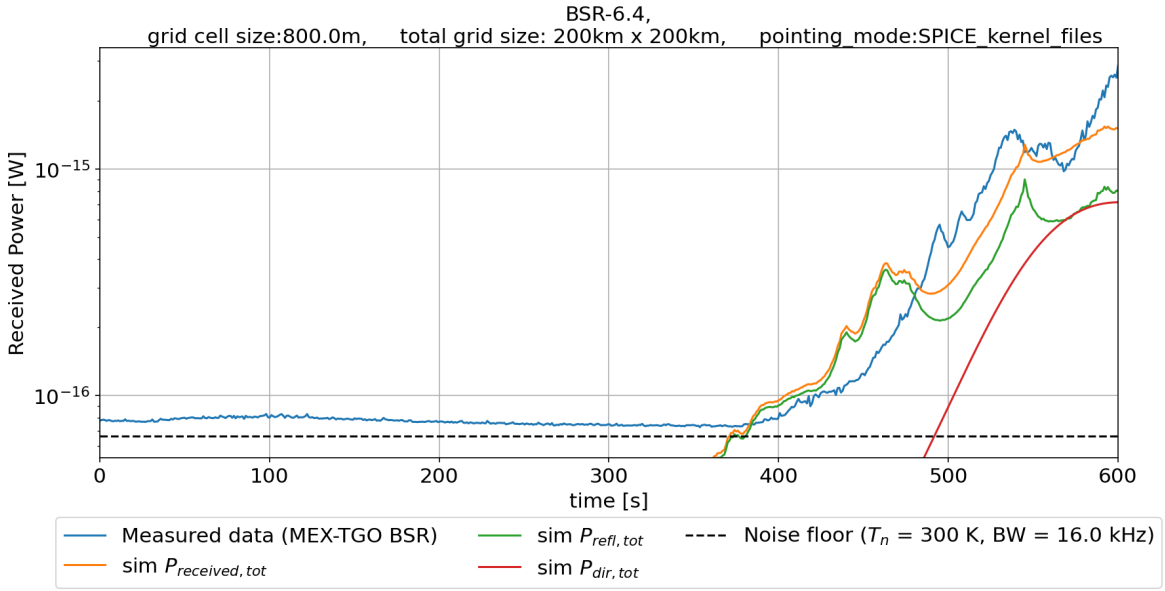

Figure 5.15: Comparison of received power model results with measured data for BSR-6.4, zoomed in.

BSR-6.5

In terms of general shape the model matches the measured data with in increase in power during the middle of the measurement and follows the occultation at the end of the measurement. What is curious is that there are several places where the data shows a peak but the model does not. Specifically the peaks around $t = 550\,\mathrm{s}$, $t = 625\,\mathrm{s}$ and $t = 675\,\mathrm{s}$. When looking at the topography around those times, the peaks seem to occur when the specular point comes close to (the rim of) a crater. In the previous measurements, passing a crater typically yielded a dip in power. A possible explanation for having peaks instead of dips here could be that the increased roughness, steep slopes, and accumulation of ejecta blocks at the crater rim create enhanced scattering which the Hagfors' scattering model does not take into account.

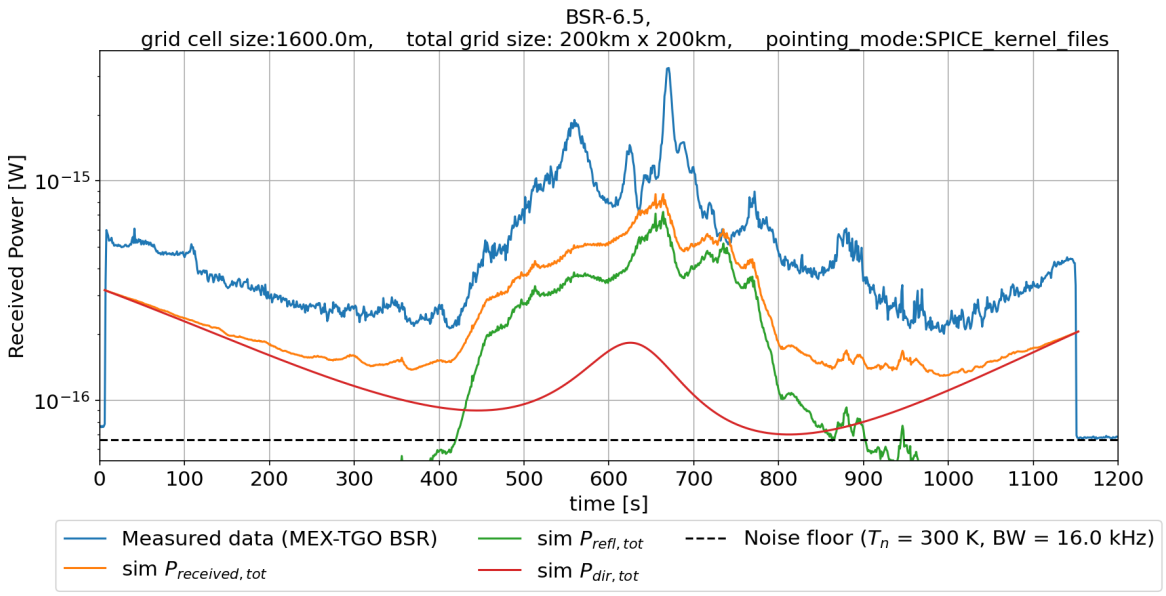

Figure 5.16: Comparison of received power model results with measured data for BSR-6.5, zoomed in.

BSR-7.1

The general shape of the model matches the measured data with the exception of the large dip in power in the measured data between $t = 275\,\mathrm{s}$ and $t = 425\,\mathrm{s}$. The terrain around that time looks actually relatively flat, so it could be that the roughness (C parameter of the Hagfors' model) is overestimated there.

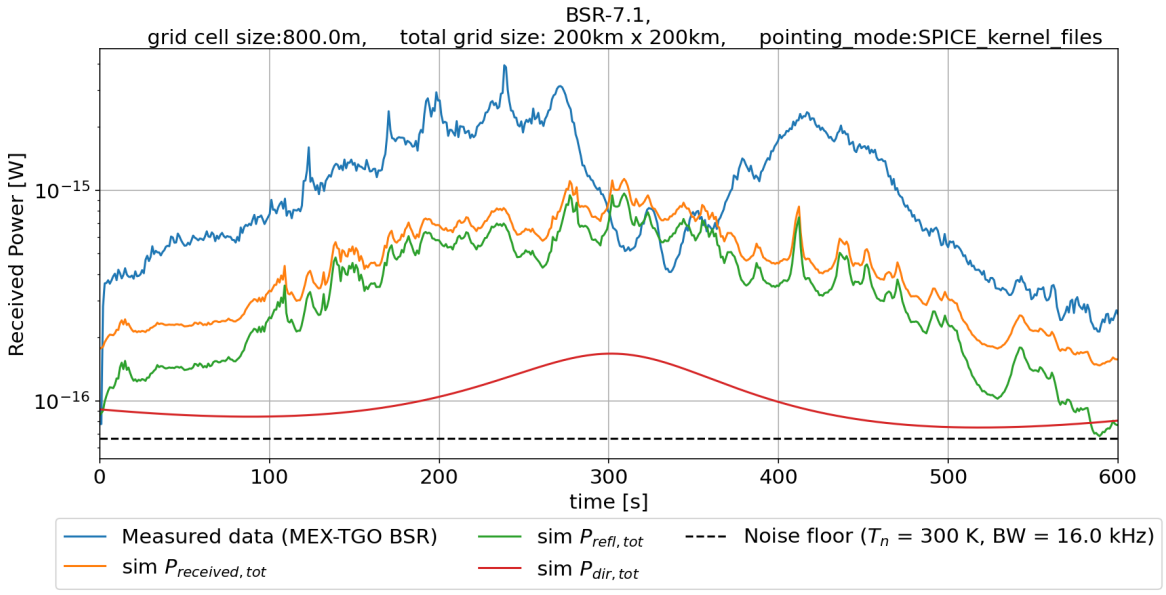

Figure 5.17: Comparison of received power model results with measured data for BSR-7.1, zoomed in.

BSR-7.2

This measurement seems very similar to measurement BSR-6.4. Once gain for the first two-thirds of the measurement the reflected and direct power are below the noise threshold. This appears to be also primarily caused by a very large TX antenna off-boresight angle (see figure B.12 in appendix B).

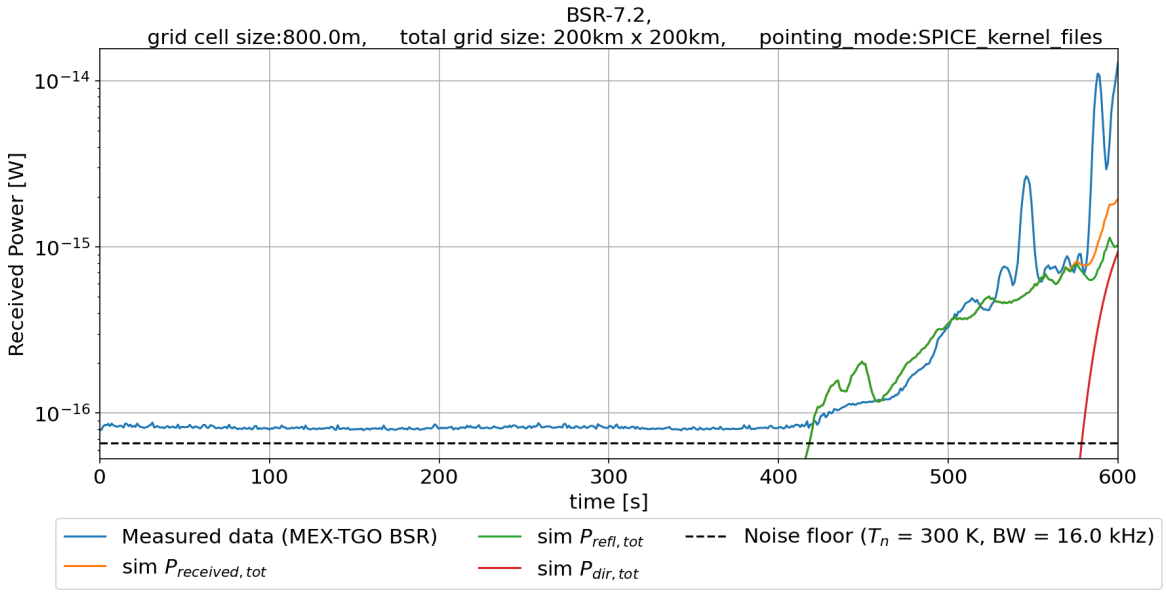

Figure 5.18: Comparison of received power model results with measured data for BSR-7.2, zoomed in.

BSR-7.3

The general shape of the model matches the data except between $t = 300\,\mathrm{s}$ and $t = 475\,\mathrm{s}$ where the measured data has a sudden increase (and then decrease) in power. However, smaller features that are on top of this large scale power change can still be seen in the model.

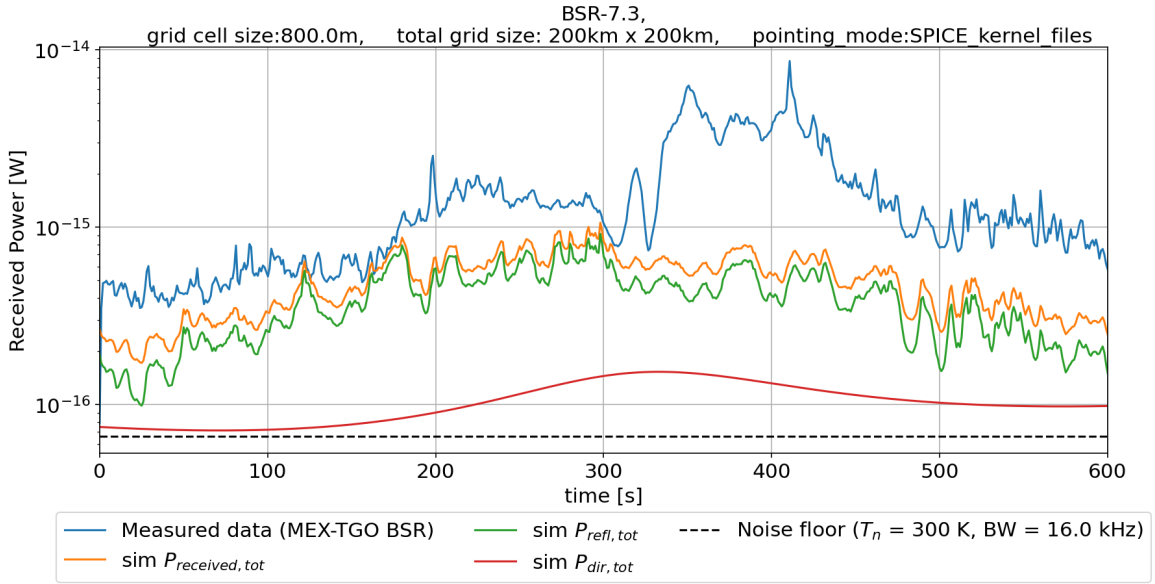

Figure 5.19: Comparison of received power model results with measured data for BSR-7.3, zoomed in.

BSR-7.4
This measurement seems very similar to measurement BSR-3.1 in the sense that the model follows most of the shape of the data extremely well and virtually every significant peak/dip in power in the data seems to be present in the model. Only at the beginning does the model stay relatively flat where the data shows some spikes, though this could just be a noisy signal.

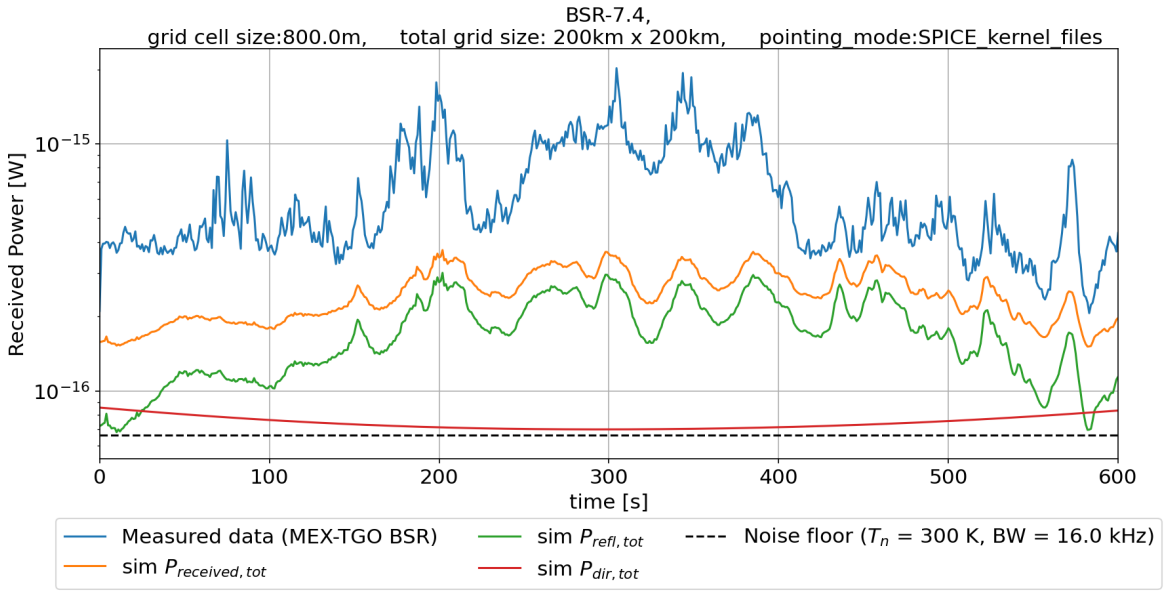

Figure 5.20: Comparison of received power model results with measured data for BSR-7.4, zoomed in.

General observations
Just as for BSR campaigns 2,3 and 4, the model results for BSR campaigns 5,6 and 7 overall seem to match the measured data (in terms of shape) very closely. However, just as before, there are still some places where there is a mismatch between the model and the measured data. The differences at the very end of BSR-5.1, the very end of BSR-6.2, peaks during in the middle of measurement BSR-6.5 and the mismatch between$t = 300\,\mathrm{s}$ and $t = 475\,\mathrm{s}$ for BSR-7.3 all seem to occur when the incidence angle is relatively low (below $45\,°$). So this could again be an indication that the reflected power is underestimated for these low incidence angles. However for the mismatch between $t = 275\,\mathrm{s}$ and $t = 425\,\mathrm{s}$ for BSR-7.1 the opposite seems to happen. There, although the incidence angle is once again relatively low, the measured power decreases instead of increases. This could of course also be caused by something unrelated, but it is surprising to observe.

5.2.5. Signal polarization impact
One of the important improvements (compared to Nieuwenhuizen [35]) was the implementation of the polarization dependence of the antenna patterns and the reflectivity. Therefore the decomposition of the RHCP and LHCP reflected signals are shown for BSR-2.1 to BSR-4.1 in figures 5.21 to 5.24. The polarization plots for the other measurements can be found in appendix B.

These polarization plots shows that the RHCP and LHCP components of the reflected power are usually very similar in shape (suggesting that the topography is the driving factor of these power fluctuations) and that the LHCP component comes very close to the RHCP component for lower incidence angles (in terms of absolute power) but that for higher incidence angles the LHCP component drops off very hard (as expected), which can be clearly seen for example near the end of measurement BSR-4.1 (there the incidence angle steadily increase) as well as measurements BSR-6.3, BSR-6.5 and BSR-7.1 (see appendix B).

What is interesting to see is that for BSR-3.1 the LHCP component is actually dominant, underlying the importance of modeling both polarizations. Perhaps this could also partially explain why the model is

consistently lower in power than the data as the MEX cross-polarization is not modeled (although this is of course very uncertain given that the calibration of the AGC data is still not available).

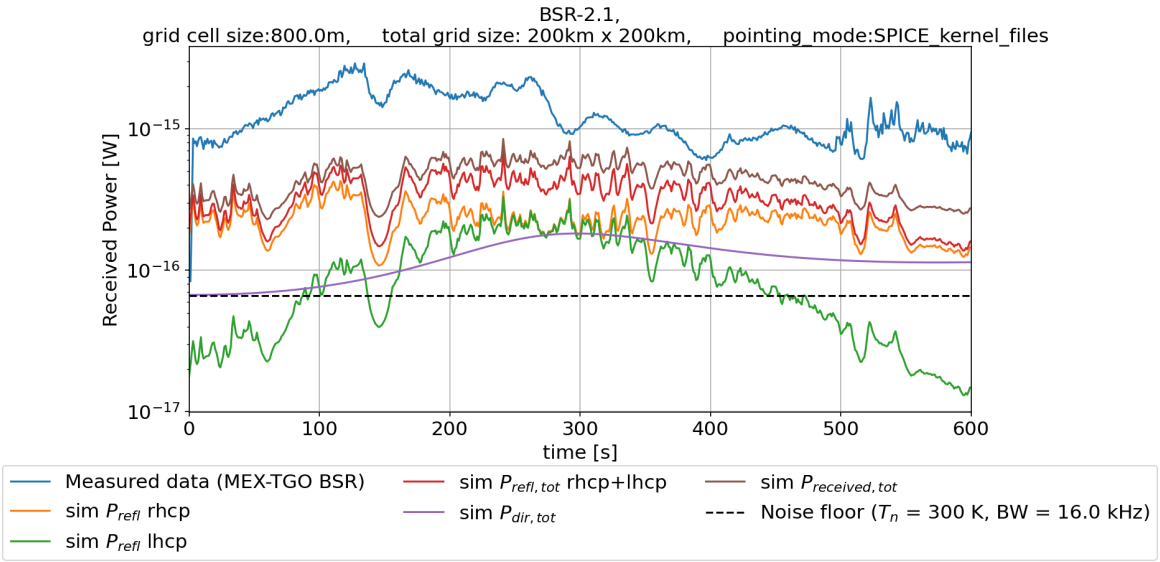

Figure 5.21: Received power results for co-pol and x-pol receiver antenna polarizations for BSR-2.1.

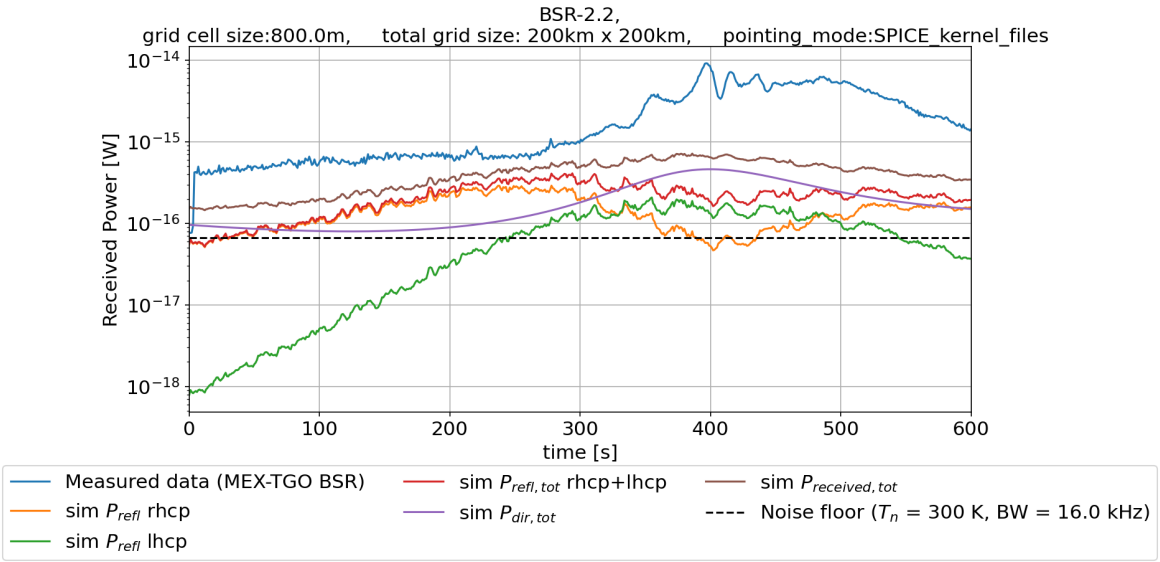

Figure 5.22: Received power results for co-pol and x-pol receiver antenna polarizations for BSR-2.2.

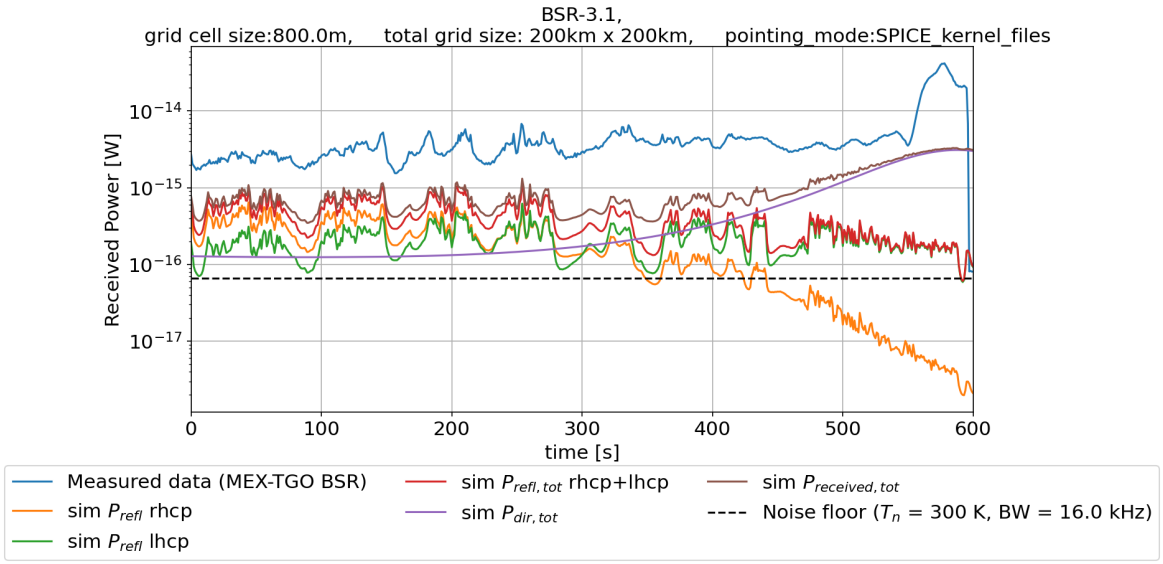

Figure 5.23: Received power results for co-pol and x-pol receiver antenna polarizations for BSR-3.1.

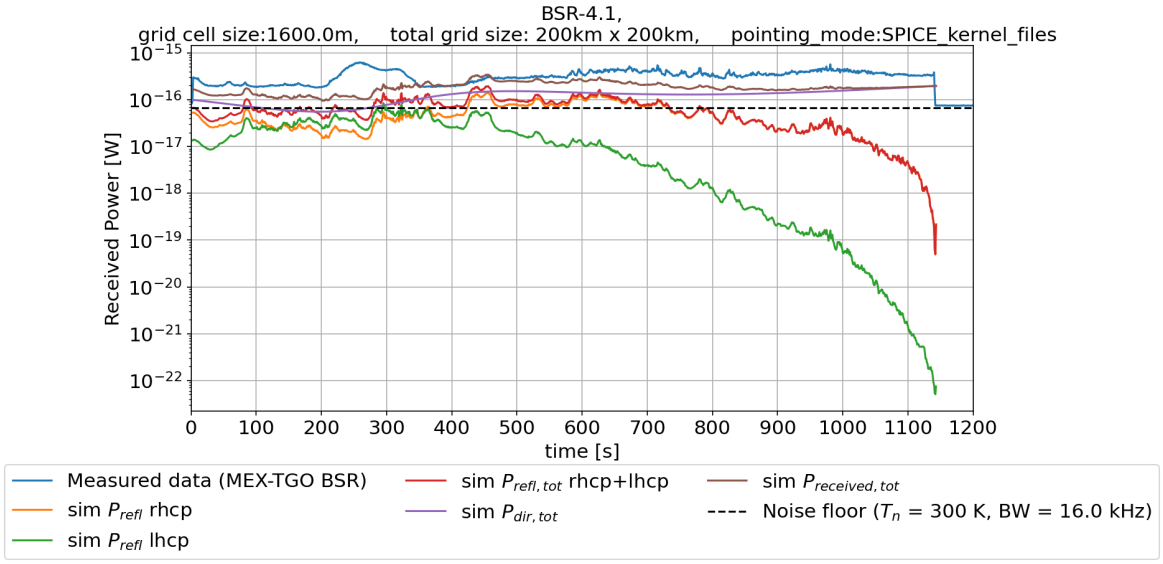

Figure 5.24: Received power results for co-pol and x-pol receiver antenna polarizations for BSR-4.1.

5.2.6. Specular point pointing

The initial hypothesis was that by pointing towards the specular point, the TX and RX gain would increase for the reflected power. Actively pointing towards the specular point for an entire measurement would require more resources from an operational standpoint (fuel consumption, maneuver planning, etc.), so it's important to investigate if this would yield a significant better SNR.

The plots showing the power for specular point pointing for BSR-2.1 to BSR-4.1 are shown in figures 5.25 to 5.28. The plots for the other measurements can be found in appendix B.

What can be seen in virtually all the figures is that, although the reflected power is higher than in the default (nadir) pointing case, the direct power is much higher than the reflected power, meaning that any variations in reflected power are essentially overpowered by the direct signal. So here the SNR is not driven by the noise power but by the direct power. This means that, for the current setup, using specular pointing would actually give a worse SNR (as the reflected power is the desired signal) instead of increasing it. These results came initially as a surprise but can be easily explained. When pointing towards the specular point, the off-boresight angles for the direct power signal decrease compared to conventional nadir-pointing considering geometries with medium/high incidence angles (in the limit of an incidence angle of $90\,^\circ$ the TX and RX would be directly pointing to each other). This apparently increases the direct signal by such an amount that it becomes much larger than the reflected power.

This problem could be solved by using a LHCP transmitting antenna with a RHCP receiver antenna (or the other way around). This solution works twofold. Firstly, measurements could take place at much lower incidence angles (as the LHCP to RHCP Fresnel coefficient is higher for low incidence angles, see again figure 2.3). When using specular pointing, this would decrease the direct power as the off-boresight angle would be much greater. This is under the assumption that enough measurement opportunities with low incidence angles exist. Secondly, by having different co-polarizations for the TX and RX antennas the direct power will be much lower (because then one of the gain patterns will always be the cross-polarization patterns which is much weaker).

Another possible solution would be to attempt to remove direct signal component by for example subtracting the modeled direct power. However, given the limited knowledge of the detailed TGO antenna pattern for the two polarizations, it is unlikely that this would succeed. One would likely just be left with noise. For this approach to have a chance of working the resolution (in terms of power) should be much smaller than the variations in the reflected power signal.

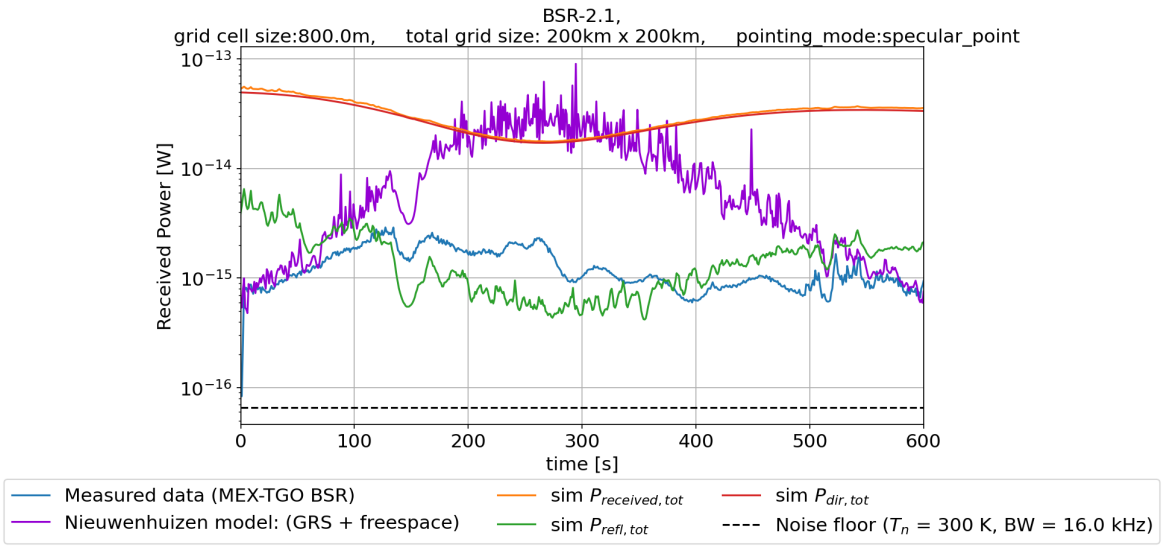

Figure 5.25: Comparison of received power model results for specular point pointing with measured data and Nieuwenhuizen [35] model for BSR-2.1.

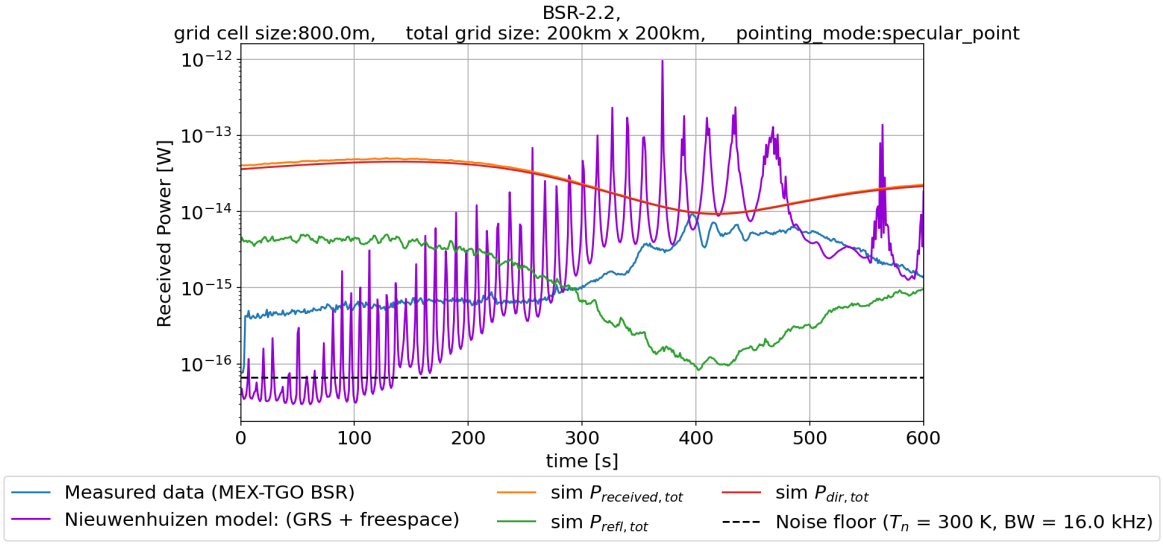

Figure 5.26: Comparison of received power model results for specular point pointing with measured data and Nieuwenhuizen [35] model for BSR-2.2.

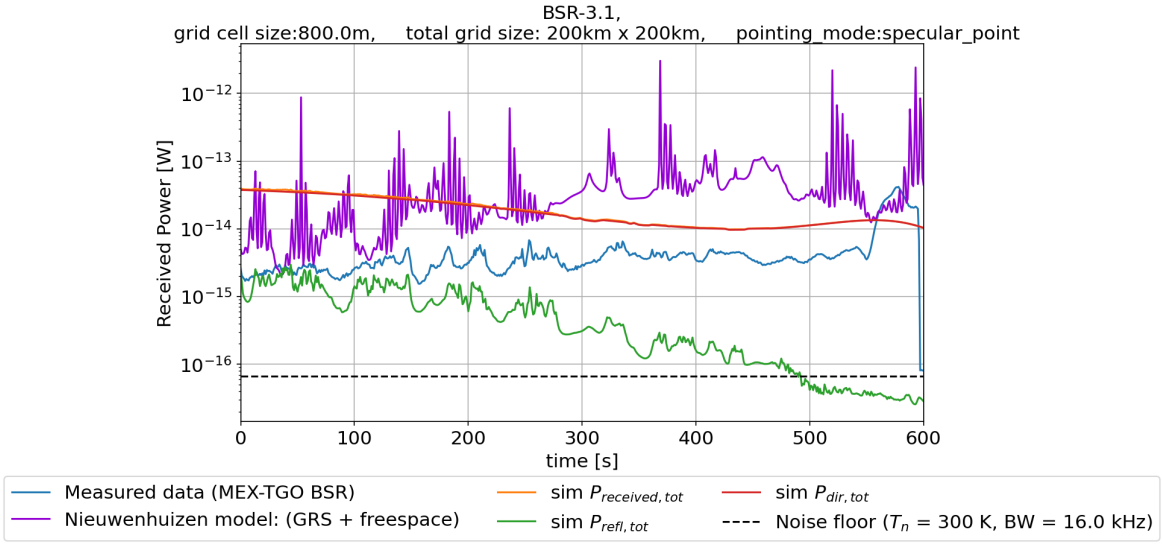

Figure 5.27: Comparison of received power model results for specular point pointing with measured data and Nieuwenhuizen [35] model for BSR-3.1.

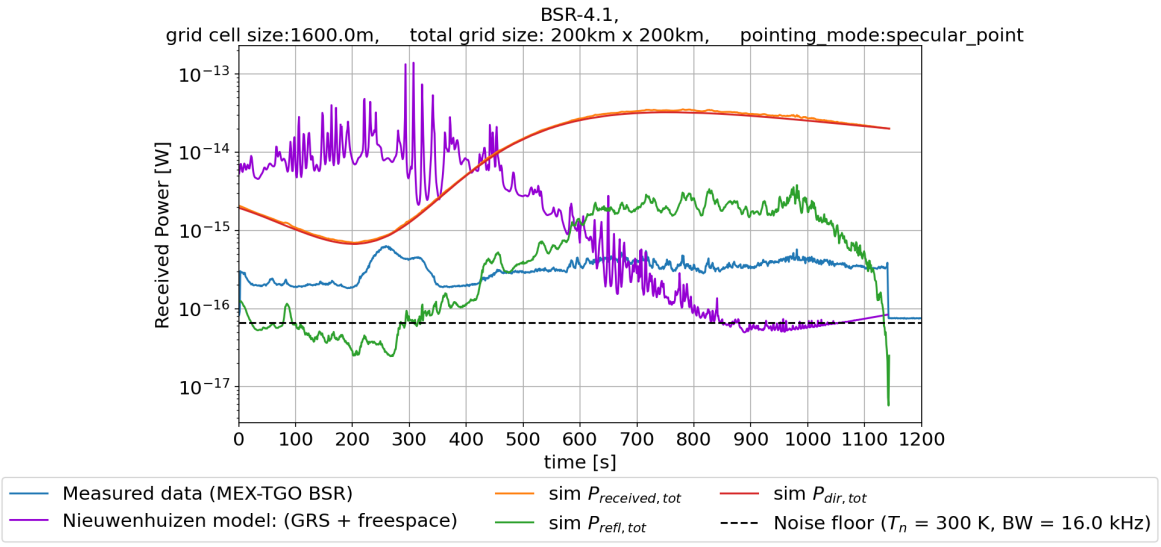

Figure 5.28: Comparison of received power model results for specular point pointing with measured data and Nieuwenhuizen [35] model for BSR-4.1.

5.2.7. Permittivity effect on model

One of the research questions stipulated the investigation of the influence of simulation parameters on the received signal. One important parameter in this regard is the surface permittivity. This is an important parameter because detection of subsurface water ice as well as soil moisture retrieval often mentioned in the studied GNSS-R literature all rely on changes in permittivity caused by the presence of water (ice) in the surface. Therefore the capacity of the model to distinguish differences in power caused by differences in permittivity is extremely important to assess the ability of the model to detect subsurface water.

In section 2.2.1 the effect of incidence angle and permittivity on the reflectivity was discussed. On the one hand rr reflectivity decreased for increasing permittivity but rl reflectivity increased for increasing permittivity. As measurements have varying incidence angles and both LHCP and RHCP signal reflections it is important to investigate the overall effect of changing the permittivity on the received power.

First, results for measurement BSR-2.1 will be explored, which overall has a higher lr than rr reflectivity (see figure B.1 in appendix B). figure 5.29 shows the reflected power for three different relative permittivities ($\epsilon_r = 4, 6, 8$). For nearly the entire measurement the simulation with the lowest permittivity has the lowest reflected power and the highest permittivity has the highest power. This is as expected because the lr reflectivity is dominant for this measurement. In figure 5.30 the absolute differences in reflected power for the three permittivities is shown. Here it is important to see if the difference is large enough to be detected. In the middle of the measurement the differences in power rise above the noise floor, so if the receiver antenna power resolution is high enough, these differences in permittivity could be measurable. However at the beginning and end of the measurement the difference in power drops below the noise floor, so this would not be measurable. So for relative permittivity differences of 2.0 the model indicates that it would be critical whether this difference is detectable or not, depending on the resolution.

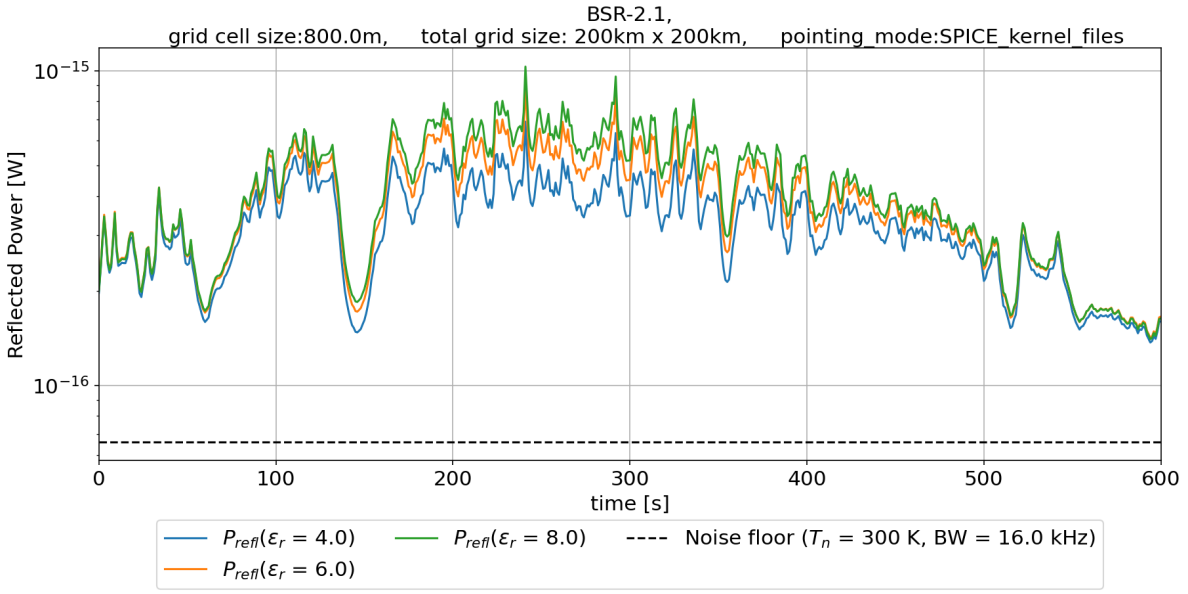

Figure 5.29: Comparison of reflected power model results for several permittivities for BSR-2.1.

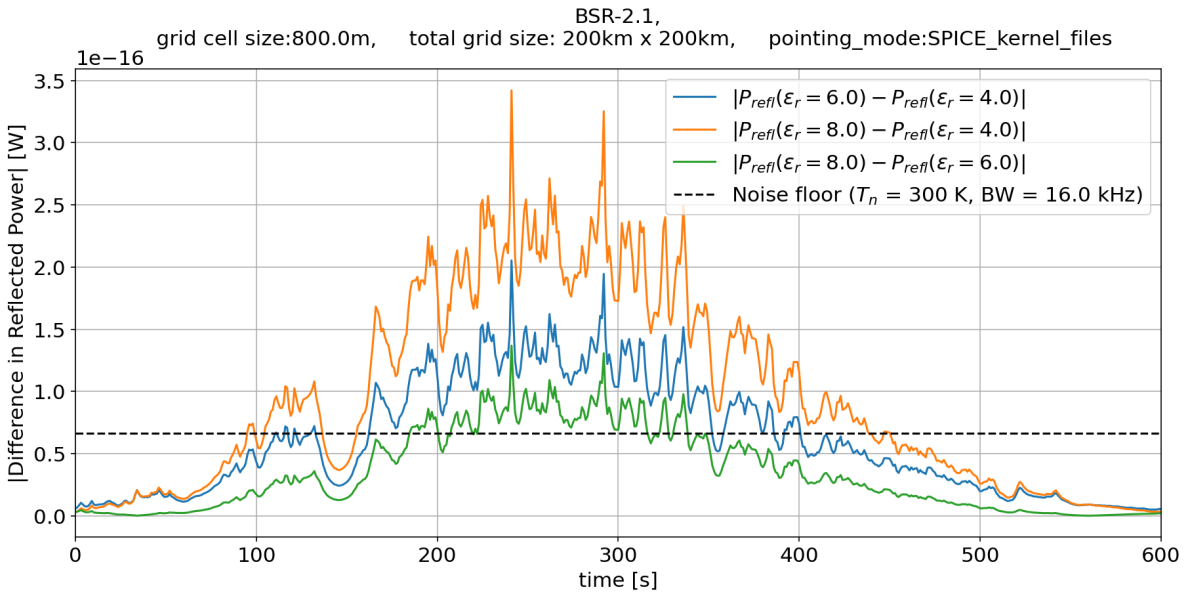

Figure 5.30: Absolute difference in reflected power between model results for several permittivities for BSR-2.1.

Next, results for measurement BSR-7.4 will also be explored. BSR-7.4 has a rr reflectivity that is generally (a little bit) higher than the lr reflectivity (see figure B.14 in appendix B), so it will be interesting to see if this will change the results.

figure 5.31 shows the reflected power for three different relative permittivities ($\epsilon_r = 4, 8, 12$). It is not very easy to see but the fact the rr reflectivity is now dominant indeed changed. At the beginning and at the end of the measurement it appears now that the lowest permittivity has the heighest reflected signal. In the middle of the measurement the middle reflectivity ($\epsilon_r = 8$) actually appears to be the strongest. Perhaps because during the middle of the measurement the rr and lr reflectivities are nearly equal. When looking at the absolute differences in reflected power in figure 5.32, the results are unfortunately not very encouraging. The differences in power are well below the noise floor, so not even a relative permittivity difference of 8.0 would be detectable.

The difference of BSR-2.1 and BSR-7.4 for the absolute power difference is probably because the reflected power for BSR-2.1 is much larger (almost $1 \times 10^{-15}\,\mathrm{W}$) compared to BSR-7.4 (just reaching $3 \times 10^{-16}\,\mathrm{W}$). So the absolute power of the measurement could be critical for the ability to differentiate between different permittivities. Additionally, the difference in reflectivity for different permittivities is usually larger for the lr than for the rr reflectivity (see figure 2.3), so that likely also partially explains the good results for BSR-2.1.

It is important to keep in mind that the differences in power here are due to a change in permittivity of the entire grid. For the search for example water ice the area with different permittivity will of course be localized to a certain area of the grid. Nevertheless, these results should give a general idea about the behavior of the reflected power for different permittivities and what kind of permittivity differences could potentially be differentiated with the current setup with MEX and TGO.

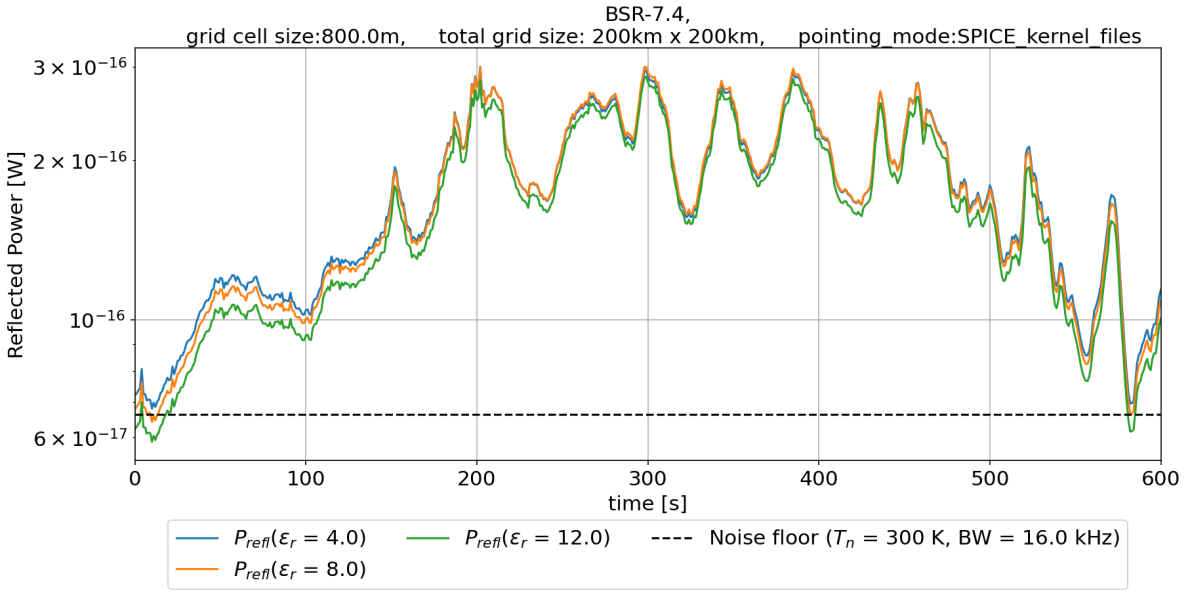

Figure 5.31: Comparison of reflected power model results for several permittivities for BSR-7.4.

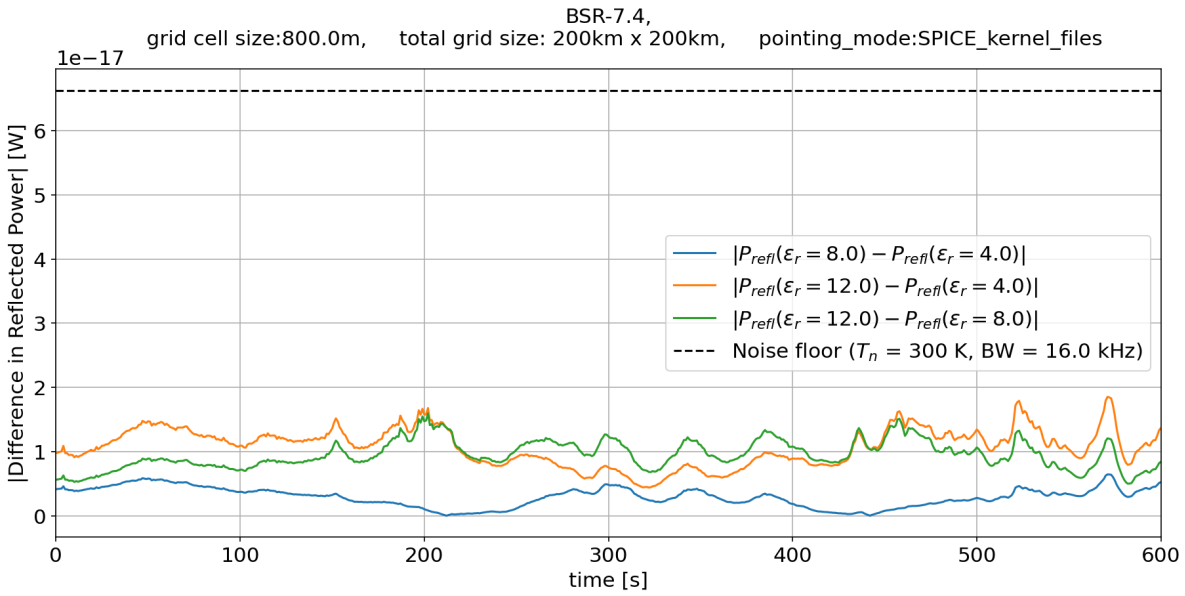

Figure 5.32: Absolute difference in reflected power between model results for several permittivities for BSR-7.4.

5.2.8. Spatial resolution

In section 2.6 it was mentioned that if the surface roughness is low enough the power mainly comes from the first Fresnel zone, but that natural surface typically have a much larger glistening zone. Thus it is important to investigate the spatial resolution of the bistatic measurements. First, Delay-Doppler Maps (DDMs) without WAF convolution of measurement BSR-2.1 at two different times will be investigated. One at $t = 150\,\mathrm{s}$ when passing the Louth crater to see the effect of topographical features on the spatial resolution, and one at $t = 300\,\mathrm{s}$ (middle of the measurement) when the terrain is more flat. These DDMs are shown in figures 5.33 and 5.34.

Theses figures both show a broad horseshoe shape associated with incoherent scattering. The apex of the horseshoe (near the SP) is where the signal power is strongest, as expected. The arms of the horseshoe extend along the axes of the DDM, representing the scattering from surrounding areas. There can still be seen significant power coming from these surrounding areas (points further away from the SP), but do note the non-linear color scale. It appears that the assumption that the power mainly comes from the first Fresnel zone does not seem to apply for these simulations (at least for BSR-2.1), but that the power seems to come from a much larger area. What can also be observed is that the DDM for the Louth crater does not exhibit a very clear horseshoe shape, but especially near the SP seems to be much 'noisier'. This is likely due to the topography of the crater causing grid cells close to the SP to have relatively large differences in delay.

To confirm that the reflected power originates from a larger area, the reflected power plotted on the surface grid will also be explored. These are shown in figures 5.35 and 5.36. It is indeed clear that the power is coming from an area much larger than the first Fresnel zone (which is only in the order of $1\,\mathrm{km}$ in size for measurement BSR-2.1.). In figure 5.35 the crater and its surrounding area can clearly be seen. The crater edge seems to reflect very little power (which explains the drop in power seen at $t = 150\,\mathrm{s}$ in the power of BSR-2.1) and the most power appears to come from the area surrounding the crater. In figure 5.36 the majority of the power does seem to come from the area around the SP. But even here, where there is a lot less topographic difference compared to the Louth crater, the area where the power appears to originate from is in the order of tens of kilometers.

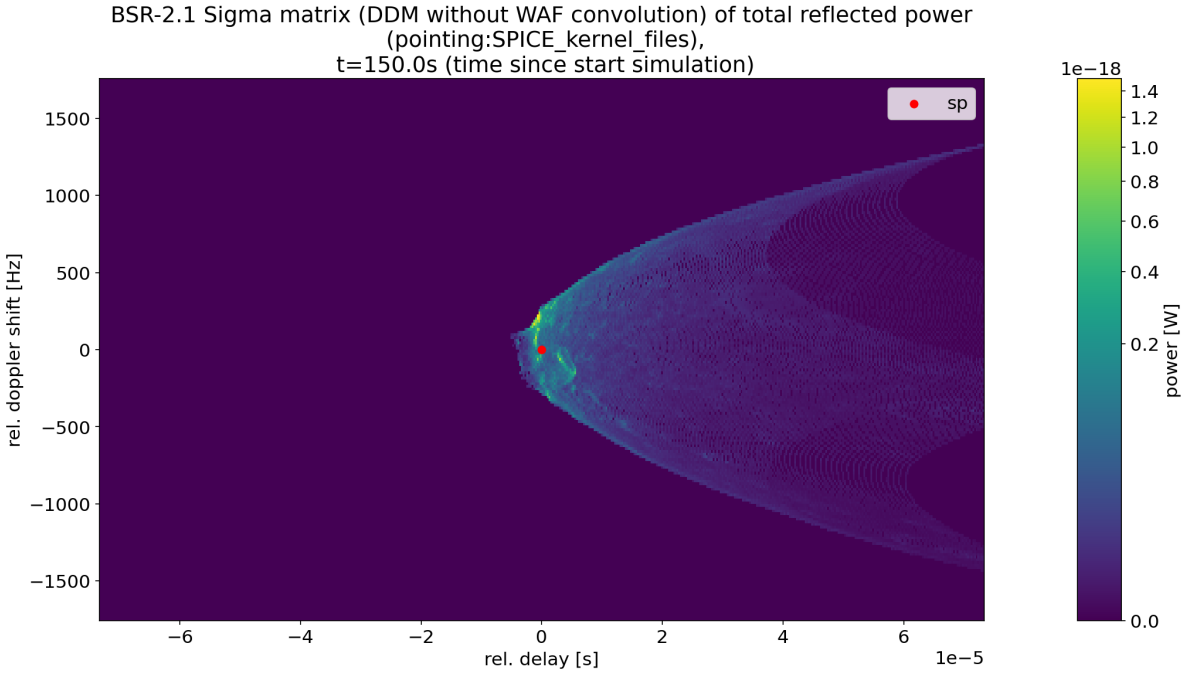

Figure 5.33: DDM (without WAF convolution) for the reflected power for BSR-2.1 at $t = 150\,\mathrm{s}$. Delays and Doppler shifts are expressed relative to those of the SP.

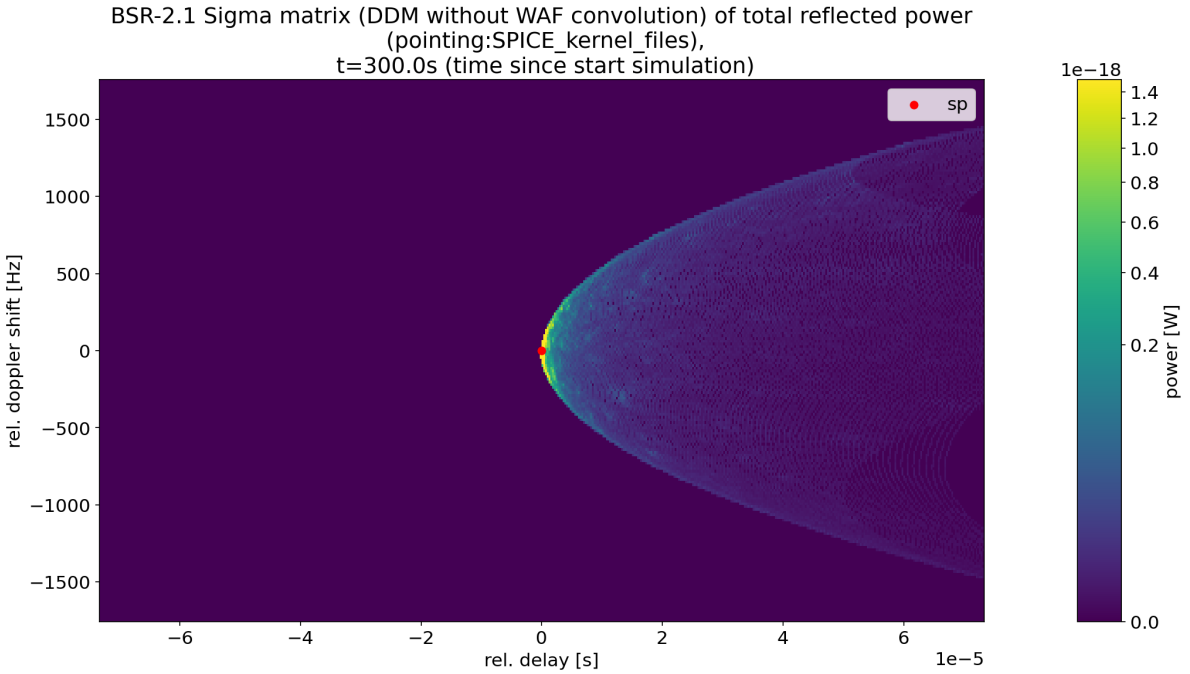

Figure 5.34: DDM (without WAF convolution) for the reflected power for BSR-2.1 at $t = 300\,\mathrm{s}$. Delays and Doppler shifts are expressed relative to those of the SP.

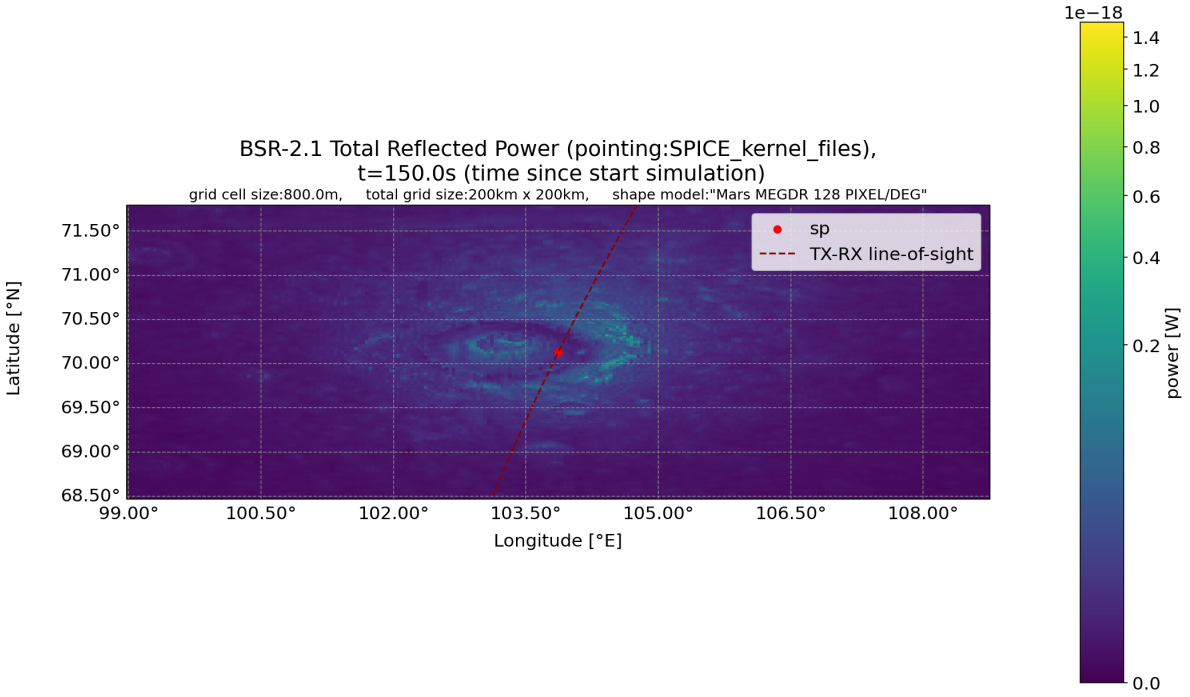

Figure 5.35: Reflected power of the simulation surface grid for measurement BSR-2.1 at $t = 150\,\mathrm{s}$.

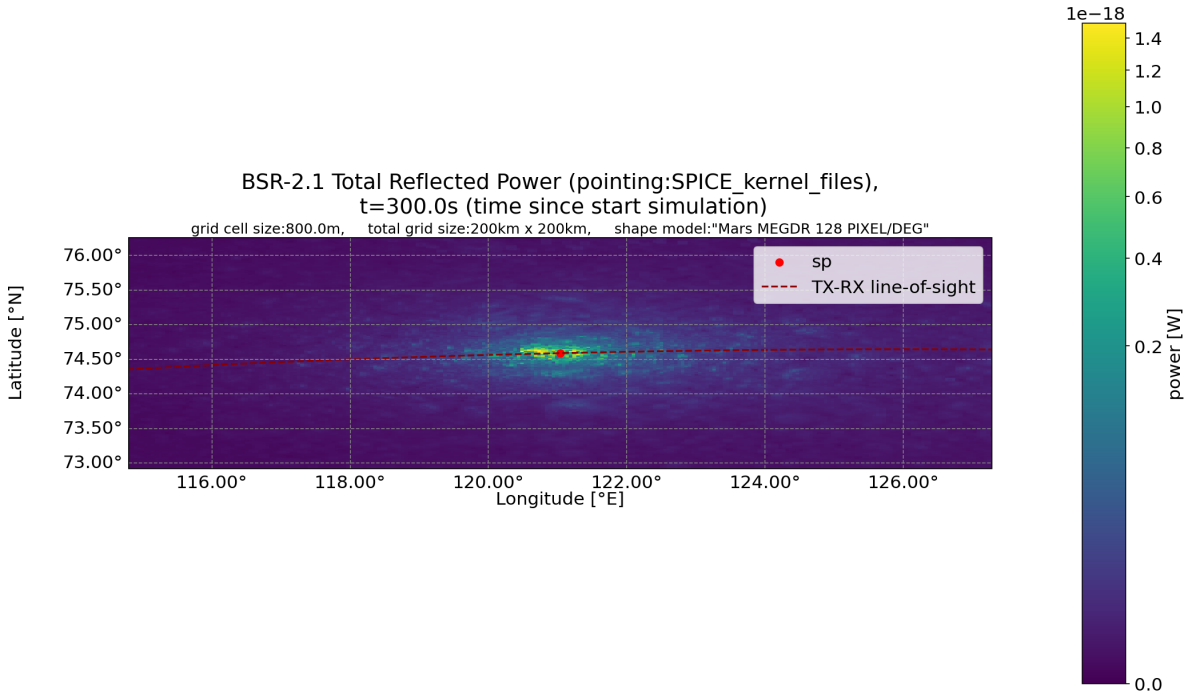

Figure 5.36: Reflected power of the simulation surface grid for measurement BSR-2.1 at $t = 300\,\mathrm{s}$.

5.3. Optimal incidence angle

One of the research goals was to investigate key parameters for (future) measurements. An important geometry parameter is the incidence angle of a measurement, as it has a high influence on the reflectivity and thus the total received power. So it would be relevant to know the optimal incidence angle for a measurement. To simplify this problem, it will be assumed that the planet is spherical and that the bistatic geometry constraints are satisfied (so TX, RX, SP and SP normal vector are all in one plane, essentially making it a 2D problem). Then for a given TX and RX distance to the SP (and planet radius) all the relevant angles and distances can be calculated using the law of cosines. This can be done for the case that the spacecraft are pointing towards the center of the planet and for the case that they are pointing towards the SP. Note that the results are highly dependent on the TX and RX antenna patterns. So any conclusions based on the results here can only be applied to measurements with MEX and TGO.

There are several ways to define what is an 'optimal' incidence angle. Firstly, an optimal incidence angle which yields maximum reflected power will be considered. The results for this (for a set of TX to SP and RX to SP distances) are shown in figure 5.37. For pointing towards the SP, all the distances result in an optimal incidence angle of $90\,°$ (it's a bit difficult to see in figure 5.37 as all the lines for target body center are on top of each other). This is not surprising as MEX and TGO both have a RHCP co-polarization, and going to $90\,°$ maximizes the rr reflectivity. For nadir pointing (TX and RX pointing towards the center of the target body), the optimal incidence angle is actually dependent on the distances. It appears to be approximately linearly dependent on both the TX to SP and RX to SP distance. The optimal incidence angle is on the higher side which would make sense given the MEX and TGO co-polarizations. For most measurements between MEX and TGO the distances to the SP typically change quite a lot during a measurement. So searching measurement opportunities for one specific optimal incidence angle is not viable, but these results do indicate that searching measurements with higher incidence angles would be beneficial (for the reflected power).

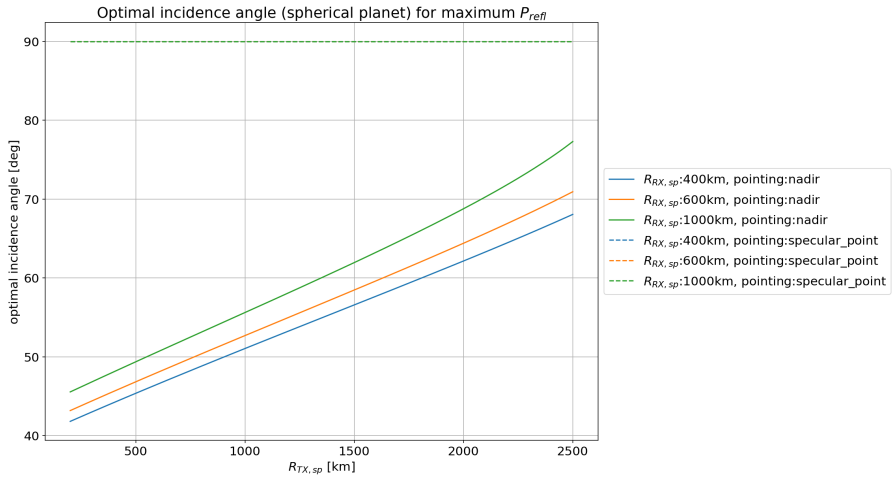

Figure 5.37: Optimal incidence angle (for a spherical planet) for maximum reflected power as function of the TX-SP distance and RX-SP distance.

However, only looking the the reflected power is insufficient (especially for SP pointing). As was seen earlier, pointing towards the specular point led to a very high direct power signal (for the measurement geometries of the performed measurements). Therefore it could also be relevant to look which incidence angles minimize the direct power. This is shown in figure 5.38. For SP pointing the optimal incidence angle is $0\,°$ nearly everywhere, which makes sense as this means the antenna boresights are essentially parallel (one antenna is pointed towards the back of the other antenna). The exception seems to be a small bump just after the TX and RX distance to the SP are equal. This could be because the antennas are so close that increasing the incidence angle, which increases the distance between the antennas, has a stronger effect than the effect of the antennas pointing a little bit more towards each other. For planet center pointing, this effect can be seen as well. When the distance between the spacecraft becomes a dominant factor in the direct power, the optimal incidence angle jumps to a much higher value, increasing the distance. But for any other distance (where the off-boresight angles for the direct power are the dominant factor), the optimal incidence angle is $0\,°$.

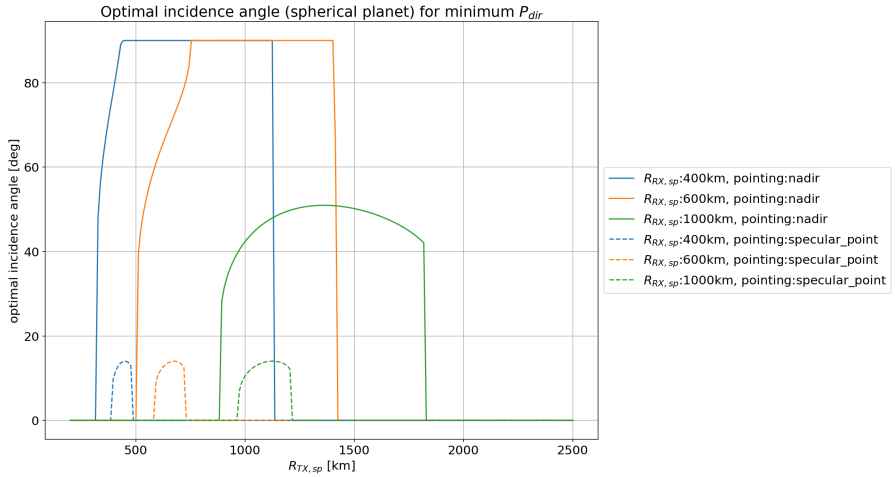

Figure 5.38: Optimal incidence angle (for a spherical planet) for minimum direct power as function of the TX-SP distance and RX-SP distance.

Especially for SP pointing, there are conflicting goals. On the one hand, to maximize the reflected power the incidence angle should be as high as possible. On the other hand to reduce the direct power the incidence angle should be near $0\,°$. A way to try to take into account both of these goals is to look at the ratio of reflected power to direct power. So, the optimal incidence angle which maximizes the ratio of reflected power to direct power can be investigated. This is show in figure 5.39.

For most TX to SP and RX to SP distances, considering planet center pointing, the optimal incidence angle remains between $40\,°$ and $60\,°$. However for very low and very high TX to SP distances, it seems that a low incidence angle to keep the direct power low is more important than having high reflectivity. Looking at SP pointing, a similar behavior to planet center pointing can be observed but at a more extreme scale. For a low enough TX to SP distance the incidence angle is kept at nearly $0\,°$, prioritizing the effect of the direct power. However for a high enough TX to SP distance, the reflected power is the dominant factor with the incidence angle at nearly $90\,°$. And the switch between these two regimes is extremely steep. This is bad news for any chance of using SP pointing under the current configuration. In the very low incidence angle region, although the ratio of reflected to direct power might be optimized, the absolute value of the reflected power will likely be very low. On the other hand, the high incidence angle region only leaves measurements near occultation and even then it is unlikely that this will increase the reflected power enough to surpass the direct power (for example at the end of measurement BSR-4.1 when it is near occultation the direct power is still much higher than the reflected power).

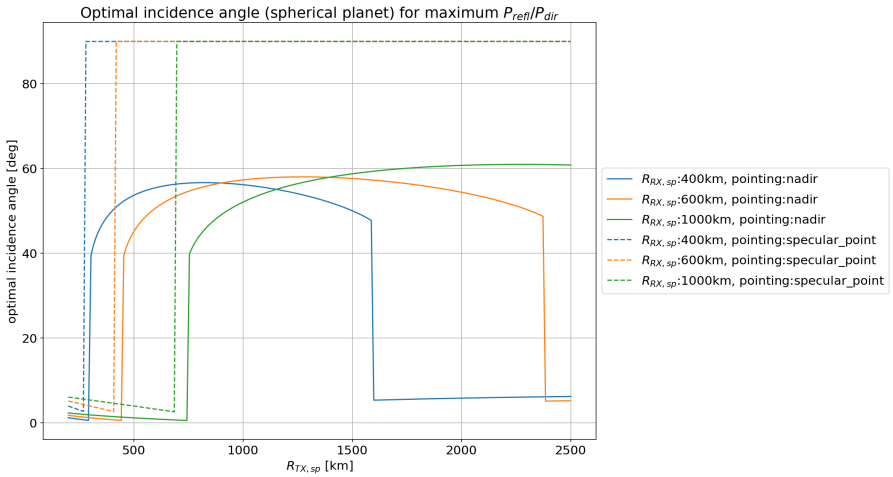

Figure 5.39: Optimal incidence angle (for a spherical planet) for maximum reflected power to direct power ratio as function of the TX-SP distance and RX-SP distance.

6

Conclusions & Recommendations

In this thesis, an improved model for the simulation of bistatic radar measurements between MEX and TGO was created, along with a model to search and rank bistatic measurement opportunities. The conclusions of this research are presented in section 6.1 and and recommendations for future work are discussed in section 6.2.

6.1. Conclusions

The conclusions for this thesis will be discussed based on the research questions which were presented in chapter 1.

6.1.1. RQ1: How can a set of Mars bistatic radar measurements between MEX and TGO be modeled to use the (full resolution) Mars MOLA DEM?

The bistatic measurements were modeled in Python with the help of the SPICE toolkit. To be able to use the full spatial resolution (in a reasonable computation time) for the Mars 128 pixel per degree MOLA DEM, dedicated SPICE DSK files of the MOLA DEM were used (provided by ESA on their FTP server). This in comparison to Nieuwenhuizen [35] who used MEGRD data files. This meant that dedicated SPICE functions could be used for conversion from (planetocentric) longitude/latitude coordinates to rectangular surface point coordinates, the calculation of the surface normal vectors, and the calculation of the illumination angles (incidence and emission angles) associated with these surface points. This allowed for a significant increase in computational speed and therefore the full resolution could be used. SPICE kernels were also used for ephemeris and attitude data for the MEX and TGO spacecraft (and Mars). The model also incorporated the effects of the polarization of the MEX and TGO antennas to better model the reflected power. A bistatic geometry search script was also created (also implementing the SPICE toolkit) to determine the SP surface coordinates needed for the grid generation.

RQ1.1: How do the modeled bistatic radar measurements of MEX-TGO compare to the initial model created by Nieuwenhuizen [35] and the actual MEX-TGO measurement data?

Overall it can be concluded that the increase in spatial resolution significantly improved the accuracy of the simulated measurements. The measurement simulation model showed significant improvement compared to Nieuwenhuizen [35], as it did not show any sign of ripple/periodic oscillations or signal mirroring effect seen in the model of Nieuwenhuizen. Moreover, the model almost always matches the general shape of the measured data (all be it with less power/ over a smaller power scale) and many spikes/dips in power caused by geographic features like craters are observable in the model. There are however certain features in the power data that were not present in the model. These were mainly present when the incidence angle became small. A possible explanation for this could be the missing transmitted LHCP signal component from the MEX MelaCom antenna (for which no antenna pattern was available found and thus is not modeled).

RQ1.2: Where can GNSS-R principles/techniques be applied to Mars bistatic radar measurements?
Several principles of GNSS-R were used throughout the bistatic measurement model. First of all, the delay doppler maps (all be it without the WAF convolution used for PRN coded signals) were implemented to help visualize the type of scattering (coherent vs incoherent) and where the majority of the reflected power is coming from. The effect of the polarization of the antennas on the reflectivity was also an important principle that was implemented into the model. Also, the principle of detecting water/ice based on permittivity changes was touched upon.

6.1.2. RQ2: What are key parameters for future measurements to obtain the optimal received signal?

It was found that the incidence angle together with the antenna polarizations play an important role to achieve the best reflected signal power due to the large dependence of the reflectivity on both of these parameters. Furthermore the pointing of the two spacecraft also plays a key role for the reflected signal due to the (undesired) direct signal component that can arise under certain pointing conditions.

RQ2.1: How do (instrumentation/geometry) parameters like spacecraft pointing, antenna polarization, permittivity, etc. influence the received signal?
The antenna polarizations were found to be an important parameter in several ways. First of all, considering both the co- and cross-polarizations of the antennas was found to be of big importance as the LHCP reflected power component can come very close (or even surpass) to the RHCP reflected power component (in terms of absolute power) depending on the incidence angle. Furthermore, because MEX and TGO both have a RHCP co-polarization, the rr reflectivity highly influences the received power. This also influences the behavior of the different pointing modes.

Pointing directly towards the SP (instead of the nominal nadir-pointing attitude) was investigated but it was found that SP pointing is not a viable strategy to increase the reflected power because it caused the direct power to be much higher than the reflected power, removing any details from the reflected power signal. This is because when using SP pointing the spacecraft are automatically pointing more towards each other and because MEX and TGO both have the same co-polarizations the gain for the direct power is very high. For the default (nadir) pointing this was not found to be a problem due to the higher off-boresight angles for the direct power in that case.

The permittivity sensitivity of the received signal was also investigated. It was found to influence the reflected power in different ways depending on whether the rr reflectivity or rl reflectivity was dominant. The sensitivity of the reflected power was shown to be (just) above the noise floor for differences in relative permittivity of 2.0, but that this heavily relied on the absolute reflected power of the measurement being significantly large enough.

Finally, an investigation of the optimal incidence angle was also performed. This yielded that when optimizing for maximum reflected power the optimal incidence angle for nadir pointing (pointing towards the planet center) lied between $40\,^\circ$ and $80\,^\circ$ depending on the TX and RX distances to the SP. For SP pointing it was found to be $90\,^\circ$ regardless of the TX or RX distance to the SP. Optimal incidence angle investigations for minimizing the direct power and maximizing the reflected to direct power ratio were also performed to investigate the SP pointing direct power problem but these only showed that SP pointing with the current antenna polarization configuration is not feasible.

RQ2.2: When are there suitable opportunities for bistatic measurements for 2026, with MEX and TGO?
A large amount of measurement opportunities was found for June,July and August of 2026. These opportunities were then ranked based on several (geometry) parameters, including the whether any ROIs were intersected and the first seven opportunities were shown in figure 5.4.

6.2. Recommendations

Based on the work done in this thesis, there are several recommendations that can be made. These are separated into recommendations for future work and recommendations for future bistatic radar missions.

6.2.1. Recommendations for future work:

- Investigate GNSS-R techniques (DDM with PRN code, polarization ratio, etc.) in more detail and investigate relevant hardware requirements.
- Verify power measurements to get an accurate value for the power in Watts for MEX and TGO *Already planned, once the calibration data for MEX and TGO becomes available it would be very interesting to compare the absolute power of the measurement data and the model.*
- Validate the model with measured data from bistatic measurements at Earth/other planetary bodies (Moon, Venus, ...) *The model is in principle set up in such a way that it could easily be used for different spacecraft at different planetary bodies (as long as the relevant data is available in SPICE)*
- Investigate bistatic measurement opportunities with other spacecraft at Mars.
- Investigate different scattering models.
- Adding a more accurate permittivity model for Mars.
- Include MEX cross-polarization in the model.
- Include azimuth dependence in antenna pattern modeling.

6.2.2. Recommendations for future bistatic reflectometry missions:

- Different co-polarizations for the TX and RX antennas. *To reduce the direct power signal problem, potentially allowing for SP pointing.*
- Increase receiver signal resolution. *Currently half of resolution is not used as it is below the noise floor.*

References

[1] Andrew M. Annex et al. “SpiceyPy: a Pythonic Wrapper for the SPICE Toolkit”. In: *Journal of Open Source Software* 5.46 (2020), p. 2050. DOI: 10.21105/joss.02050. URL: https://doi.org/10.21105/joss.02050.

[2] Ahmed M Balakhder, Mohammad M Al-Khaldi, and Joel T Johnson. “On the coherency of ocean and land surface specular scattering for GNSS-R and signals of opportunity systems”. In: *IEEE Transactions on Geoscience and Remote Sensing* 57.12 (2019), pp. 10426–10436.

[3] Adrian J. Brown et al. “Louth crater: Evolution of a layered water ice mound”. In: *Icarus* 196.2 (2008). Mars Polar Science IV, pp. 433–445. ISSN: 0019-1035. DOI: https://doi.org/10.1016/j.icarus.2007.11.023. URL: https://www.sciencedirect.com/science/article/pii/S0019103507005969.

[4] Hugo Carreno-Luengo, Guido Luzi, and Michele Crosetto. “Sensitivity of CyGNSS bistatic reflectivity and SMAP microwave radiometry brightness temperature to geophysical parameters over land surfaces”. In: *IEEE Journal of Selected Topics in Applied Earth Observations and Remote Sensing* 12.1 (2018), pp. 107–122.

[5] Luigi Castaldo et al. “Global permittivity mapping of the Martian surface from SHARAD”. In: *Earth and Planetary Science Letters* 462 (2017), pp. 55–65.

[6] Maria Paola Clarizia. “Investigating the effect of ocean waves on GNSS-R microwave remote sensing measurements”. PhD thesis. University of Southampton, 2012.

[7] Maria Paola Clarizia and Christopher S Ruf. “On the spatial resolution of GNSS reflectometry”. In: *IEEE Geoscience and Remote Sensing Letters* 13.8 (2016), pp. 1064–1068.

[8] Rodrigo Moreno Cordón, Luis Javier Serrano Arriezu, and Patrizia Savi. “GNSS-R systems for soil parameters determination”. 2018.

[9] Roger D De Roo and Fawwaz T Ulaby. “Bistatic specular scattering from rough dielectric surfaces”. In: *IEEE Transactions on Antennas and Propagation* 42.2 (2002), pp. 220–231.

[10] Andreas Dielacher, Heinrich Fragner, and Otto Koudelka. “PRETTY–passive GNSS-Reflectometry for CubeSats”. In: *e & i Elektrotechnik und Informationstechnik* 139.1 (2022), pp. 25–32.

[11] Alejandro Egido. “GNSS reflectometry for land remote sensing applications”. PhD thesis. Polytechnic University of Catalonia, Spain, 2013.

[12] TanoS Elfouhaily, Donald R Thompson, and Lloyd Linstrom. “Delay-Doppler analysis of bistatically reflected signals from the ocean surface: Theory and application”. In: *IEEE Transactions on Geoscience and Remote Sensing* 40.3 (2002), pp. 560–573.

[13] ESA. *True-colour image of Mars seen by OSIRIS*. Feb. 2007. URL: https://www.esa.int/ESA_Multimedia/Images/2007/02/True-colour_image_of_Mars_seen_by_OSIRIS (visited on 02/08/2026).

[14] European Space Agency. *ESA’s HydroGNSS mission launched to ‘scout’ for water*. [Accessed 01-12-2025]. Nov. 28, 2025. URL: https://www.esa.int/Applications/Observing_the_Earth/FutureEO/HydroGNSS/ESA_s_HydroGNSS_mission_launched_to_scout_for_water.

[15] Fran Fabra. “GNSS-R as a source of opportunity for remote sensing of the cryosphere”. In: *Universitat Politècnica de Catalunya* (2013).

[16] GIS Resources. *What is GNSS Reflectometry? How Does GNSS Reflectometry Work? Understanding Its Principles and Applications*. [Accessed 08-12-2025]. Sept. 2, 2024. URL: https://gisresources.com/what-is-gnss-reflectometry-how-does-gnss-reflectometry-workunderstanding-its-principles-and-applications/.

[17] Cyril Grima et al. “Investigating the Martian Surface at Decametric Scale: Population, Distribution, and Dimension of Heterogeneity from Radar Statistics”. In: *The Planetary Science Journal* 3.10 (Oct. 2022), p. 236. DOI: 10.3847/PSJ/ac9277. URL: https://doi.org/10.3847/PSJ/ac9277.

[18] H. M. Gunnarsdottir et al. “Root-mean-square surface slopes of Phoenix landing sites with 75-cm bistatic radar received by Mars Odyssey”. In: *Journal of Geophysical Research: Planets* 113.E3 (2008). DOI: https://doi.org/10.1029/2007JE003040. eprint: https://agupubs.onlinelibrary.wiley.com/doi/pdf/10.1029/2007JE003040. URL: https://agupubs.onlinelibrary.wiley.com/doi/abs/10.1029/2007JE003040.

[19] Hrefna Marin Gunnarsdottir. “Modeling the Martian Surface using Bistatic Radar at High Incidence Angles”. PhD thesis. Stanford University, 2010.

[20] T. Hagfors. “Backscattering from an undulating surface with applications to radar returns from the Moon”. In: *Journal of Geophysical Research* 69.18 (1964), pp. 3779–3784.

[21] Mark S. Haynes. “Surface and subsurface radar equations for radar sounders”. In: *Annals of Glaciology* 61.81 (2020), pp. 135–142. DOI: 10.1017/aog.2020.16.

[22] Patrik Hermansson, Göran Forssell, and Jan Fagerstrom. “A review of models for scattering from rough surfaces”. In: *Linköping: FOI-Swedish Defence Research Agency* (2003).

[23] Philip Jales. “Spaceborne receiver design for scatterometric GNSS reflectometry”. 2012.

[24] Ramakrishna Janaswamy. *Radiowave propagation and smart antennas for wireless communications*. Springer, 2002.

[25] Yan Jia and Yuekun Pei. “Remote sensing in land applications by using GNSS-reflectometry”. In: *Recent Advances and Applications in Remote Sensing* (2018).

[26] Shuanggen Jin et al. “Remote sensing and its applications using GNSS reflected signals: Advances and prospects”. In: *Satellite Navigation* 5.1 (2024), p. 19.

[27] Kevin Kelly and Bojan Šavrič. “Area and volume computation of longitude–latitude grids and three-dimensional meshes”. In: *Transactions in GIS* 25.1 (2021), pp. 6–24. DOI: https://doi.org/10.1111/tgis.12636. eprint: https://onlinelibrary.wiley.com/doi/pdf/10.1111/tgis.12636. URL: https://onlinelibrary.wiley.com/doi/abs/10.1111/tgis.12636.

[28] Mehmet Kurum et al. “SCoBi-Veg: A generalized bistatic scattering model of reflectometry from vegetation for signals of opportunity applications”. In: *IEEE Transactions on Geoscience and Remote Sensing* 57.2 (2018), pp. 1049–1068.

[29] Eric Loria et al. “Analysis of scattering characteristics from inland bodies of water observed by CYGNSS”. In: *Remote Sensing of Environment* 245 (2020), p. 111825.

[30] Juan Fernando Marchán Hernandez et al. “Sea state determnation using GNSS-R techniques: contributions to the pau instrument”. 2009.

[31] Juan Fernando Marchán-Hernández et al. “An efficient algorithm to the simulation of delay–Doppler maps of reflected global navigation satellite system signals”. In: *IEEE Transactions on Geoscience and Remote Sensing* 47.8 (2009), pp. 2733–2740.

[32] NASA Navigation and Ancillary Information Facility. *SPICE: Observation Geometry System for Space Science Missions*. Astrophysics Source Code Library, record ascl:1903.015. Mar. 2019. ascl: 1903.015.

[33] Navigation and Ancillary Information Facility. *An Overview of SPICE. NASA’s Observation Geometry System for Space Science Missions*. https://naif.jpl.nasa.gov/pub/naif/toolkit_docs/Tutorials/pdf/individual_docs/03_spice_overview.pdf. Accessed: 2026-01-15. Apr. 2023.

[34] Navigation and Ancillary Information Facility. *Geometry Finder Required Reading*. https://naif.jpl.nasa.gov/pub/naif/misc/toolkit_docs_N0067/C/req/gf.html. Accessed: 2026-01-27. June 2017.

[35] D.J. Nieuwenhuizen. “Probing shallow subsurface water on Mars through bi-static radar measurements at UHF wavelengths”. 2025.

[36] Richard A. Simpson et al. “Polarization in Bistatic Radar Probing of Planetary Surfaces: Application to Mars Express Data”. In: *Proceedings of the IEEE* 99.5 (2011), pp. 858–877.

[37] SkywalkerPL. *File:ExoMars TGO size vs Mars Express.svg*. Mar. 2016. URL: https://commons.wikimedia.org/wiki/File:ExoMars_TGO_size_vs_Mars_Express.svg (visited on 02/08/2026).

[38] Alan D. Snow et al. *pyproj4/pyproj: 3.7.2 Release*. Version 3.7.2. Aug. 2025. DOI: 10.5281/zenodo.16874869. URL: https://doi.org/10.5281/zenodo.16874869.

[39] Minfeng Song et al. “Investigation on Geometry Computation of Spaceborne GNSS-R Altimetry over Topography: Modeling and Validation”. In: *Remote Sensing* 14.9 (2022). ISSN: 2072-4292. DOI: 10.3390/rs14092105. URL: https://www.mdpi.com/2072-4292/14/9/2105.

[40] Ahmed K Sultan-Salem and G Leonard Tyler. “Hagfors’ law revisited”. In: *Journal of Geophysical Research: Planets* 111.E6 (2006).

[41] L.H Svedhem. Personal communication. [Supervisor Meeting]. May 2025.

[42] L.H Svedhem. Personal communication. [Dataset containg MEX and TGO co-polarization antenna gain pattern data]. June 2025.

[43] TGO team. *ExoMars TGO FDDB User Manual*. Thales Alenia Space. June 2016.

[44] USGS Astrogeology Science Center. *Mars Viking Global Color Mosaic 925m*. URL: https://astrogeology.usgs.gov/search/map/mars_viking_global_color_mosaic_925m (visited on 02/16/2025).

[45] Anne Virkki. “Numerical Evaluation of Planetary Radar Backscatter Models for Self-Affine Fractal Surfaces”. In: *Remote Sensing* 16.5 (2024). ISSN: 2072-4292. DOI: 10.3390/rs16050890. URL: https://www.mdpi.com/2072-4292/16/5/890.

[46] Alexander G Voronovich and Valery U Zavorotny. “Bistatic radar equation for signals of opportunity revisited”. In: *IEEE Transactions on Geoscience and Remote Sensing* 56.4 (2017), pp. 1959–1968.

[47] Yang Wang. “Evaluating GNSS-R measurements at very low elevation angles (< 8°) and their atmospheric applications based on Spire grazing-angle data”. In: *AGU Fall Meeting Abstracts*. Vol. 2023. AGU Fall Meeting Abstracts. Dec. 2023, IN34B-07, IN34B–07.

[48] S Wu et al. “The potential use of GPS signals as ocean altimetry observables”. In: *Proceedings of the National Technical Meeting-Institute of Navigation*. INSTITUTE OF NAVIGATION. 1997, pp. 543–550.

[49] Xuerui Wu et al. “Spaceborne GNSS-R Soil Moisture Retrieval: Status, Development Opportunities, and Challenges”. In: *Remote Sensing* 13.1 (2021). ISSN: 2072-4292. DOI: 10.3390/rs13010045. URL: https://www.mdpi.com/2072-4292/13/1/45.

[50] Changzhi Yang et al. “Review of GNSS-R Technology for Soil Moisture Inversion”. In: *Remote Sensing* 16.7 (2024). ISSN: 2072-4292. DOI: 10.3390/rs16071193. URL: https://www.mdpi.com/2072-4292/16/7/1193.

[51] Kegen Yu, Chris Rizos, and Andrew G Dempster. “GNSS-based model-free sea surface height estimation in unknown sea state scenarios”. In: *IEEE Journal of Selected Topics in Applied Earth Observations and Remote Sensing* 7.5 (2013), pp. 1424–1435.

[52] Valery U Zavorotny and Alexander G Voronovich. “Scattering of GPS signals from the ocean with wind remote sensing application”. In: *IEEE Transactions on Geoscience and Remote Sensing* 38.2 (2002), pp. 951–964.

[53] Valery U Zavorotny et al. “Tutorial on remote sensing using GNSS bistatic radar of opportunity”. In: *IEEE Geoscience and Remote Sensing Magazine* 2.4 (2015), pp. 8–45.

A

Derivations

A.1. Divergence factors derivation

For a spherically curved planet surface, the first Fresnel zone is approximated by an ellipse with semi-major and semi-minor axes F_{1x} and F_{1y} which can be calculated through a set of equations that also introduce the D_x and D_y divergence factors [2]:

$$F_1 = \sqrt{\frac{\lambda R_t R_r}{R_t + R_r}} \tag{A.1}$$

$$D_x = \sqrt{1 + \frac{2F_1}{a_{\text{eff}}} \frac{F_1}{\lambda \cos(\theta)}} \tag{A.2}$$

$$D_y = \sqrt{1 + \frac{2F_1}{a_{\text{eff}}} \frac{F_1 \cos(\theta)}{\lambda}} \tag{A.3}$$

$$F_{1x} = \frac{F_1}{D_x \cos(\theta)} \tag{A.4}$$

$$F_{1y} = \frac{F_1}{D_y} \tag{A.5}$$

where a_{eff} is the planet's radius of curvature at the specular point.

B

Additional measurement simulation figures

This appendix contains several additional measurement simulation figures. Appendix B.1 contains figures with several model parameters, including TX and RX distances, reflectivity, incidence angles, required tilt angle, off-boresight angles, C parameter (Hagfors' model) and topography scaling factor (as defined by Nieuwenhuizen [35]). Appendix B.2 contains figures showing the RX antenna co- and cross-polarization components of the reflected power.

B.1. Measurement simulation model parameters figures

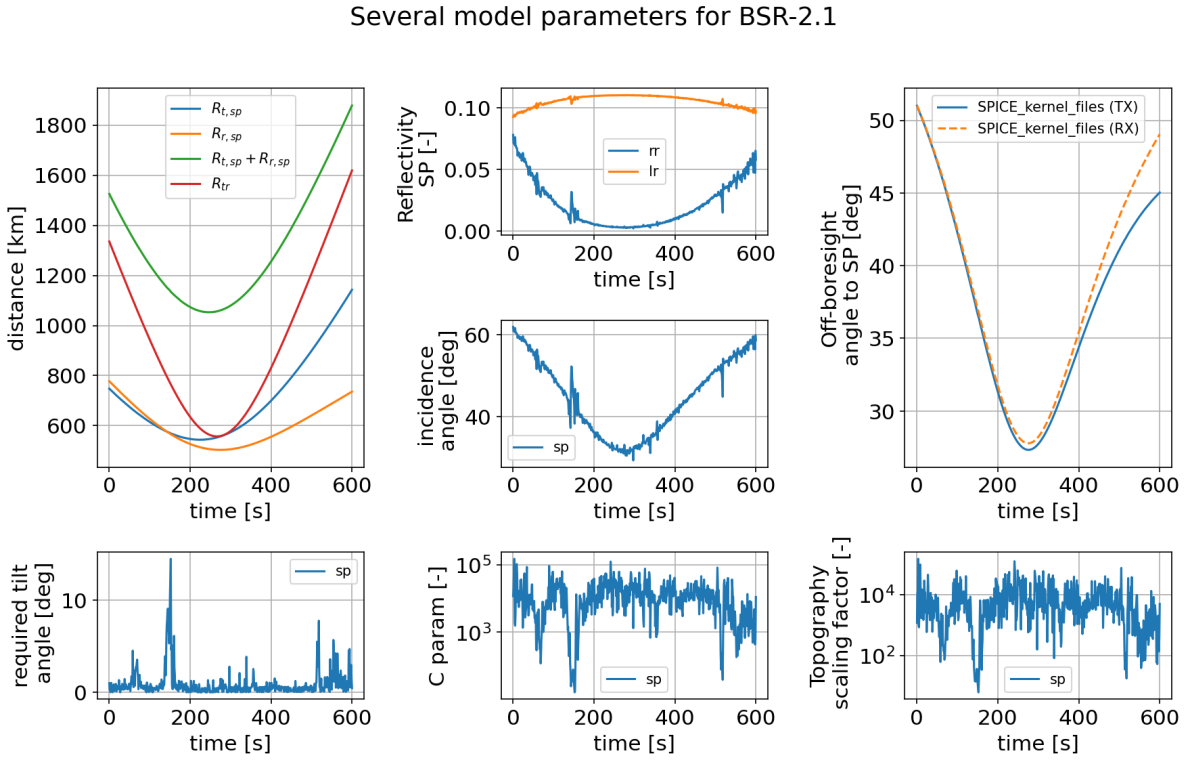

Figure B.1: Several model parameter plots for BSR-2.1

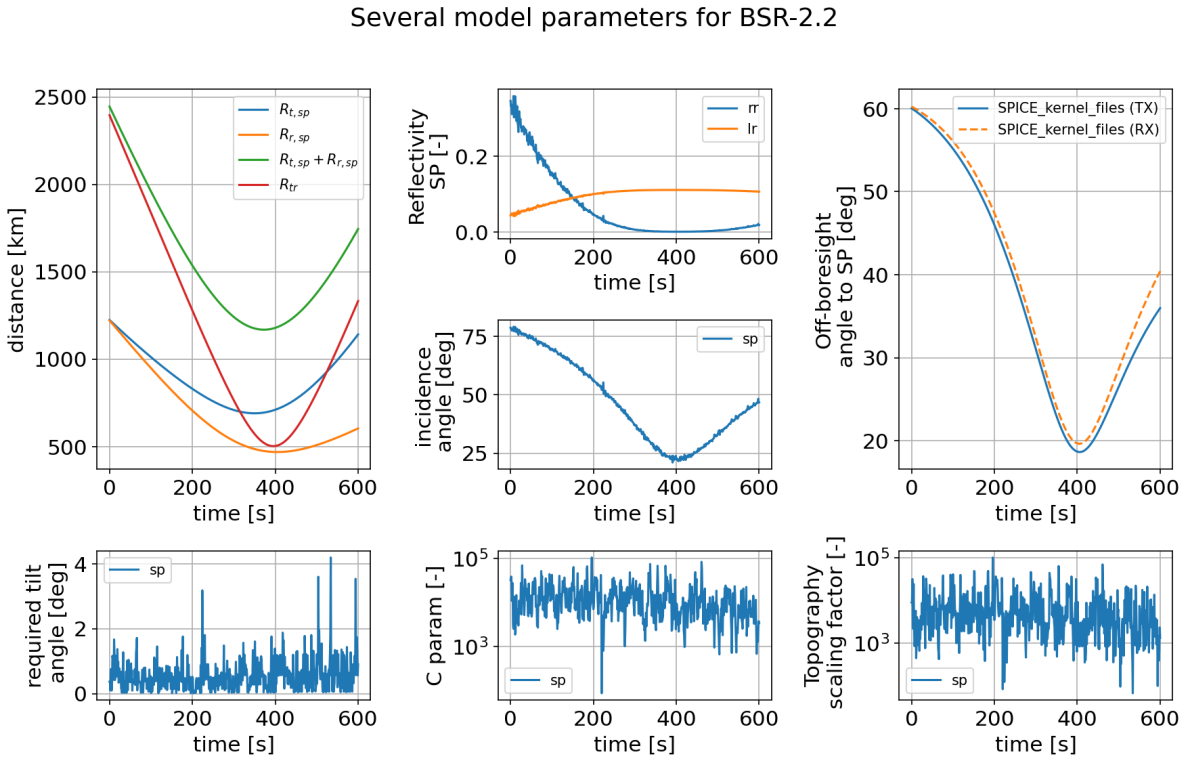

Figure B.2: Several model parameter plots for BSR-2.2

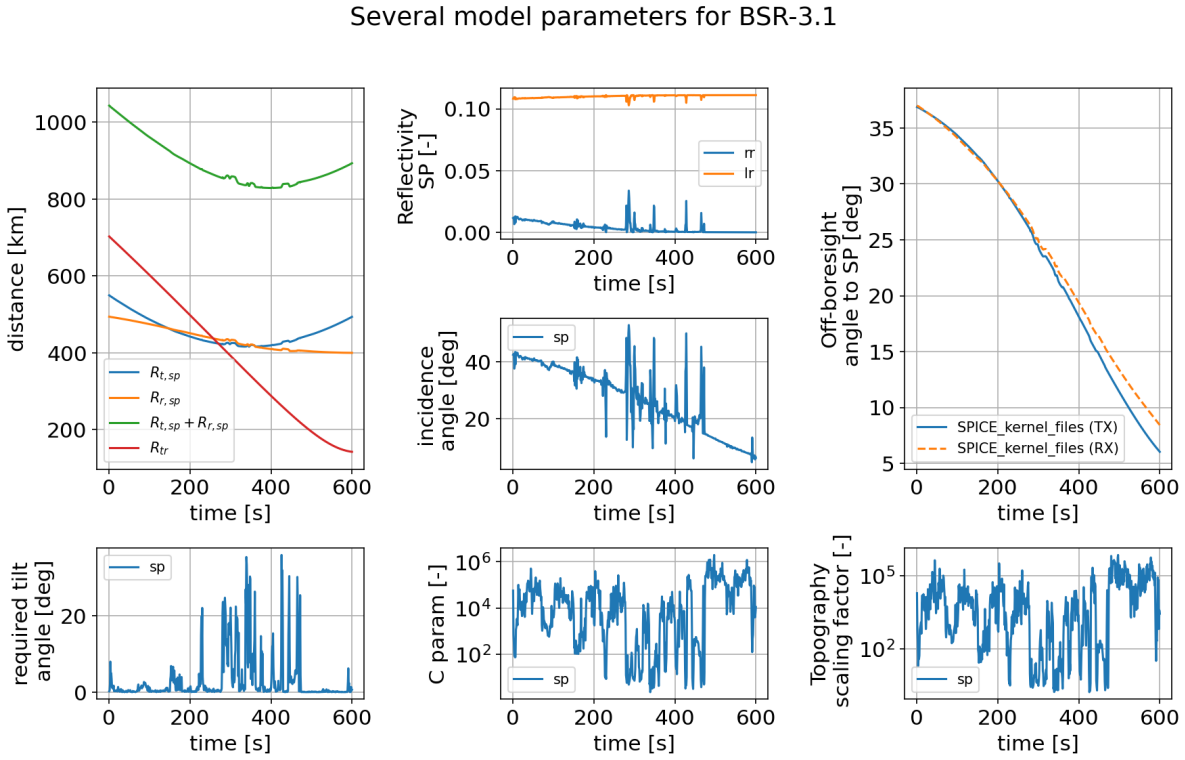

Figure B.3: Several model parameter plots for BSR-3.1

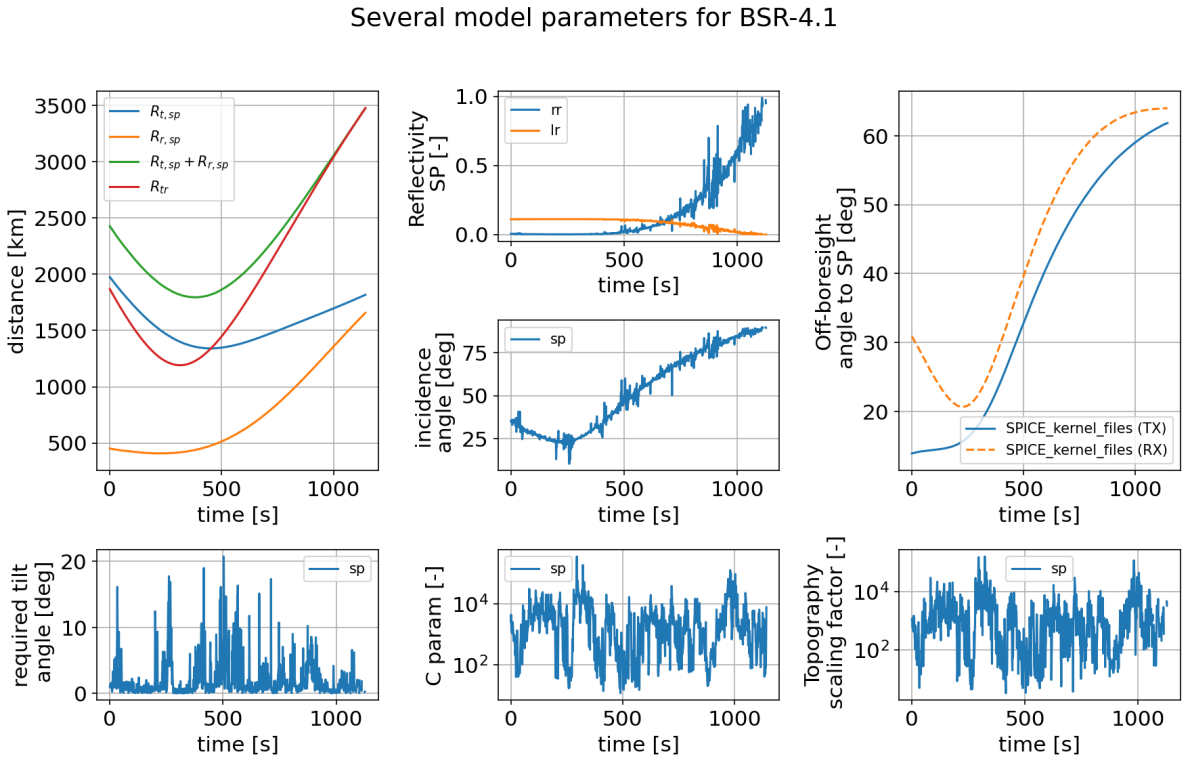

Figure B.4: Several model parameter plots for BSR-4.1

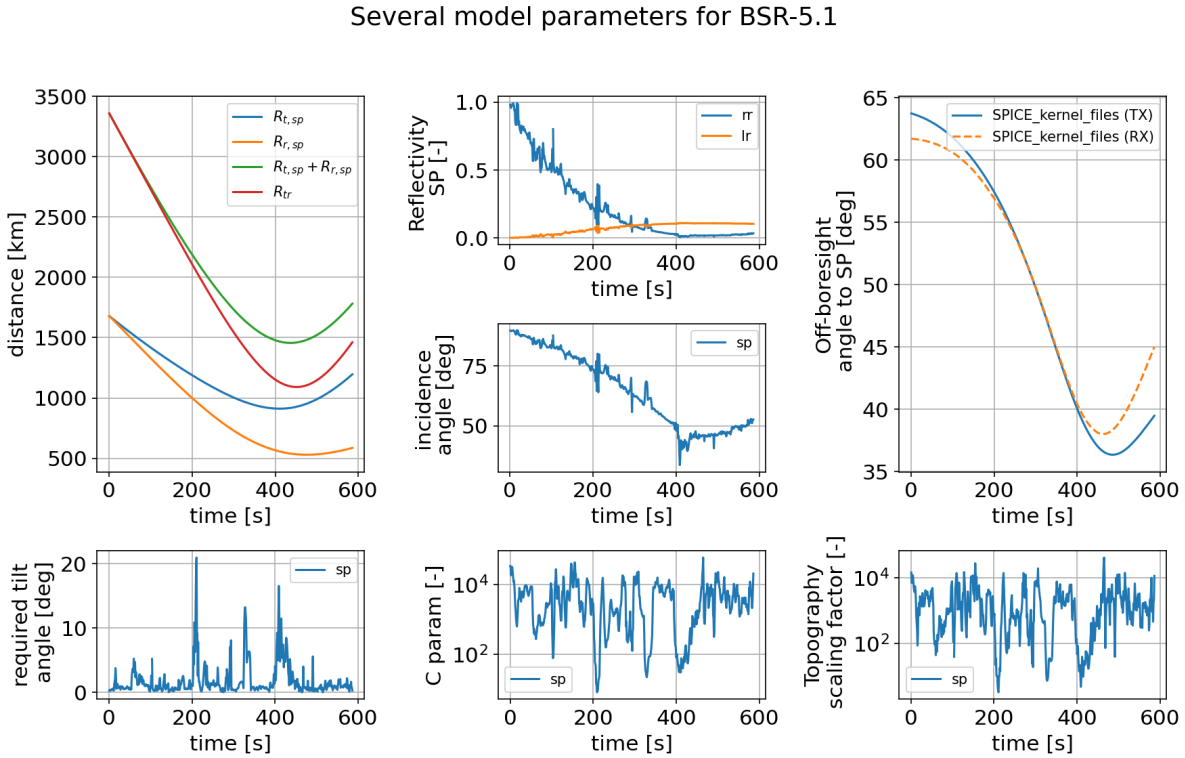

Figure B.5: Several model parameter plots for BSR-5.1

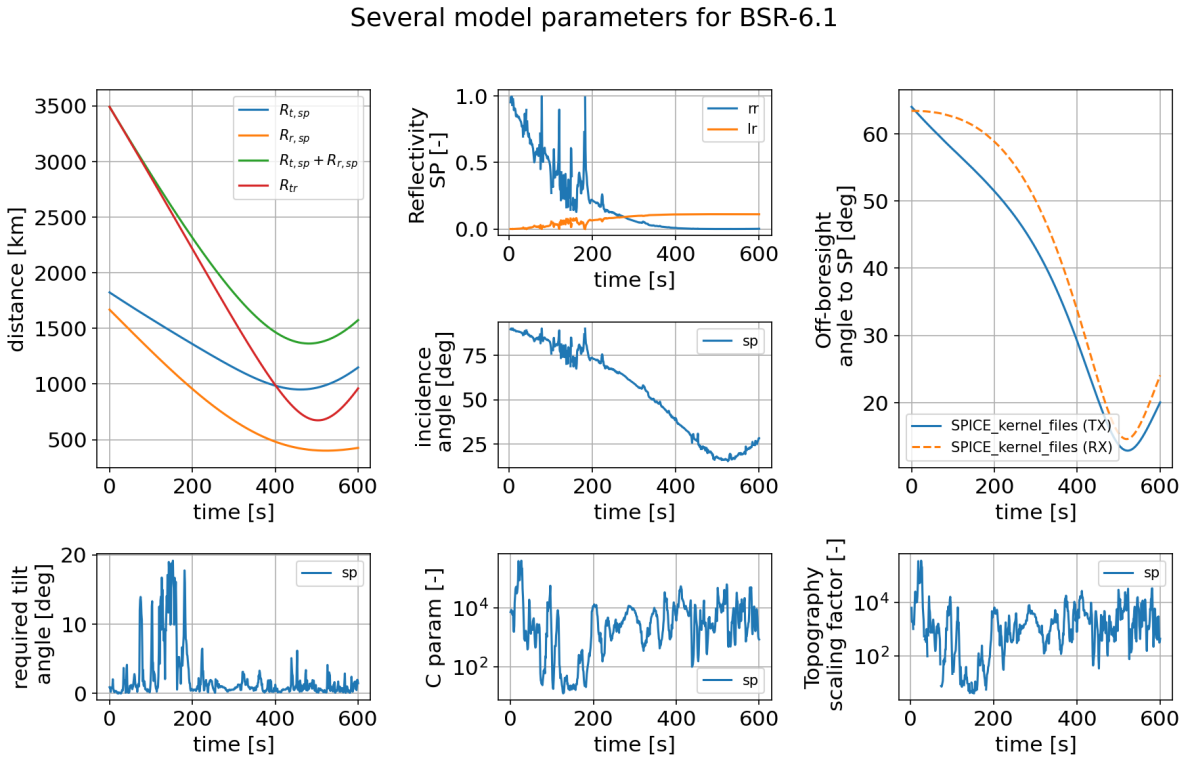

Figure B.6: Several model parameter plots for BSR-6.1

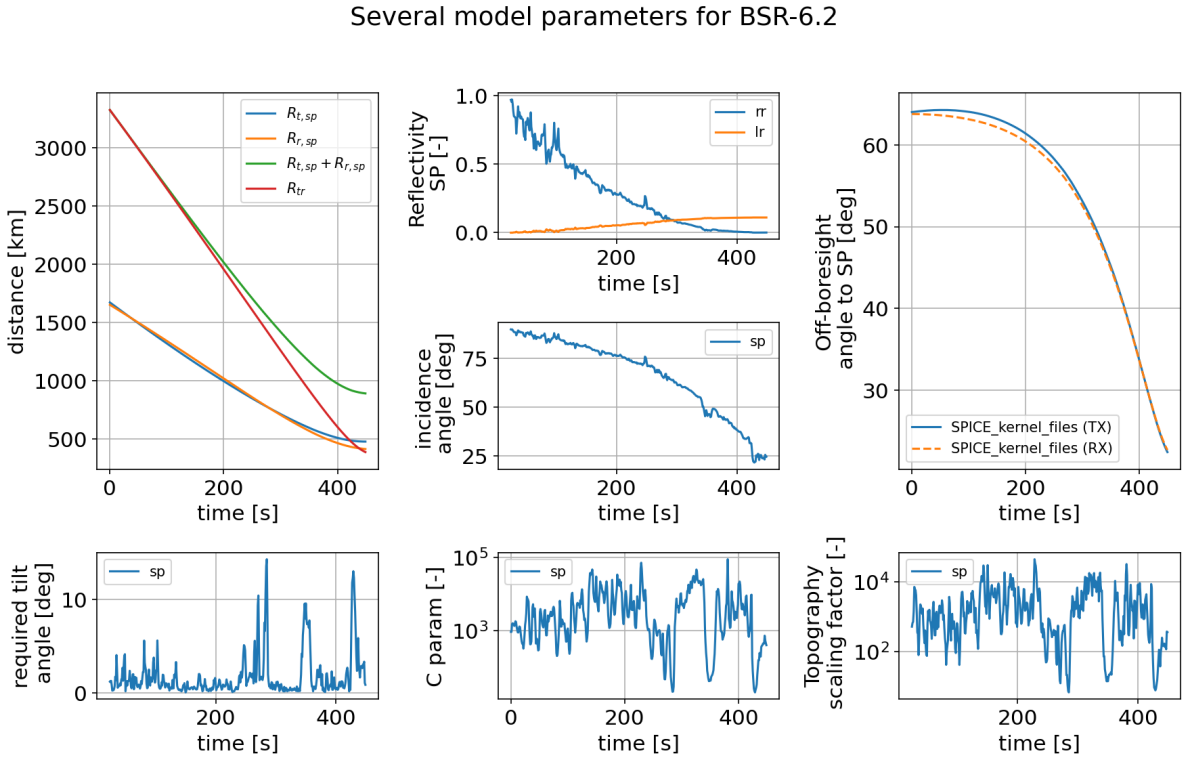

Figure B.7: Several model parameter plots for BSR-6.2

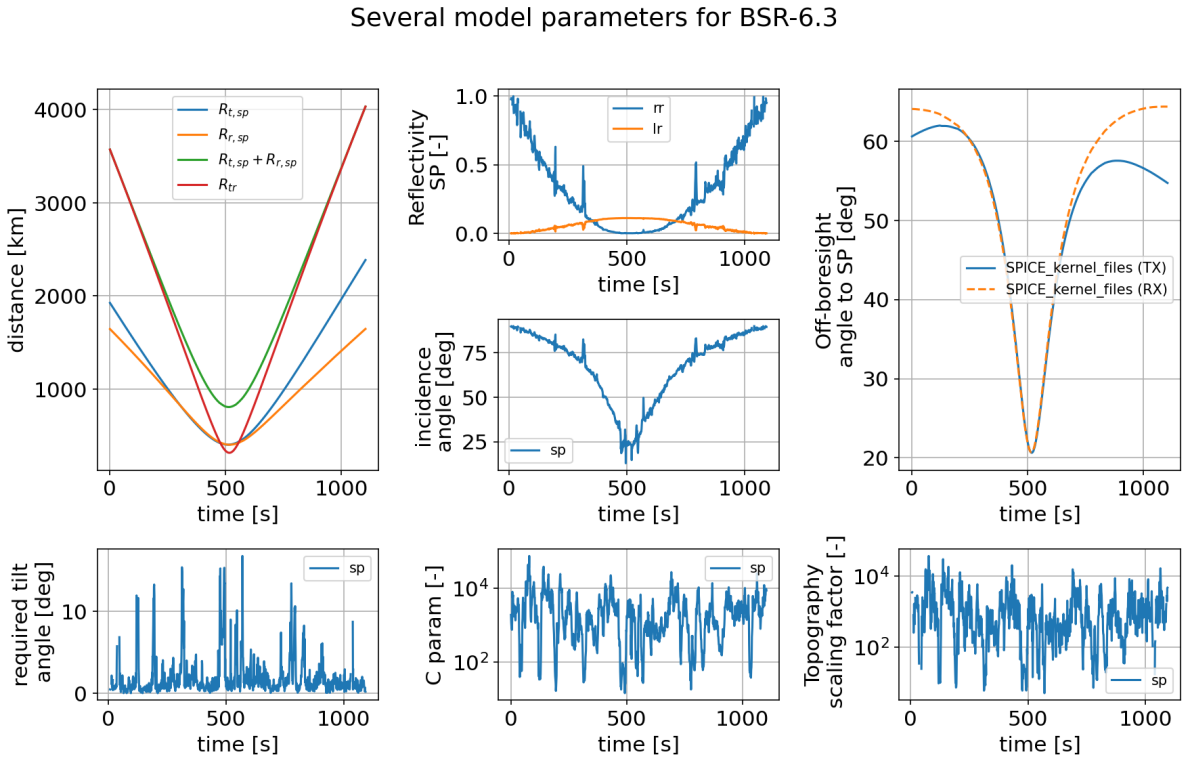

Figure B.8: Several model parameter plots for BSR-6.3

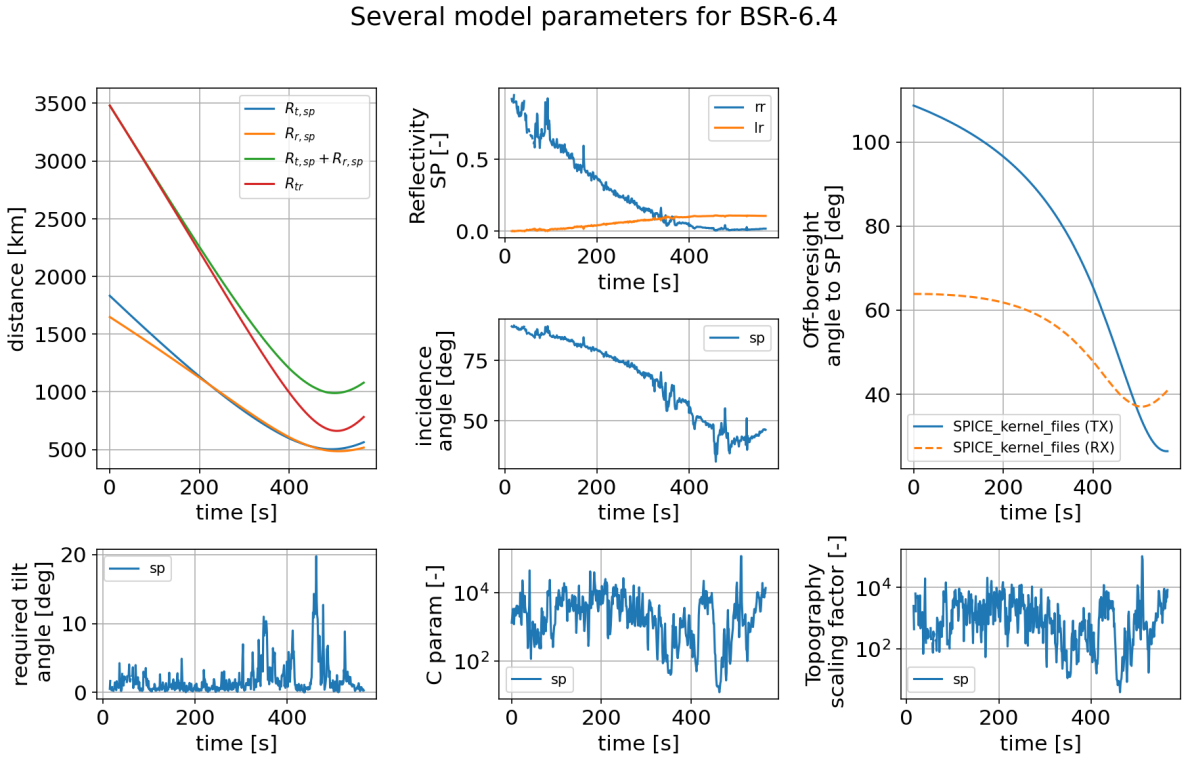

Figure B.9: Several model parameter plots for BSR-6.4

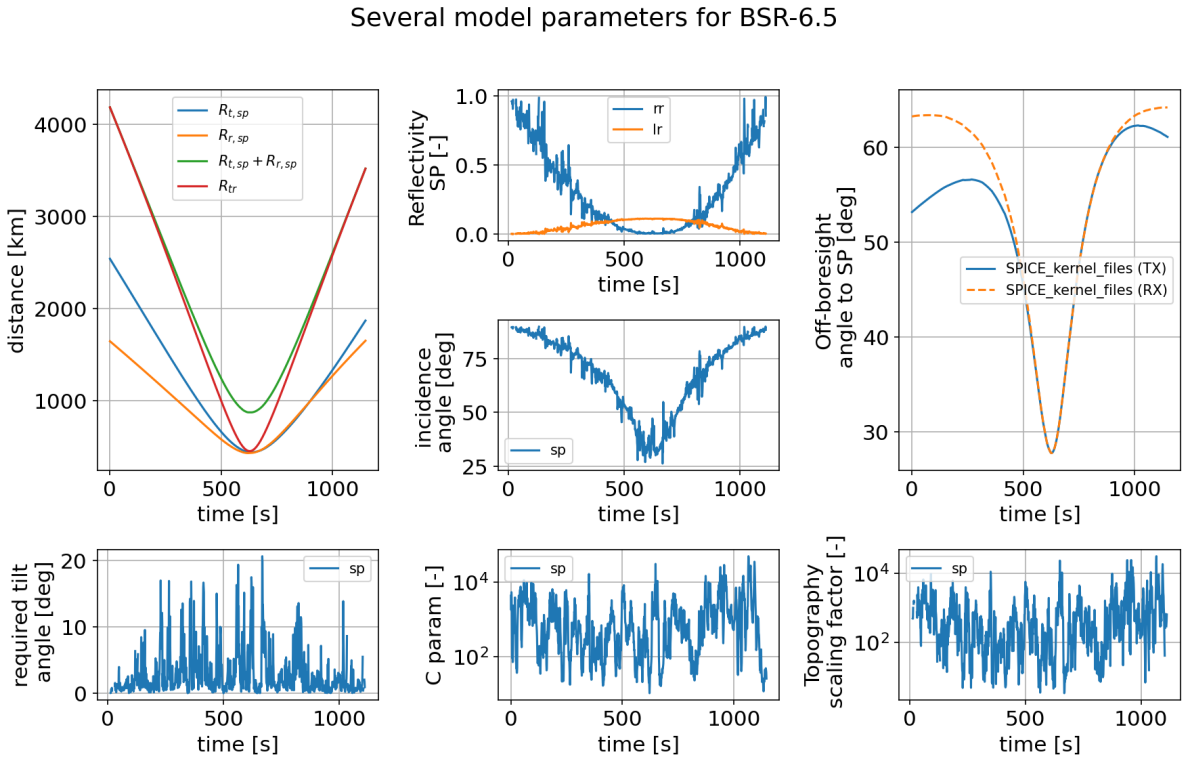

Figure B.10: Several model parameter plots for BSR-6.5

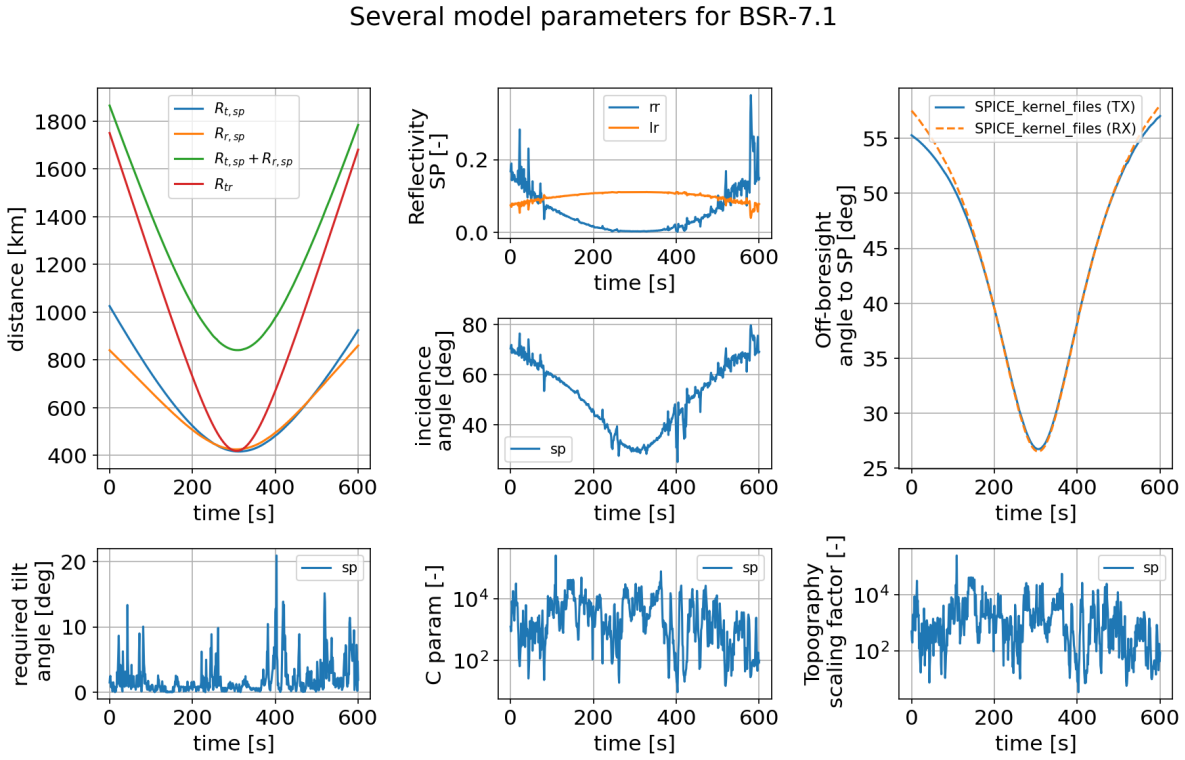

Figure B.11: Several model parameter plots for BSR-7.1

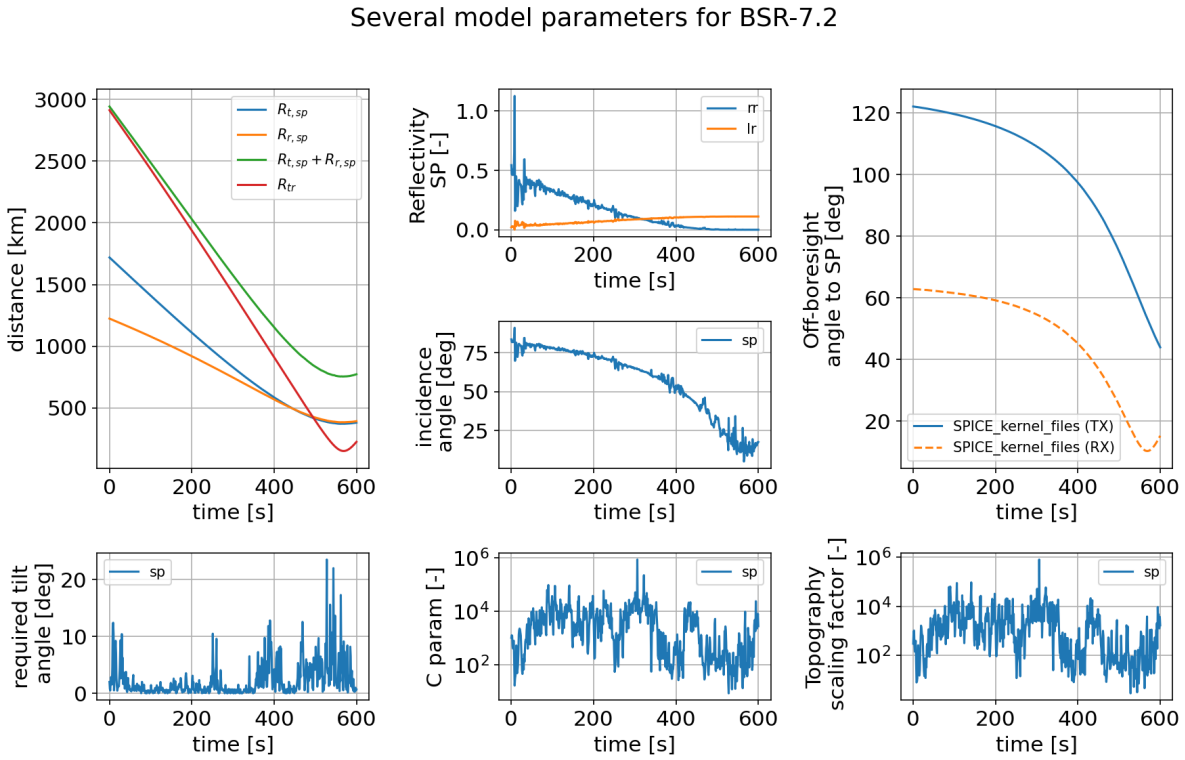

Figure B.12: Several model parameter plots for BSR-7.2

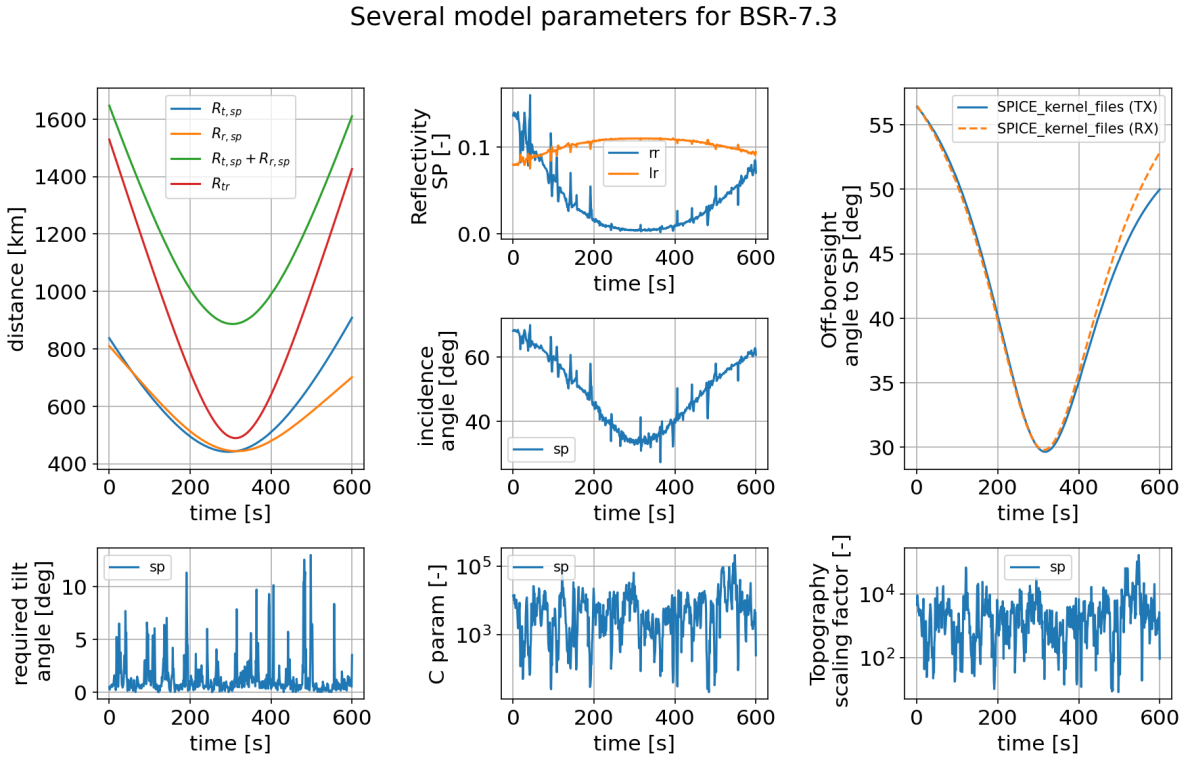

Figure B.13: Several model parameter plots for BSR-7.3

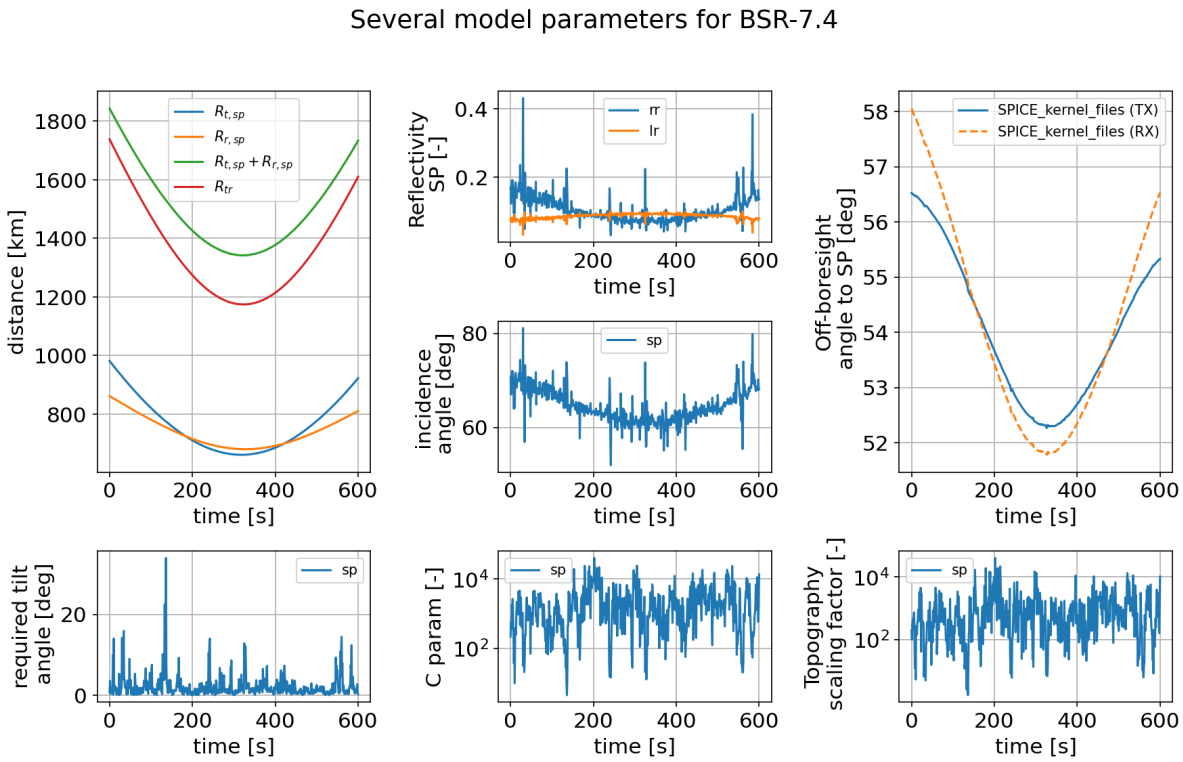

Figure B.14: Several model parameter plots for BSR-7.4

B.2. Measurement simulation polarization figures

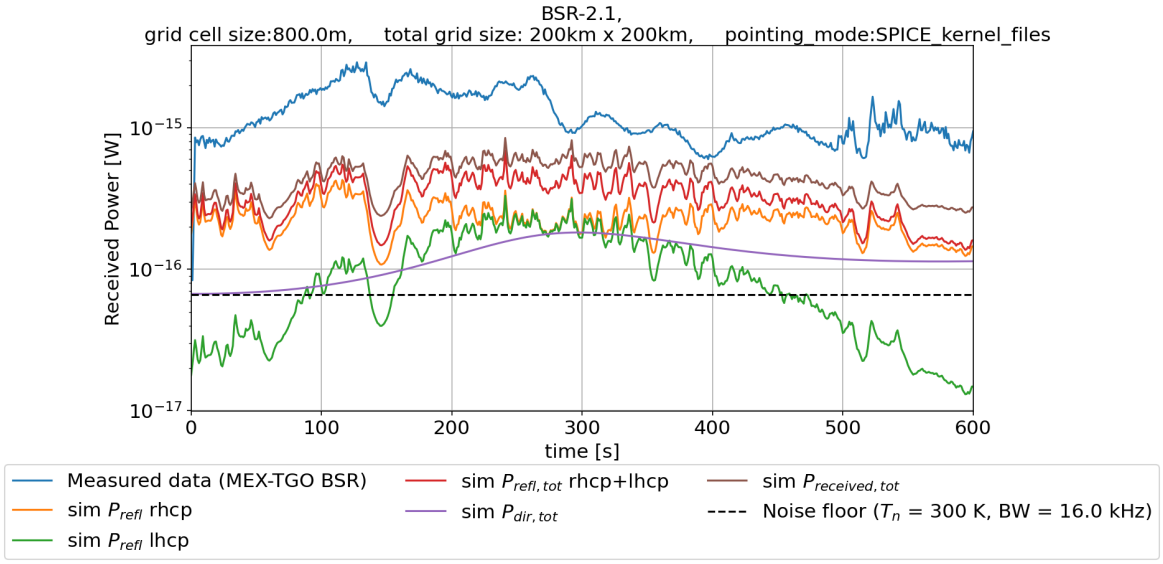

Figure B.15: Received power results for co-pol and x-pol receiver antenna polarizations for BSR-2.1

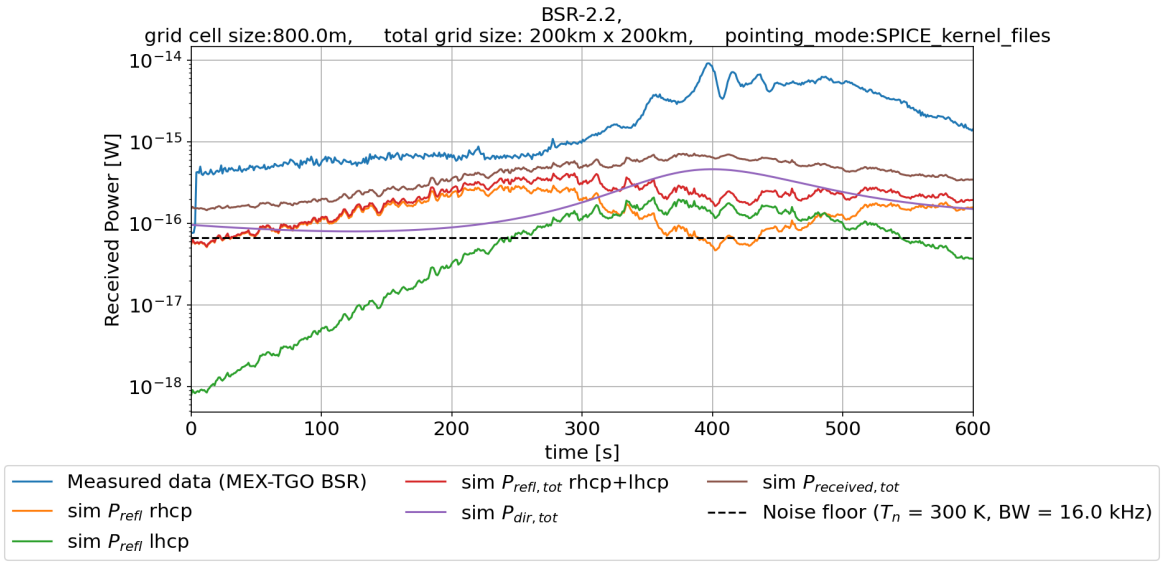

Figure B.16: Received power results for co-pol and x-pol receiver antenna polarizations for BSR-2.2

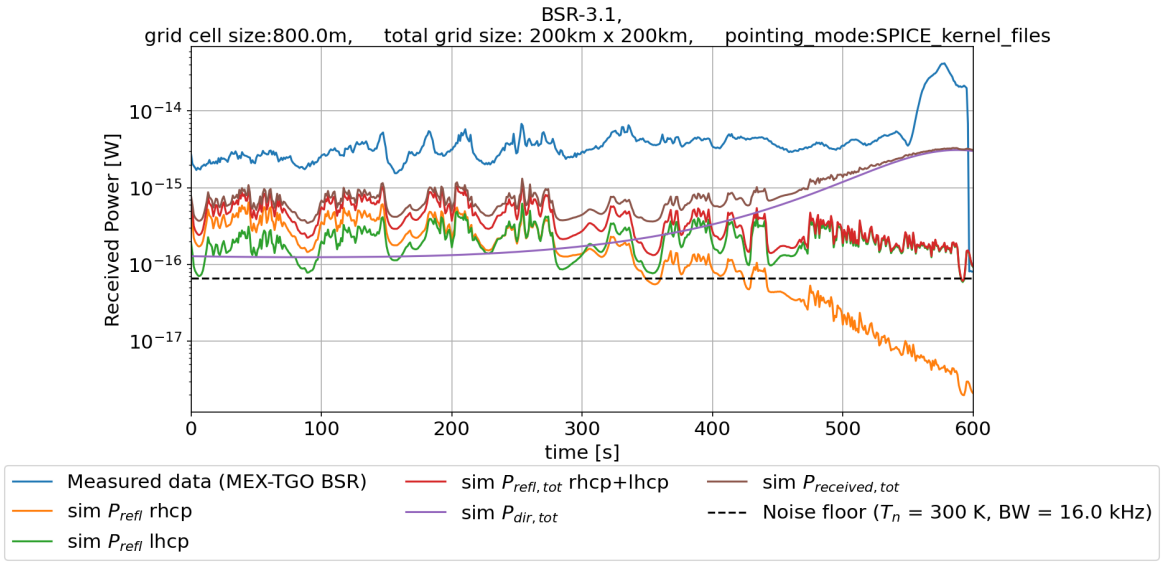

Figure B.17: Received power results for co-pol and x-pol receiver antenna polarizations for BSR-3.1

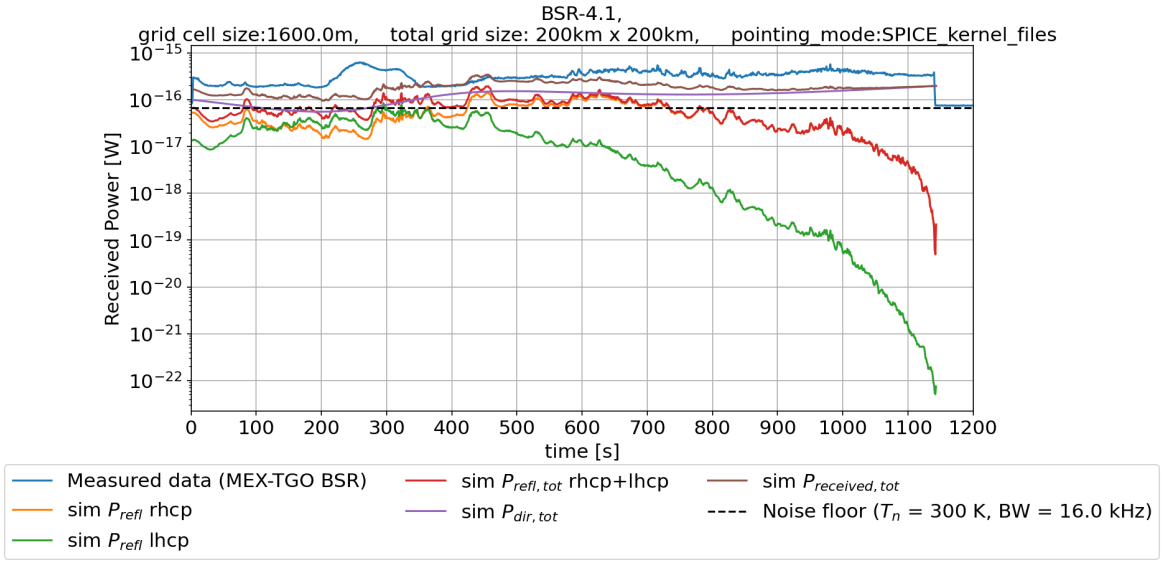

Figure B.18: Received power results for co-pol and x-pol receiver antenna polarizations for BSR-4.1

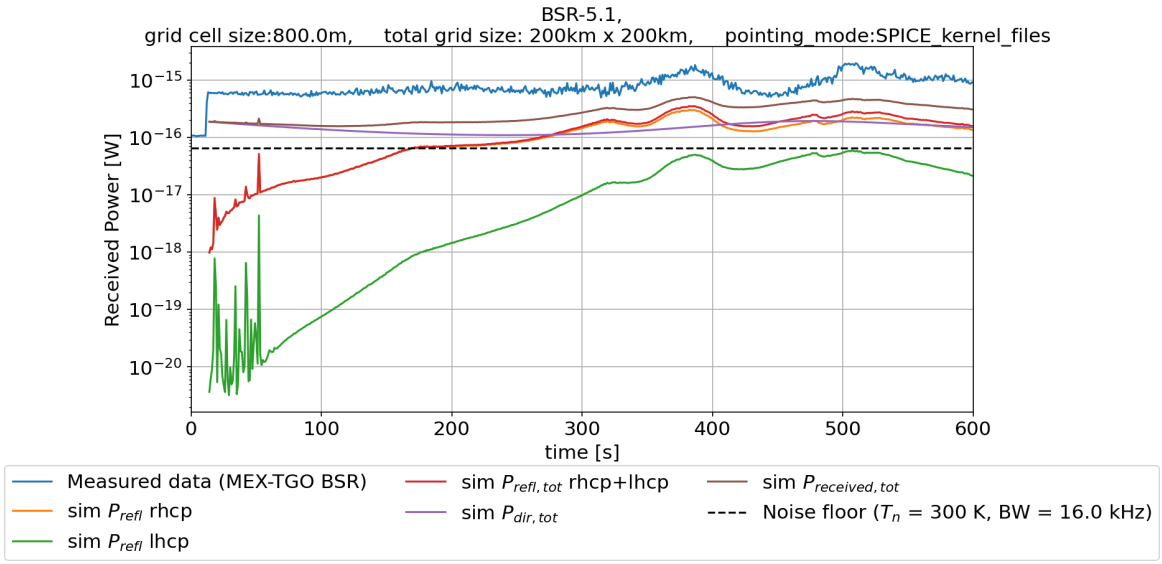

Figure B.19: Received power results for co-pol and x-pol receiver antenna polarizations for BSR-5.1

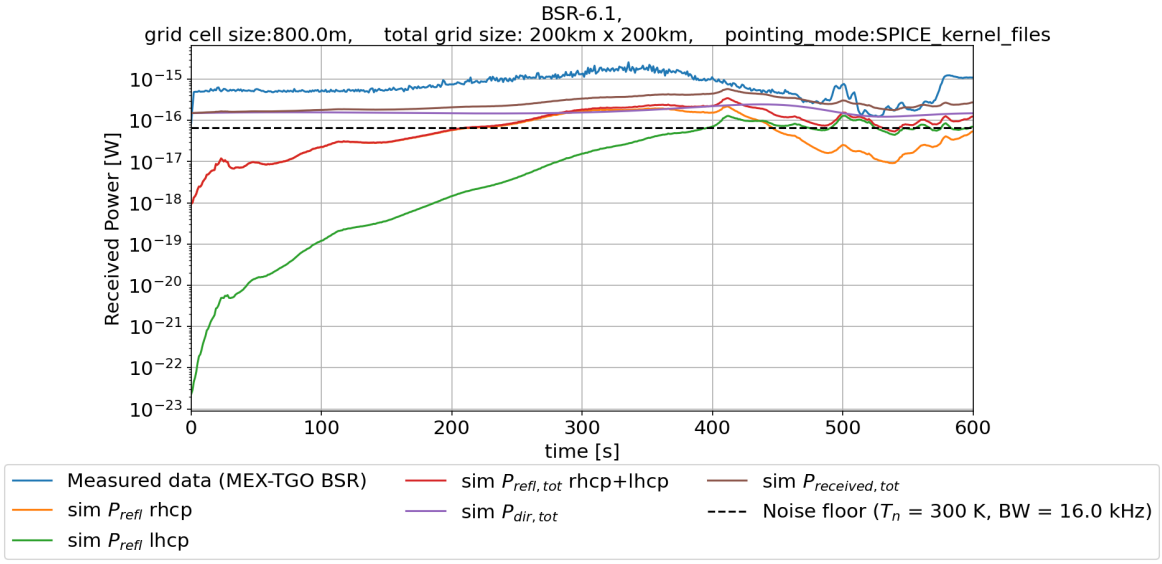

Figure B.20: Received power results for co-pol and x-pol receiver antenna polarizations for BSR-6.1

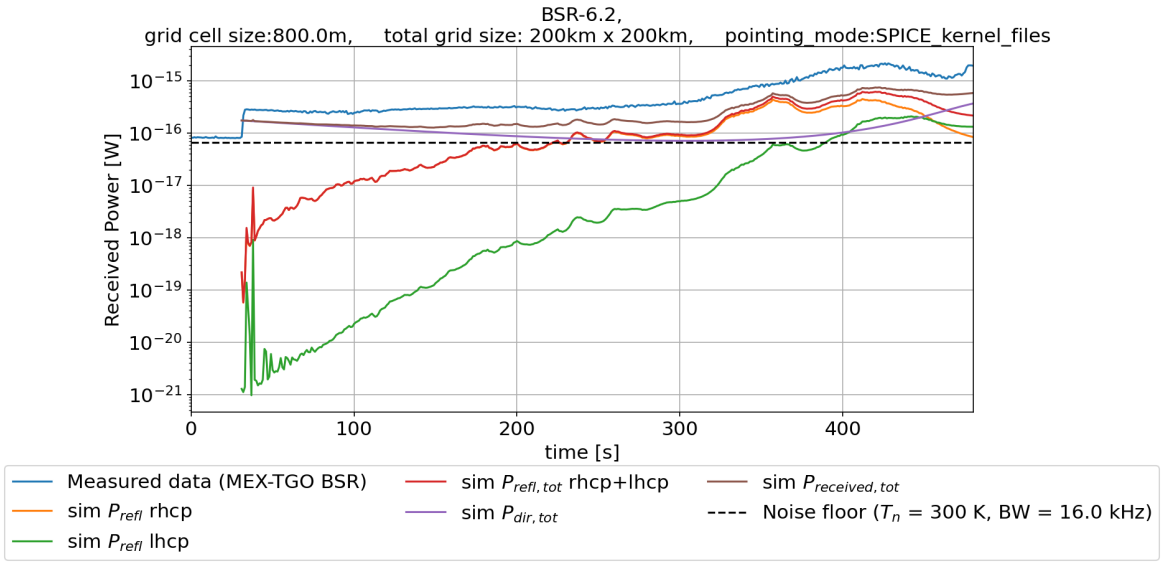

Figure B.21: Received power results for co-pol and x-pol receiver antenna polarizations for BSR-6.2

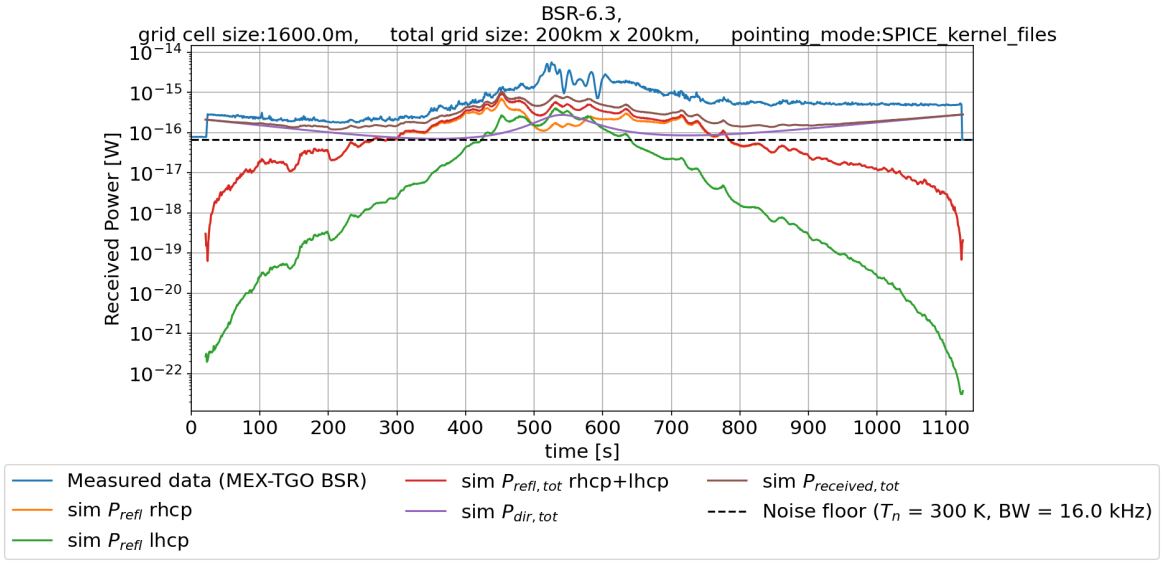

Figure B.22: Received power results for co-pol and x-pol receiver antenna polarizations for BSR-6.3

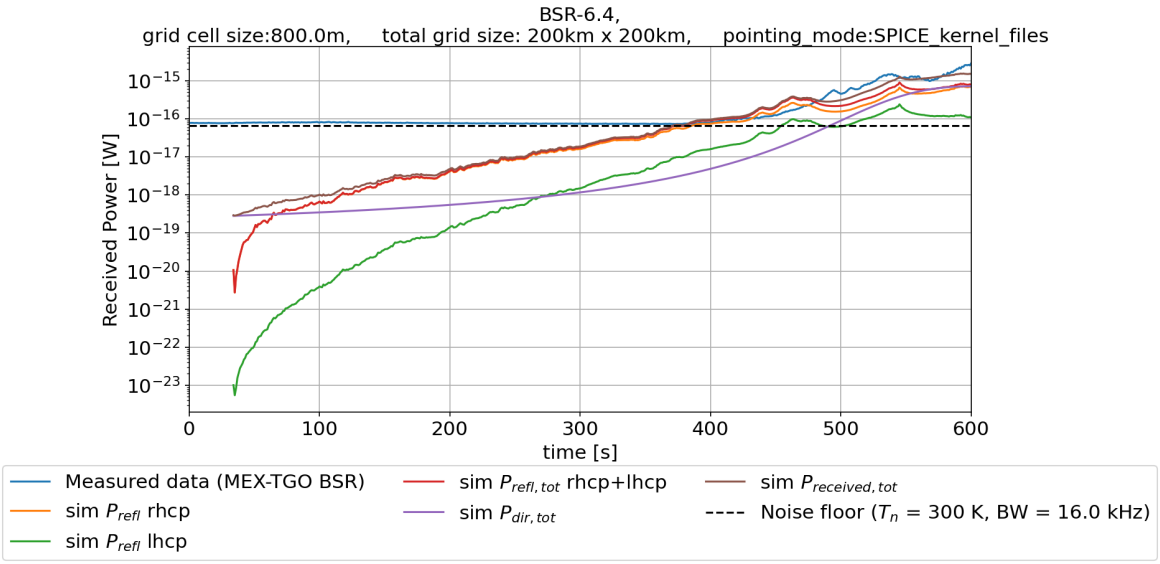

Figure B.23: Received power results for co-pol and x-pol receiver antenna polarizations for BSR-6.4

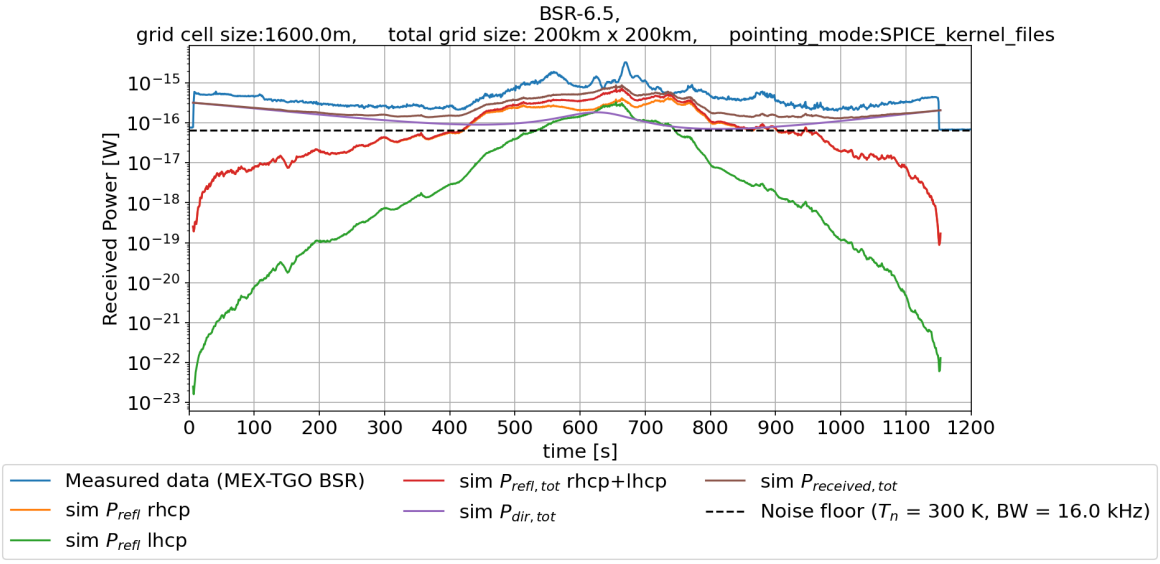

Figure B.24: Received power results for co-pol and x-pol receiver antenna polarizations for BSR-6.5

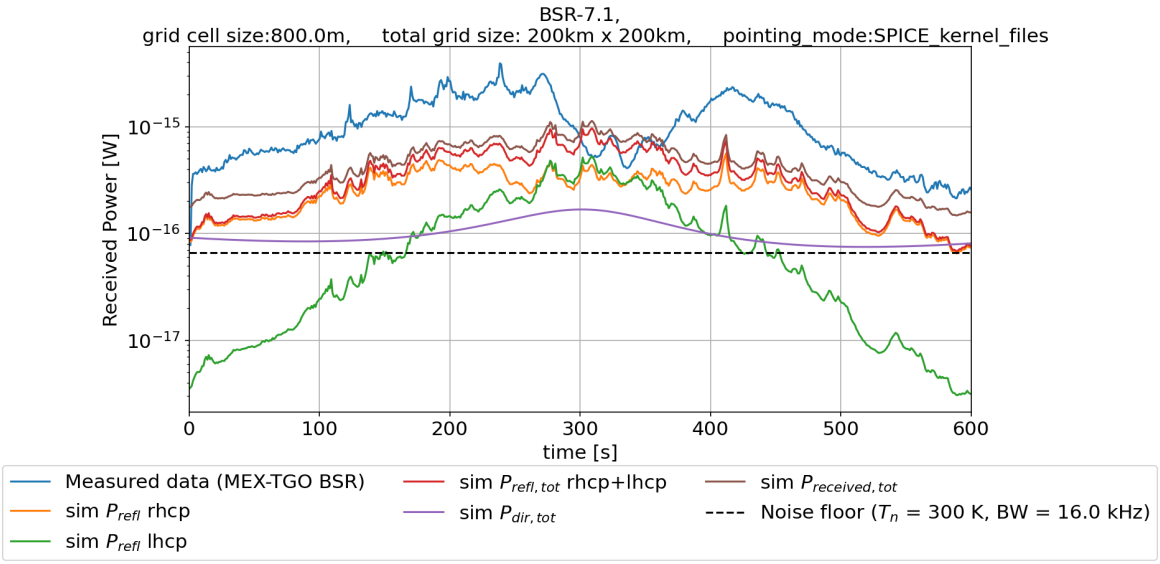

Figure B.25: Received power results for co-pol and x-pol receiver antenna polarizations for BSR-7.1

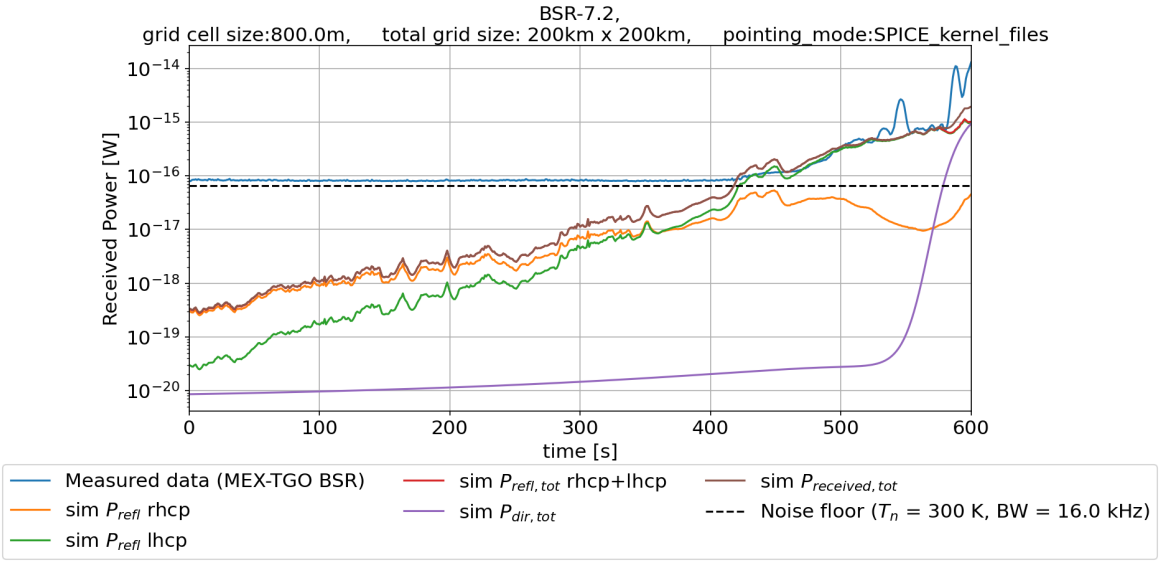

Figure B.26: Received power results for co-pol and x-pol receiver antenna polarizations for BSR-7.2

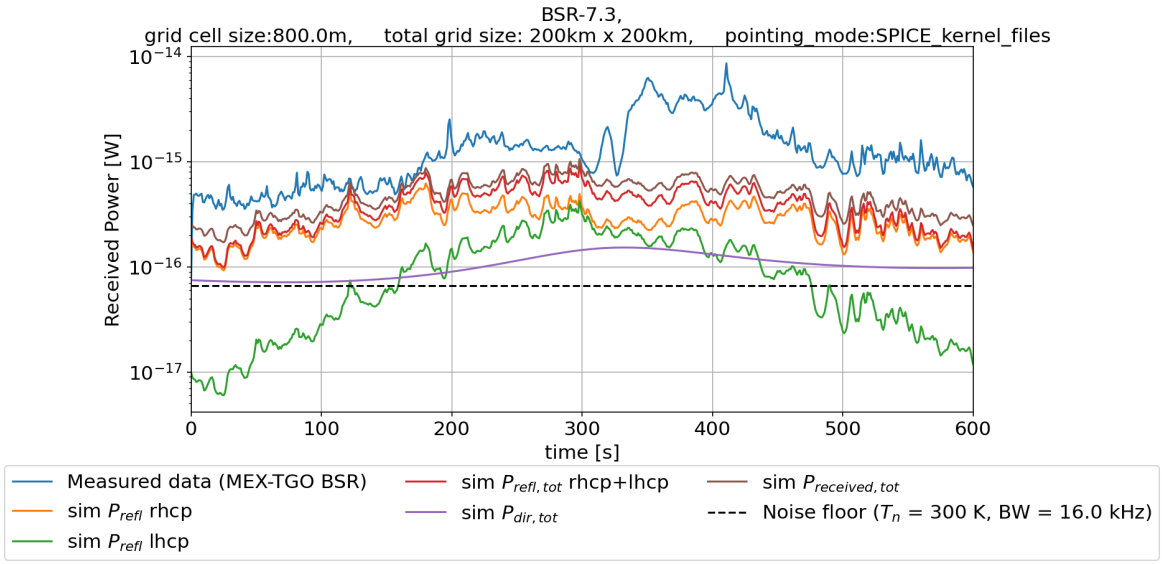

Figure B.27: Received power results for co-pol and x-pol receiver antenna polarizations for BSR-7.3

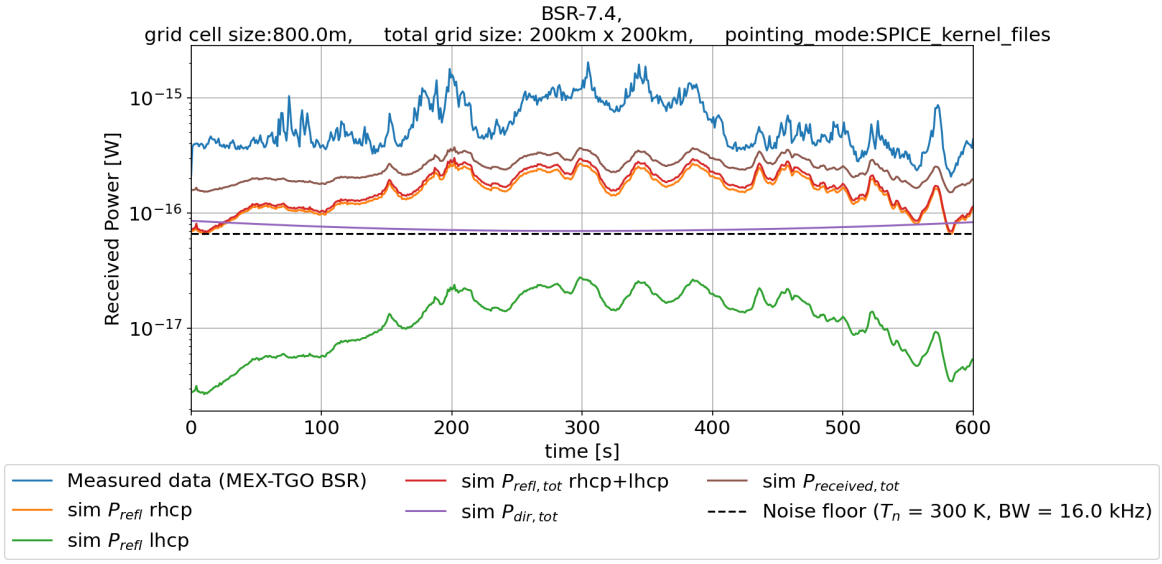

Figure B.28: Received power results for co-pol and x-pol receiver antenna polarizations for BSR-7.4

C

SPICE kernels

Here all the SPICE kernels used in the bistatic geometry search(/measurement planning) and bistatic measurement simulation are listed. These kernels were downloaded from the ESA SPICE service FTP server: `https://spiftp.esac.esa.int/data/SPICE/`. The kernels are divided into four categories:

- General_MetaKernel: Metakernel containing general planetary constants and ephemeris, time conversion, and Mars ephemeris related kernels.
- MEX_MetaKernel: Metakernel containing ephemeris and orientation related kernels for MEX.
- TGO_MetaKernel: Metakernel containing ephemeris and orientation related kernels for TGO.
- Tiled Mars MOLA DSK files: List of tiled Mars MOLA DSK files.

which can be found in appendices C.1 to C.4 respectively.

C.1. General_MetaKernel

This section lists the kernels loaded by the 'General_MetaKernel.tm' file.

- **Leap Second Kernels (LSKs)**:
  - naif0012.tls — *Generic leapseconds kernel.*
- **Planetary Constants Kernels (PCKs)**:
  - pck00011.tpc — *Generic Planetary Constants Kernel.*
- **Spacecraft and Planet Kernels (SPKs)**:
  - de442s.bsp — *Planetary ephemeris data for the Solar system.*
  - mar099s.bsp — *Mars Satellite Ephemeris, required for determination of the location of Mars' Center of Mass (499), which differs slightly from Mars' Barycenter (4).*
- **Frame Kernels (FKs)**:
  - mars_mola_dem_463m_v00.tf — *Frame kernel containing surface name to ID code mappings for the Mars 463M DEM USGS V2 Tiled DSK set.*

C.2. MEX_MetaKernel

This section lists the kernels loaded by the 'MEX_MetaKernel.tm' file.

- **Spacecraft Clock Kernels (SCLKs)**:
  - MEX_251124_STEP.tsc — *MEX spacecraft clock constants*
- **FKs**:

  - MEX_V16.tf *Frame kernel containing MEX specific frames.*
- **CKs**:
  - ATNM_SGS_P170331235152_01936.bc *Camera kernel containing MEX orientation/attitude data.*
- **SPKs**:
  - *MEX s/c ephemeris data (predicted and reconstructed):*
    - ORMF_T19_240614_320101_01863.BSP
    - ORMM_T19_250301000000_01903.BSP
    - ORMM_T19_250401000000_01907.BSP
    - ORMM_T19_250501000000_01912.BSP
    - ORMM_T19_250601000000_01916.BSP
    - ORMM_T19_250701000000_01920.BSP
    - ORMM_T19_250801000000_01924.BSP
    - ORMM_T19_250901000000_01930.BSP
    - ORMM_T19_250601000000_01916.BSP
    - ORMM_T19_251001000000_01934.BSP
    - ORMM_T19_251101000000_01936.BSP
    - ORMM_T19_251201000000_01936.BSP

C.3. TGO_MetaKernel

This section lists the kernels loaded by the 'TGO_MetaKernel.tm' file.

- **SCLKs**:
  - em16_tgo_fict_20180215.tsc *TGO spacecraft clock constants for a fictional clock*
  - em16_tgo_step_20251014.tsc *TGO spacecraft clock constants*
- **FKs**:
  - em16_tgo_v27.tf *Frame kernel containing TGO specific frames.*
- **CKs**:
  - em16_tgo_sc_fsp_418_01_20220101_20260110_s20251014_v01.bc *Camera kernel containing TGO orientation/attitude data.*
- **SPKs**:
  - *TGO s/c ephemeris data (predicted and reconstructed):*
    - em16_tgo_flp_011_01_20250203_20390104_v01.bsp
    - em16_tgo_fsp_394_01_20250310_20250823_v01.bsp
    - em16_tgo_fsp_401_01_20250428_20251011_v01.bsp
    - em16_tgo_fsp_418_01_20250811_20260221_v01.bsp

C.4. Tiled Mars MOLA DSK files

This section lists the kernels that make up the tiled Mars MOLA 128 pixel per degree digital shape model.

- **DSKs**:
  - mars_mola_dem_463m_xx_yy_v03.bds *where xx and yy range from 01 to 32 (so in total there are 1024 DSK files).*